Center for the Advancement of Natural Discoveries using Light Emission

Samvel Zakaryan

Electromagnetic waves in laminated structures and particle bunching

Thesis

to take a candidate degree in physical and mathematical sciences 01.04.20

“Charged Particle Beam Physics and Accelerator Technology”

Scientific supervisor:

Doctor of Physical and Mathematical Sciences

Mikayel I. Ivanyan

Yerevan 2017

Contents

Introduction ..... - 4 -

Chapter 1: Slow waves in laminated structures ..... - 10 -

1.1 Introduction ..... - 10 -

1.2 Slow waves in cylindrical structures ..... - 10 -

1.3 Attenuation parameter ..... - 13 -

1.4 Longitudinal impedance and radiation pattern ..... - 14 -

1.5 Slow waves in flat structures ..... - 16 -

1.6 Summary ..... - 24 -

Chapter 2: Accelerating structures with flat geometry ..... - 26 -

2.1 Introduction ..... - 26 -

2.2 Multilayer flat structure ..... - 27 -

2.3 Two-layer flat structure ..... - 35 -

2.4 Impedance of two-layer symmetrical flat structure ..... - 37 -

2.5 Approximate analytical representation of impedance ..... - 47 -

2.6 Summary ..... - 53 -

Chapter 3: Rectangular resonator with two-layer vertical walls ..... - 55 -

3.1 Introduction ..... - 55 -

3.2 IHLCC cavity with ideally conductive walls ..... - 56 -

3.3 Pure copper cavity. Measurements and interpretation ..... - 60 -

3.4 IHLCC cavity resonance frequency comparison with experimental results ..... - 62 -

3.5 Summary ..... - 67 -

Chapter 4: Electron bunch compression in single-mode structures ..... - 68 -

4.1 Introduction ..... - 68 -

4.2 Wakefields and Impedances ..... - 69 -

4.3 Ballistic bunching ..... - 71 -

4.4 Energy modulation, bunch compression and microbunching in cold neutral plasma ..... - 73 -

4.5 Energy modulation, bunch compression and microbunching in internally coated metallic tube ..... - 80 -

4.6 Summary ..... - 88 -

Summary ..... - 90 -

Acknowledgements ..... - 93 -

References ..... - 94 -

Introduction

The investigation of new accelerating structures and high frequency, high brightness coherent radiation sources is an important research area in modern accelerator physics [1-7]. High brightness and high intensity radiation in THz region opens new opportunities for researches in a wide range of areas [8-14]. European XFEL, SwissFEL accelerators are constructed to obtain this kind of radiation [15, 16]. To emit the THz radiation, one needs to generate ultrashort, intensive bunches [16-25]. When lengths of microbunches become smaller than the synchronous mode wavelength ($\sigma_z < \lambda$), a large number of electrons starts to radiate coherently and the intensity of the radiation field grows quadratically with the number of particles [26-28].

The direct generation of sub-ps bunches in RF guns is limited because of technical characteristics of photocathodes and lasers. Because of that reason, sub-ps bunches are usually formed by shortening the initial long bunches [29-31]. One of the main principles to obtain ultrashort bunches is to use SASE process [32, 33], which is widely used in modern accelerators (FELs) [15, 16]. Also it is possible to use additional external laser field to have a stronger microbunching [34-36]. The main principle of generating ultrashort bunches is to obtain energy modulation within the bunch and convert it into charge density modulation [22, 31, 37-39]. For the high energy bunches magnetic chicanes and for low energy ones velocity bunching is used to generate sub-ps bunches [40-45]. Energy modulation within the bunch can be obtained via bunch interaction with its own radiated wakefield or by the field emitted from bunches in front of it. For such a process disc loaded or dielectric loaded structures are widely used [46-51]. Both structure types are characterized by the high order modes, excited during the beam passage through them [51-62]. These high order modes play a parasitic role in particle acceleration processes.

Unlike disc and dielectric loaded structures, in the single mode structures like plasma and circular waveguide with two-layer metallic walls (ICMT – internally coated metallic tube) there are no parasitic high order modes [63-67]. In the dissertation the microbunching processes are studied in single mode structure.

It is theoretically shown that ICMT has a single slowly propagating high frequency mode [66]. In case of structure appropriate geometry, a charged particle moving along the structure axis radiates in the terahertz frequency region. While the theoretical study of ICMT shows that for certain conditions it is a single-mode structure, the experiment on it is related to some technical difficulties. To serve as a high frequency single-mode structure, ICMT requires high accuracy, μm – sub-μm low conductivity internal coating, and an inner diameter in the order of several mm [66], which is technically a complex problem. Because of these problems, it is preferable to do an experiment on a structure which is similar to ICMT and is more simple in mechanical means. As such a multilayer flat metallic structure is considered. For appropriate parameters these two structures are similar, and it is expected that two-layer flat structure should be single-mode, high frequency too.

The thesis consists of introduction, four chapters, summary and bibliography. In introduction a short review on the actuality of problems and the main results of the thesis are given.

The **first** chapter of the dissertation is devoted to the study of slow waves in laminated structures. The study of high frequency accelerating structures is an important issue for the development of future compact accelerator concepts [68-70]. The laminated structures are widely used in advanced accelerators to meet the technical specifications like high vacuum performance, cure of static charge, reduction of the impedance, etc. [53]. The electrodynamic properties of two-layer structures, based on field matching technique, have been studied in Refs. [71–74]. For the internally coated metallic tube (ICMT), with coating thickness smaller than the skin depth, the longitudinal impedance has a narrow band resonance at high frequency [74], which is conditioned by the synchronous TM_{01} fundamental mode [75]. In the first chapter, the peculiarities of high frequency TM_{01} mode, slowly propagating in ICMT structure, is analyzed both numerically and analytically. The TM modes dispersion curves and the TM_{01} mode attenuation constant are given. Dispersion relations of flat two-layer structure are investigated. The longitudinal impedance and the radiation patterns for large aperture ICMT structures are discussed.

The main results of the first chapter are

- The single slow propagating mode properties in laminated structures are studied. It is shown that two-layer cylindrical structure has single slowly traveling mode (TM_{01}) in THz frequency range.
- Explicit expression for attenuation constant of two-layer structure's TM_{01} mode is obtained.
- Dispersion relations of flat two-layer structure are derived.

The **second** chapter of the thesis is devoted to study of electrodynamic properties of multilayer two infinite metallic parallel plates. A bunch traveling through the structure excites wakefields [52-54, 76-79]. The longitudinal component of the wakefield produces extra voltage for the trailing particles in the bunch [80-83]. The Fourier transformation of wake potential for a point driving charge is the impedance of the structure, which presents the excited electromagnetic field in frequency domain [52, 53]. For ultrarelativistic particles, the impedance is independent of the beam parameters and can describe a structure in frequency domain.

The field matching technique, based on matching the tangential components of the electromagnetic fields at the borders of layers, is used to calculate electromagnetic fields. Matrix formalism is developed to couple electromagnetic field tangential components in two borders of layers. Fourier transformed electromagnetic fields, excited by a relativistic point charge, are obtained analytically for two-layer unbounded two parallel infinite plates. As a special case, electromagnetic fields of single-layer unbounded and two-layer structures with perfectly conducting outer layers are obtained. The longitudinal impedance of two-layer structure with outer perfectly conducting layer, excited by an ultrarelativistic particle, is calculated numerically. It is shown that for low conductivity inner layer the driving particle radiation has a narrow-band resonance. The resonance frequency is well described by the formula $f_{res} = \frac{c}{2\pi}\sqrt{\frac{1}{a\,d}}$, where a is the half-height of the structure, d is the layer thickness and c is the velocity of light in vacuum. The longitudinal wake potential is calculated, and it is shown that it is a quasi-periodic function with the period Δs given by the resonant frequency $\Delta s = \frac{c}{f_{res}}$.

The main results of the second chapter are:

- A method of calculating point charge excited electromagnetic fields in multilayer infinite parallel plates is developed.
- Expressions of radiation fields in two-layer parallel plates are analytically derived.
- Longitudinal impedance and dispersion relations of symmetrical two-layer parallel plates with perfectly conducting outer layer are derived.
- A comparison of the electro-dynamic properties of two-layer parallel plates and of ICMT is performed.
- Conditions in which the point charge radiation in two-layer parallel plates has a narrow-band resonance are obtained.
- Wakefields generated by a point charge traveling through the center of the two-layer parallel plates, with outer perfectly conducting material, are calculated.

In the **third** chapter a theoretical study of rectangular cavity with laminated walls and comparison with the experimental results are presented. In the second chapter it is shown that for appropriate parameters two-layer parallel infinite plates have a distinct, narrow band resonance. In this chapter, a real, limited structure, which is similar to the parallel plates, is studied. As such a structure, a rectangular cavity with laminated horizontal walls is considered. For the cavity, with vertical dimensions much bigger than horizontals ones, the electrodynamic characteristics are expected to be similar to the ones for parallel plates. In the case of a resonator, unlike the parallel plates, one has a discrete set of eigenfrequencies in all three degrees of freedom. To be able to distinguish the main resonance from the secondary ones, a finite wall resonator model (perfectly conducting rectangular cavity with inner low conductivity layers at the top and bottom walls) is developed and resonances of the model are studied.

A comparison of resonant frequencies of a resonator model with resonances of the test copper cavity, with inner germanium layers and parallel two-layer plates, is done. A good agreement between these results is obtained ($\Delta f / f_{rez} < 0.03$). The experimental results show the presence of fundamental resonance which is caused by the two-layer horizontal cavity walls. The measured fundamental frequencies are close to those

calculated for the two-layer parallel plates, their values are subjected to the laws specific to this kind of structures: they are decreasing with cavity height increase.

The main results of the third chapter are:

- The resonance properties of a copper rectangular resonator and a copper resonator with an internal germanium coating are experimentally investigated and theoretically substantiated.
- A theoretical model of a rectangular cavity with horizontal laminated walls is created and electro-dynamical properties of it are studied.
- A good correlation between resonance frequencies of the model and test facility is fixed: all resonances of the test structure correspond to the modes of the model.
- It is shown that for a resonator, with vertical dimensions much bigger than horizontal ones, the resonance frequencies are in a good agreement with resonances of two-layer infinite parallel plates.

The **forth** chapter of the dissertation is devoted to the generation of sub-ps bunches via bunch compression and microbunching processes in single-mode structures. Wakefields, generated by an electron bunch propagating through a structure, act back on the bunch particles or on the ones traveling behind it, producing energy modulation or transverse kick [52-54, 84-86]. In case of appropriate parameters, this process can lead to energy modulation within the bunch, which then can be transformed into a charge density modulation. For non-ultrarelativistic ($10\ MeV$) electron bunches, the energy modulation causes velocity modulation, which leads to bunch compression or microbunching at proper ballistic distances.

Single-mode structures, due to the absence of high order parasitic modes, are ideal candidates for this process. The plasma channel and internally coated metallic tube are observed as an example of single-mode structures. The method of ballistic bunching is used: the bunch is considered rigid in a structure and only energy modulations occur, then in the drift space the energy modulation leads to charge redistribution.

The main results of the forth chapter are:

- It is shown that the Gaussian distributed bunch interaction with a single-mode structure leads to its compression. For appropriate bunch and structure parameters a bunch compression for 8 and 12 times for plasma and ICMT is reached, respectively.
- It is shown that the microbunching of non-Gaussian bunches is possible in single-mode structures. For parabolic distributed bunches $20\,\mu m$ and $3\,\mu m$ microbunches and for rectangular distributed bunches $40\,\mu m$ and $8\,\mu m$ microbunches can be formed for plasma and ICMT, respectively.
- The relations among the bunch length, structure parameters and microbunch formation distance are analyzed for various bunch shapes. The optimal parameters for structures and drift space distances are obtained.

The main results of the dissertation are the following:

- The single slowly propagating mode properties in laminated structures are studied.
- The electromagnetic fields of multilayer parallel plates are analytically derived.
- Dispersion relations of two-layer parallel plates are derived and single resonance frequency is obtained.
- The narrow-band high frequency longitudinal impedance and longitudinal wake function of two-layer parallel plates are calculated.
- Resonance frequencies of rectangular cavity with horizontal double-layer metallic walls are derived.
- A good agreement between the theoretical results and experiment is fixed.
- It is shown that the generation of ultrashort bunches ($\sim 10\,\mu m$) in single-mode structures is possible via ballistic bunching.

The study results have been reported at international conferences, during the seminars at CANDLE Synchrotron Research Institute, Yerevan State University, DESY, Paul Scherrer Institute and are published in scientific journals [75, 87-90].

Chapter 1: Slow waves in laminated structures

1.1 Introduction

In this chapter the conditions in which slowly propagating free oscillations are formed in cylindrical and flat two-layer metallic structures are studied. The importance of establishing the presence of such oscillations is due to the fact that the radiation of a moving particle in accelerating structures is synchronous (or is synphase) with its motion. In particular, for an ultrarelativistic particle moving at the speed of light, the phase velocity of the emitted wave is the same too.

As is known, an arbitrary field, generated or propagating in a closed structure, can be expressed with the help of a superposition of the eigenoscillations of a given structure. The field generated by a particle must only contain synchronous components of its own oscillations.

In this chapter, we consider mechanisms of the formation of a synchronous mode in two-layer cylindrical and planar structures and demonstrate their connection with longitudinal impedances. In particular, for a flat structure, a relationship between the eigenvalues of the synchronous mode and the poles of the impedance integral is established.

1.2 Slow waves in cylindrical structures

In this chapter a round metallic two-layer hollow pipe of inner radius a with a perfectly conducting outer layer and an inner metallic layer of conductivity σ and thickness $d = b - a$ (Figure 1.1) is considered.

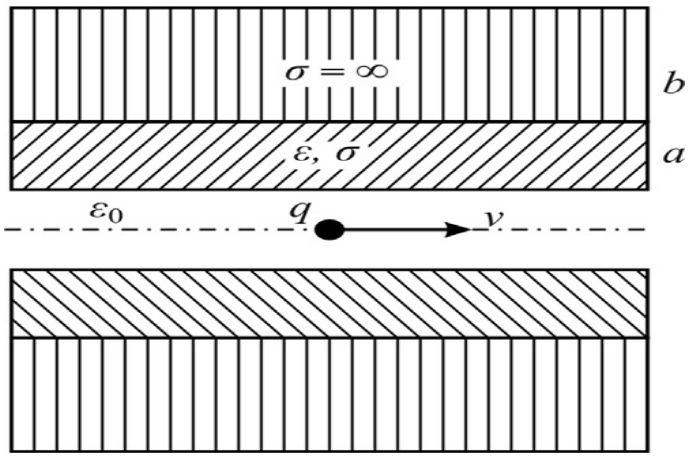

Figure 1.1: The geometry of the internally coated metallic tube.

In axially symmetric geometry, the non-zero electromagnetic field components (E_z, E_r, H_θ) of the axially symmetric monopole TM modes are proportional to $exp\left(j\beta_{0_n}z - j\omega t\right)$, where $\beta_{0_n} = \sqrt{k^2 - \nu_{0_n}^2}$ and ν_n are the longitudinal and radial propagation constants, respectively, $k = {\omega}/{c}$ is the wave number, ω is the frequency and c is the velocity of light. The dispersion relation for the modes is derived by the matching of electromagnetic field tangential components (E_z, H_θ) at the boundaries of layers. Omitting the factor $exp\left(j\beta_{0_n}z - j\omega t\right)$, the tangential components of electromagnetic fields in vacuum ($r < a$) and metallic wall ($a \le r \le b$) regions are given as:

$$\begin{aligned} E_z(r,z) &= AJ_0\left(\nu_{0_n}r\right) \\ H_\theta(r,z) &= A\frac{j\omega\varepsilon_0}{\nu_{0_n}}J_1\left(\nu_{0_n}r\right) \end{aligned} \qquad r < a$$

$$\text{for} \qquad (1.1)$$

$$\begin{aligned} E_z(r,z) &= BJ_0\left(\lambda_{0_n}r\right) + CH_0^{(1)}\left(\lambda_{0_n}r\right) \\ H_\theta(r,z) &= \frac{j\omega\varepsilon_1}{\lambda_{0_n}}\left[BJ_1\left(\lambda_{0_n}r\right) + CH_1^{(1)}\left(\lambda_{0_n}r\right)\right] \end{aligned} \qquad a \le r \le b$$

where $\lambda_{0_n} = \sqrt{\nu_{0_n}^2 - \chi^2}$, $\chi = j\,{\sqrt{2}}/{\delta}$ is the radial propagation constant in internal metallic layer, $\delta = c\left({2\varepsilon_0}/{\sigma\omega}\right)$ is the skin depth, ε_0 and $\varepsilon_1 = \varepsilon_0 + {j\sigma}/{\omega}$ are the vacuum and metal dielectric constants, respectively, $J_{0,1}(x)$, $H_{0,1}^{(1)}(x)$ are the zero and first order Bessel and Hankel functions, respectively.

The unknown coefficients A, B, C are defined by the matching of tangential components (E_z, H_θ) at ($r = a$) and the vanishing of the electric field E_z at the perfect conducting outer wall ($r = b$). The non-zero solution is provided by zero determinant of a system of three linear algebraic equations. This defines the eigenvalue equation:

$$\frac{\varepsilon_0 J_1(\nu_{0_n} a)}{\varepsilon_1 J_0(\nu_{0_n} a)} = \frac{\nu_{0_n} J_1(\lambda_{0_n} a) H_0^{(1)}(\lambda_{0_n} b) - J_0(\lambda_{0_n} b) H_1^{(1)}(\lambda_{0_n} a)}{\lambda_{0_n} J_0(\lambda_{0_n} a) H_0^{(1)}(\lambda_{0_n} b) - J_0(\lambda_{0_n} b) H_0^{(1)}(\lambda_{0_n} a)} \tag{1.2}$$

In a high frequency range, where the inequalities $|\chi| \gg |\nu_{0_n}|$ ($|\lambda_{0_n}| \approx {\sqrt{2}}/{\delta}$), $|\lambda_{0_n}| a \gg 1$ and $\delta \ll a$ are hold, Eq. 1.2 is modified to

$$\frac{\varepsilon_0 J_1(\nu_{0_n} a)}{\nu_{0_n} J_0(\nu_{0_n} a)} = \frac{\varepsilon_1}{\lambda_{0_n}} \cot(\lambda_{0_n} d) \tag{1.3}$$

For the inner metallic layer thickness d, less than the skin depth δ ($d \ll \delta$), and for not very high frequencies $\omega \ll {\sigma}/{\varepsilon_0}$ ($\varepsilon_1 \approx {j\sigma}/{\omega}$), the Eq. 1.3 is expressed as

$$\frac{1}{\nu_{0_n} a} \frac{J_1(\nu_{0_n} a)}{J_0(\nu_{0_n} a)} = \frac{1}{k^2 a d} \tag{1.4}$$

In the frequency range of interest (THz), the inequality $\omega \ll {\sigma}/{\varepsilon_0}$ holds well for practically all metals (for copper, ${\sigma}/{\varepsilon_0} \approx 10^5\, TH$). The frequency range of applicability for expression (1.4) is given as $d \ll \delta \ll a$.

The analysis of Eq. 1.4 shows that the radial propagation constants ν_{0_n} of high TM_{0n} ($n > 1$) modes are purely real and non-zero. Therefore, the phase velocity for high order modes $\nu_{ph} = {ck}/{\beta_{0n}}$ is higher than the velocity of light. For fundamental TM_{01} mode, the parameter ν_{01} vanishes ($\nu_{01} = 0$) at $k_0 = \sqrt{2/ad}$ ($\nu_{ph} = c$) frequency, ν_{01} is purely real for $k < k_0$ ($\nu_{ph} > c$) and ν_{01} is purely imaginary for $k > k_0$ ($\nu_{ph} < c$). Thus, the structure under consideration is characterized by a single slowly propagating TM_{01}mode at high frequency. Figure 1.2 shows the dispersion curves for the fundamental TM_{01} and high

order TM_{0n} ($n > 1$) modes. As is seen, only the fundamental mode crosses the synchronous line $\beta = k$ ($v_{ph} = c$) at a resonant frequency of $k = k_0 = \sqrt{2/ad}$.

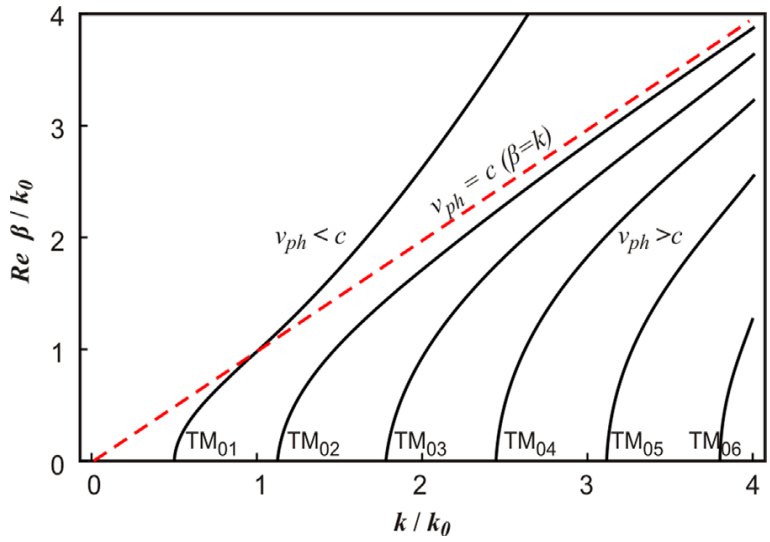

Figure 1.2: Dispersion curves for fundamental TM_{01} and high order TM_{0n} ($n > 1$) modes.

1.3 Attenuation parameter

To evaluate the TM_{01} mode attenuation constant $\alpha_{01} = Im(\beta_{01})$ for thin inner layer ($d \ll \delta$), the second term in expansion of formula 1.3 should be taken into account, i.e. $\cot(\chi) \approx {}^{1}/_{\chi} - {}^{\chi}/_{3}$,

$$\frac{J_1(\nu_{01}a)}{\nu_{01}aJ_0(\nu_{01}a)} = \frac{k_0^2}{2k^2} - j\frac{\eta}{ka} \tag{1.5}$$

where $\eta = (\varsigma + \varsigma^{-1})/\sqrt{3}$, $\varsigma = Z_0 d\sigma/\sqrt{3}$. The numerical solutions for real and imaginary parts of TM_{01} mode transverse propagation constant are presented in Figure 1.3 ($^{d}/_{a} = 10^{-3}$, $\varsigma = 1$). For small arguments of Bessel functions $|\nu_{01}|a \ll 1$ one can obtain the following approximate expression:

$$\nu_{01}{}^2 \approx \frac{16}{a^2}\left(-\frac{1}{2} + \frac{k_0^2}{2k^2} - j\frac{\eta}{ka}\right) \tag{1.6}$$

Note, that the real and imaginary parts of transverse propagation constant ν_{01} at the resonance frequency $k = k_0 = \sqrt{2/ad}$ are given as:

$$Re(\nu_{01}) = -Im(\nu_{01}) = \frac{1}{a}\sqrt{\frac{8\eta}{k_0 a}} \tag{1.7}$$

and the relation $|\nu_{01}|a \ll 1$ holds well around the resonance frequency. For high frequency $k \gg |\nu_{01}|$, the longitudinal propagation constant $\beta_{01} = \sqrt{k^2 - {\nu_{01}}^2}$ is given as:

$$\beta \approx k + \frac{4}{k^3 a^2}\left(k^2 - {k_0}^2\right) + j\frac{8\eta}{a(ka)^2} \tag{1.8}$$

The attenuation constant at resonance frequency ($k = k_0$) is then given as $\alpha_{01} = 4d\eta/a^2$.

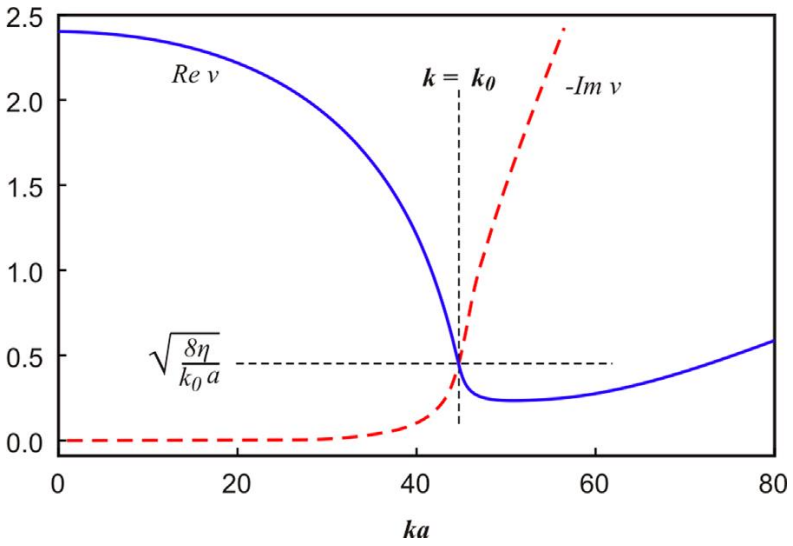

Figure 1.3: Real (solid) and imaginary (dashed) parts of TM_{01} mode transverse eigenvalue $\nu = \nu_{01}a$.

1.4 Longitudinal impedance and radiation pattern

A relativistic charge traveling along the axis of a round metallic two-layer hollow pipe (Fig. 1.1) is considered. The excited non-zero electromagnetic field components (E_z, E_r, H_θ) of the axially symmetric monopole mode in the vacuum region can be derived based on the field matching technique [72]. A good analytical approximation for metallic type two-layer tube longitudinal impedance can be obtained in high frequency range, when the skin depths δ are much smaller than the tube radius a, i.e. $\delta \ll a$ [74].

$$Z_{\parallel}^{0} = j\frac{Z_0}{\pi k a^2}\left(1 + \frac{2}{a}\frac{\varepsilon}{\varepsilon_0 \chi} cth(\chi d)\right)^{-1} \tag{1.9}$$

where $Z_0 = 120\pi\ \Omega$ is the impedance of free space. For the layer thickness d smaller with respect to the skin depth δ ($d \ll \delta$) and for not very high frequencies ($\omega \ll \sigma/\varepsilon_0$), the impedance can be presented in a form of parallel resonance circuit impedance:

$$Z_{\parallel}^{0} = R\left[1 + jQ\left(\frac{\omega_0}{\omega} - \frac{\omega}{\omega_0}\right)\right]^{-1} \tag{1.10}$$

where $\omega_0 = c\sqrt{2/ad}$ is the resonant frequency, $R = Z_0(2\pi a\eta)^{-1}$ is the shunt impedance, $Q = \omega_0 a(2c\eta)^{-1}$ is the quality factor.

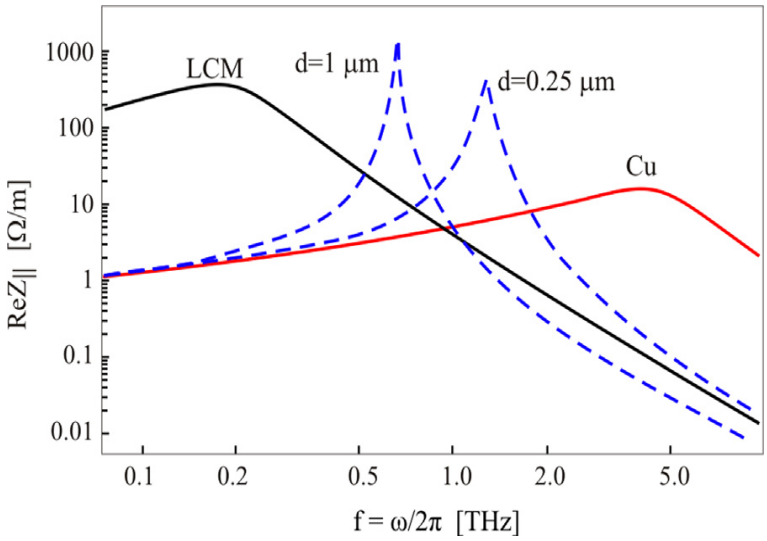

Figure 1.4: Longitudinal impedance for Cu, LCM (solid) and Cu-LCM (dashed) tubes.

Figure 1.4 presents the field matching based exact numerical simulations of longitudinal impedance for copper (Cu, $\sigma_1 = 5.8 \times 10^7\ \Omega^{-1}m^{-1}$) tube, internally coated by the low conductivity metal (LCM, $\sigma_1 = 5 \times 10^3\ \Omega^{-1}m^{-1}$) of $d = 1\,\mu m$ and $d = 0.25\,\mu m$ thickness. The tube radius is $a = 1\,cm$. As is seen, in the transition region for thin LCM layer the impedance is modified to narrow band resonance at the frequency $f_0 = \omega_0/2\pi$, corresponding to $f_0 = 0.675\,THz$ for $d = 1\,\mu m$ and $f_0 = 1.35\,THz$ for $d = 0.25\,\mu m$. The impedance has a different nature for single and two-layer tubes. It has a broadband maximum for the single layer tube and narrow band resonance at high frequency ω for two-layer tube. An important feature is that the resonance is observed when the inner layer thickness is less than the layer skin depth. Thus, the resonance is conditioned by the interference of scattered electromagnetic fields from the inner and outer layers.

The radiation pattern at the open end of the waveguide can be evaluated by using the “from near to far fields” transformation technique.

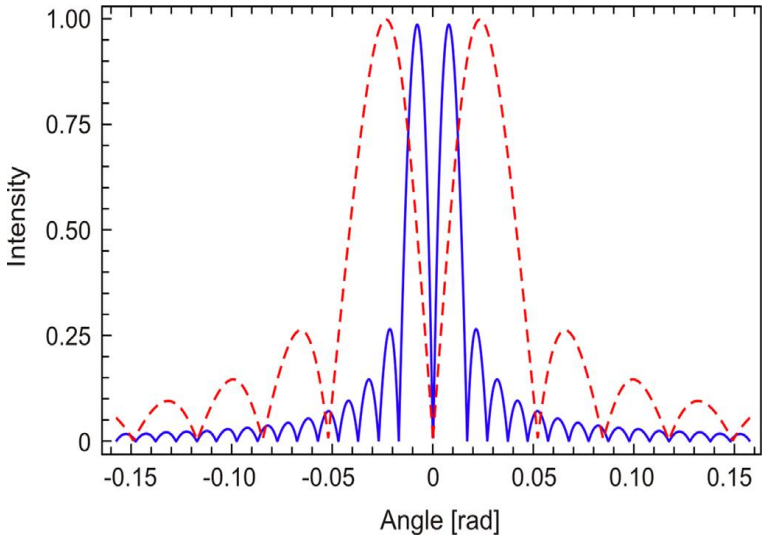

Figure 1.5: Radiation pattern for frequencies $f = 1.35\,THz$ (solid) and $f = 4.7\,THz$ (dashed).

Fig. 1.5 presents the angular distribution of the normalized radiation intensity with respect to waveguide axis $\theta = 0$ for the internal layer thickness of $d = 0.25\,\mu m$ and resonant frequencies $f = 4.7\,THz$ $(a = 1\,mm)$ and $f = 1.35\,THz$ $(a = 1\,cm)$. The radiation pattern is zero at $\theta = 0$ and reaches its maximum value at $\theta = arcsin\left(2.3\sqrt{d/2a}\right)$.

1.5 Slow waves in flat structures

In this section, we derive the dispersion relations that determine the eigenfrequencies of electromagnetic oscillations of two infinite parallel planes, the latter being covered by a thin conducting layer from inside. The metal layers are identical: with a thickness d and a conductivity σ. The permittivity of the layers is characterized by the expression $\varepsilon = \varepsilon' + j\,\sigma/\omega$, where ε' is the static permittivity of the metal (for most metals $\varepsilon' = \varepsilon_0$, where ε_0 is the permittivity of vacuum, for germanium $\varepsilon' = 16\varepsilon_0$) and ω is the frequency. The distance between the inner surfaces of the plates is $2a$.

The solution for the natural electromagnetic oscillations (eigenoscillations) of the structure is sought by the method of partial regions. In the case under consideration, we can distinguish three regions: the regions of the upper $(a \le y \le a + d,\ i = 1)$ and lower $(-a - d \le y \le a, i = -1)$ metal layers and the vacuum region between the plates $(-a \le$

$y \le a, i = 0)$. In the outer ideally conducting layers, the fields and currents are absent. Since all three regions have finite dimensions along the transverse direction, in each of them quasi-plane waves with both damped and increasing amplitudes can propagate. Thus, in each of the three regions, the fields can be written in an identical form. In particular, electrical components in each of the three regions $(i = 0, \pm 1)$ are written as:

$$E^{(i)}_{x,y,z} = E^{(i)}_{1,x,y,z} + E^{(i)}_{2,x,y,z} \tag{1.11}$$

with

$$E^{(i)}_{1,2,x,y,z}(\vec{r}) = \int_{-\infty}^{\infty}\int_{-\infty}^{\infty} \tilde{E}^{(i)}_{1,2,x,y,z} dk_x dk_z dk \tag{1.12}$$

where

$$\begin{aligned}
\tilde{E}^{(i)}_{1,2,x} &= A_{1,2,x} \begin{Bmatrix} Sh\left(k_y^{(i)} y\right) \\ Ch\left(k_y^{(i)} y\right) \end{Bmatrix} e^{j(k_x x + k_z z - \omega t)} \\
\tilde{E}^{(i)}_{1,2,y} &= A_{1,2,y} \begin{Bmatrix} Ch\left(k_y^{(i)} y\right) \\ Sh\left(k_y^{(i)} y\right) \end{Bmatrix} e^{j(k_x x + k_z z - \omega t)} \\
\tilde{E}^{(i)}_{1,2,z} &= A_{1,2,z} \begin{Bmatrix} Sh\left(k_y^{(i)} y\right) \\ Ch\left(k_y^{(i)} y\right) \end{Bmatrix} e^{j(k_x x + k_z z - \omega t)}
\end{aligned} \tag{1.13}$$

Here $A_{1,2,x,y,z}$ are arbitrary weight coefficients (amplitudes) and $\omega = kc$. The magnetic field components are determined from electrical field components with the help of Maxwell equations:

$$\vec{B}^{(i)}_{1,2}(\vec{r}) = \frac{1}{j\omega} rot\, \vec{E}^{(i)}_{\pm}(\vec{r}) \tag{1.14}$$

whence

$$\tilde{B}_{1,2,x}^{(i)} = \frac{1}{j\omega}\left(k_y^{(i)} A_{1,2,z}^{(i)} - jk_z A_{1,2,y}^{(i)}\right)\begin{Bmatrix} Ch\left(k_y^{(i)} y\right) \\ Sh\left(k_y^{(i)} y\right) \end{Bmatrix} e^{j(k_x x + k_z z - \omega t)}$$

$$\tilde{B}_{1,2,y}^{(i)} = -\frac{1}{\omega}\left(k_x A_{1,2,z}^{(i)} - k_z A_{1,2,x}^{(i)}\right)\begin{Bmatrix} Sh\left(k_y^{(i)} y\right) \\ Ch\left(k_y^{(i)} y\right) \end{Bmatrix} e^{j(k_x x + k_z z - \omega t)} \qquad (1.15)$$

$$\tilde{B}_{1,2,x}^{(i)} = -\frac{1}{j\omega}\left(k_y^{(i)} A_{1,2,x}^{(i)} - jk_z A_{1,2,y}^{(i)}\right)\begin{Bmatrix} Ch\left(k_y^{(i)} y\right) \\ Sh\left(k_y^{(i)} y\right) \end{Bmatrix} e^{j(k_x x + k_z z - \omega t)}$$

The relationship between the amplitudes $A_{1,2,z}^{(i)}$ and $A_{1,2,x}^{(i)}, A_{1,2,y}^{(i)}$ is determined from the Maxwell equation:

$$div\vec{E}_{1,2}^{(i)} = 0 \qquad (1.16)$$

whence

$$A_{1,2,z}^{(i)} = \frac{1}{k_z}\left(jk_y^{(i)} A_{1,2,x}^{(i)} - k_x A_{1,2,x}^{(i)}\right) \qquad (1.17)$$

To determine the relationship between wave numbers and frequency we use the identity, which follows from Eq. 1.13:

$$rot\ rot\vec{E}_{1,2}^{(i)} = \left(k_x^2 - \left(k_y^{(i)}\right)^2 + k_z^2\right)\vec{E}_{1,2}^{(i)}(k_x, k_z, k, \vec{r}) \qquad (1.18)$$

and the equation, which is a consequence of Maxwell's equations:

$$rot\ rot\vec{E}_{\pm}^{(i)} = k^2 \varepsilon_i' \mu_i' \vec{E}_{\pm}^{(i)} \qquad (1.19)$$

with ε_i', μ_i' relative electric and magnetic permeability in the respective regions ($\varepsilon_{\pm 1}' = 1 + j\,\sigma/\varepsilon_0\omega$, $\mu_{\pm 1}' = 1$; $\varepsilon_0' = \mu_0' = 1$), and $k = \omega/c$.

Comparing Eq. 1.18 and Eq. 1.19, we obtain

$$k_y^{(i)} = \sqrt{-k^2 \varepsilon_i' \mu_i' + k_x^2 + k_z^2} \qquad (1.20)$$

For inner (vacuum) part of structure

$$k_y^{(0)} = \sqrt{-k^2 + k_x^2 + k_z^2} \qquad (1.21)$$

To construct the dispersion relations (relationship between k_x and k) one should set up a system of linear equations based on field matching at the boundaries of the structure areas:

$$\begin{aligned}
&1. \quad E_x^{(1)} = 0, \quad E_z^{(1)} = 0 && \text{at } y = a + d \\
&2. \quad E_x^{(1)} = E_x^{(0)},\ E_z^{(1)} = E_z^{(0)};\quad B_x^{(1)} = B_x^{(0)}, B_z^{(1)} = B_z^{(0)} && \text{at } y = a \\
&3. \quad E_x^{(-1)} = E_x^{(0)}, E_z^{(-1)} = E_z^{(0)};\ B_x^{(-1)} = B_x^{(0)}, B_z^{(-1)} = B_z^{(0)} && \text{at } y = -a \\
&4. \quad E_x^{(-1)} = 0, \quad E_z^{(-1)} = 0 && \text{at } y = -a - d
\end{aligned} \tag{1.22}$$

As a result, a system of 12 equations containing 12 unknown amplitudes is obtained. Dispersion relations are determined by the determinant of this system being equal to zero. These relations take a form consisting of a product of four factors:

$$D = \prod_{i=1}^{4} T_i = 0 \tag{1.23}$$

where

$$\begin{aligned}
T_1 &= k_y^{(1)} Ch\left(dk_y^{(1)}\right) Sh\left(ak_y^{(0)}\right) + k_y^{(0)} Sh\left(dk_y^{(1)}\right) Ch\left(ak_y^{(0)}\right) \\
T_2 &= k_y^{(1)} Ch\left(dk_y^{(1)}\right) Ch\left(ak_y^{(0)}\right) + k_y^{(0)} Sh\left(dk_y^{(1)}\right) Sh\left(ak_y^{(0)}\right) \\
T_3 &= k_y^{(0)} \left(k_y^{(1)^2} - k_x^2 - k_z^2\right) Ch\left(dk_y^{(1)}\right) Sh\left(ak_y^{(0)}\right) + k_y^{(1)} \left(k_y^{(0)^2} - k_x^2 - k_z^2\right) Sh\left(dk_y^{(1)}\right) Ch\left(ak_y^{(0)}\right) \\
T_4 &= k_y^{(0)} \left(k_y^{(1)^2} - k_x^2 - k_z^2\right) Ch\left(dk_y^{(1)}\right) Ch\left(ak_y^{(0)}\right) + k_y^{(1)} \left(k_y^{(0)^2} - k_x^2 - k_z^2\right) Sh\left(dk_y^{(1)}\right) Sh\left(ak_y^{(0)}\right)
\end{aligned} \tag{1.24}$$

Taking into account $k_y^{(i)} = \sqrt{-k^2 \varepsilon_i' \mu_i' + k_x^2 + k_z^2}$ from Eq. 1.18, instead of T_3 and T_4 , we can write

$$\begin{aligned}
T_3 &= -k_y^{(0)} k^2 \varepsilon_i' \mu_i' Ch\left(dk_y^{(1)}\right) Sh\left(ak_y^{(0)}\right) - k_y^{(1)} k^2 Sh\left(dk_y^{(1)}\right) Ch\left(ak_y^{(0)}\right) \\
T_4 &= -k_y^{(0)} k^2 \varepsilon_i' \mu_i' Ch\left(dk_y^{(1)}\right) Ch\left(ak_y^{(0)}\right) - k_y^{(1)} k^2 Sh\left(dk_y^{(1)}\right) Sh\left(ak_y^{(0)}\right)
\end{aligned} \tag{1.25}$$

An independent system of natural oscillations of the structure is determined by the factors $(T_i = 0,\ i - 1,2,3,4)$ being equal to zero.

The radiation generated by a particle is synchronous with its motion. The spectral components of its radiation field have a phase velocity equal to the speed of light $v_{ph} = \omega/k = c$. In this case, the direction particle motion (direction along the z axis) is

distinguished. In the case of natural electromagnetic oscillations, determined in the absence of a particle or some other source of radiation, the directions along both horizontal axes $\vec{x}$ and $\vec{z}$ are equivalent. This fact manifests itself in a symmetrical dependence of the frequency $k = \omega/c$ on the wave numbers k_x and k_z (1.21):

$$k = \sqrt{k_x^2 + k_z^2 - {k_y^{(0)}}^2} \tag{1.26}$$

The phase velocity of eigenfunctions of the structure has the following form:

$$v_{ph} = \omega/k_z = \frac{k}{k_z}c = \frac{\sqrt{k_x^2+k_z^2-{k_y^{(0)}}^2}}{k_z}c \tag{1.27}$$

As can be seen from Eq. 1.27, the phase velocity of the natural oscillations is equal to the velocity of the particle (the speed of light in a vacuum) under condition $k = k_z$. The amplitudes $A_{1,2,x,y,z}$ are then written in a form containing the Dirac delta function: $A_{1,2,x,y,z} = \tilde{A}_{1,2,x,y,z}\delta(k - k_z)$. Taking into account $= k_z$, the vertical wave numbers $k_y^{(i)}$ will take the form $k_y^{(i)} = \sqrt{k^2(1 - \varepsilon_i'\mu_i') + k_x^2 + k_z^2}$ for $i = \pm 1$ (in layers) and $k_y^{(0)} = k_x$ at $i = 0$ (in the inner vacuum region).

Thus, for synchronous eigenmodes, generated by a particle, instead of (1.24, 1.25), one can write (by replacing $k_y^{(0)}$ with k_x):

$$\begin{aligned}
T_1 &= k_y^{(1)} Ch\left(dk_y^{(1)}\right) Sh(ak_x) + k_x Sh\left(dk_y^{(1)}\right) Ch(ak_x) \\
T_2 &= k_y^{(1)} Ch\left(dk_y^{(1)}\right) Ch(ak_x) + k_x Sh\left(dk_y^{(1)}\right) Sh(ak_x) \\
T_3 &= -k_x k^2 \varepsilon_i'\mu_i' Ch\left(dk_y^{(1)}\right) Sh(ak_x) - k_y^{(1)} k^2 Sh\left(dk_y^{(1)}\right) Ch(ak_x) \\
T_4 &= -k_x k^2 \varepsilon_i'\mu_i' Ch\left(dk_y^{(1)}\right) Ch(ak_x) - k_y^{(1)} k^2 Sh\left(dk_y^{(1)}\right) Sh(ak_x)
\end{aligned} \tag{1.28}$$

Let us compare the obtained expressions 1.28 with the denominators of the impedance (Eq. 2.45) obtained in chapter 2 writing them in a form convenient for comparison:

$$\begin{matrix} R_1^C \\ R_2^C \end{matrix}\Big\} = \pm \begin{Bmatrix} k_y^{(1)} \\ k_x k^2 \varepsilon_i' \mu_i' \end{Bmatrix} Ch\left(k_y^{(1)} d\right) Ch(k_x a_1) \pm \begin{Bmatrix} k_x \\ k_y^{(1)} k^2 \end{Bmatrix} Sh\left(k_y^{(1)} d\right) Sh(k_x a_1)$$
$$\begin{matrix} R_1^S \\ R_2^S \end{matrix}\Big\} = \pm \begin{Bmatrix} k_y^{(1)} \\ k_x k^2 \varepsilon_i' \mu_i' \end{Bmatrix} Ch\left(k_y^{(1)} d\right) Sh(k_x a_1) \pm \begin{Bmatrix} k_x \\ k_y^{(1)} k^2 \end{Bmatrix} Sh\left(k_y^{(1)} d\right) Ch(k_x a_1) \quad (1.29)$$

The comparison gives a complete coincidence of the expressions 1.28 and 1.29

$$T_1 = R_1^S, T_2 = R_1^C, T_3 = R_2^S, T_4 = R_2^C \quad (1.30)$$

Thus, the complex roots of the dispersion equations ($T_i = 0,\ i = 1,2,3,4$) are the poles of impedance function on the complex plane k_x. When the particle moves along the symmetry plane of the structure ($\Delta y = 0$) only two dispersion equations are realized: $T_2 = 0$ and $T_4 = 0$. With a parallel offset of the particle from the horizontal plane of symmetry ($\Delta y \neq 0$), all four dispersion equations are realized: $T_i = 0,\ i = 1,2,3,4$.

In the approximation $k_x^2 \ll Z_0 \sigma k_z$ or $k_y^{(1)} \approx \sqrt{-jZ_0 \sigma k_z}$, (in the cylindrical case this approximation is equivalent to the one for the permittivity of the metal $\varepsilon \approx j\,\sigma/\omega$, which is valid for not very large frequencies), the expressions (1.28) or (1.29) become analytic on the complex plane k_x, which allows us to directly calculate the integral functions through which the impedance is expressed using the residue theorem [91].

The final form of the second and fourth equations (1.28) is:

$$\begin{gathered} k_x Th(ak_x) = -\sqrt{-jZ_0 \sigma k}\, Cth\left(d\sqrt{-jZ_0 \sigma k}\right) \\ \frac{Th(ak_x)}{k_x} = \frac{\sqrt{-j\sigma Z_0 k}}{k^2} Cth\left(d\sqrt{-j\sigma Z_0 k}\right) \end{gathered} \quad (1.31)$$

At a fixed frequency, the right-hand sides of Eq. 1.31 are constant (independent of the wave number k_x to be determined). Equations (1.31) can be expressed through dimensionless parameters $\tilde{k}_x = ak_x,\ \tilde{k} = kd$, $\tilde{d} = d/a$ and $\xi = Z_0 \sigma d$:

$$\frac{Cth(\tilde{k}_x)}{\tilde{k}_x} = -\tilde{d}\,\frac{th\left(\sqrt{-j\xi\tilde{k}}\right)}{\sqrt{-j\xi\tilde{k}}} \quad (1.32a)$$

$$\frac{Th(\tilde{k}_x)}{\tilde{k}_x} = \tilde{d}\sqrt{-j\xi\tilde{k}}\, Cth\left(\sqrt{-j\xi\tilde{k}}\right)/\tilde{k}^2 \quad (1.32b)$$

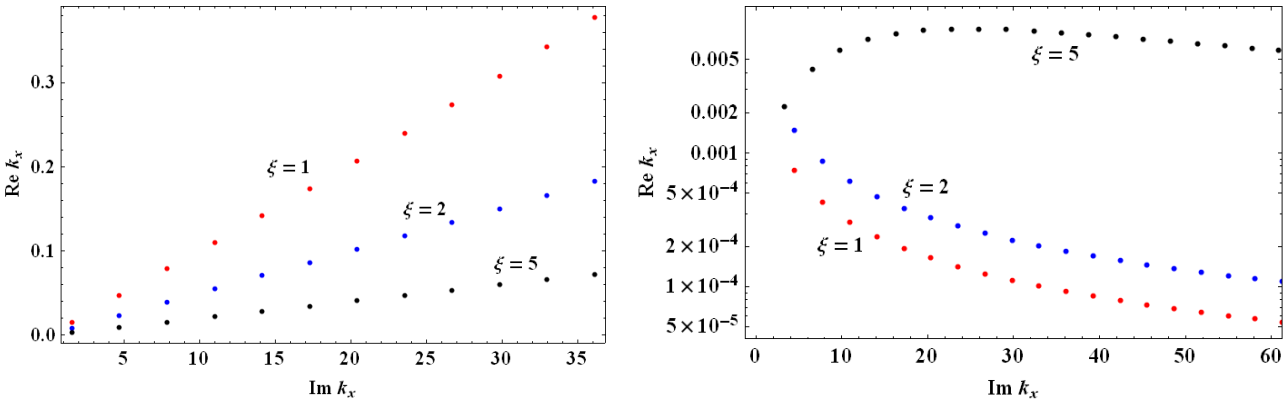

Fig.1.6: Eigenvalues of a planar two-layer structure. Solutions of equation 1.32a (left) and 1.32b (right) for different values of parameter ξ ($\xi = 1,\ 2\ and\ 5$) at a resonance frequency $\tilde{k} = k_{rez}\tilde{d} = \sqrt{d/a}$, $\tilde{d} = 10^{-4}$.

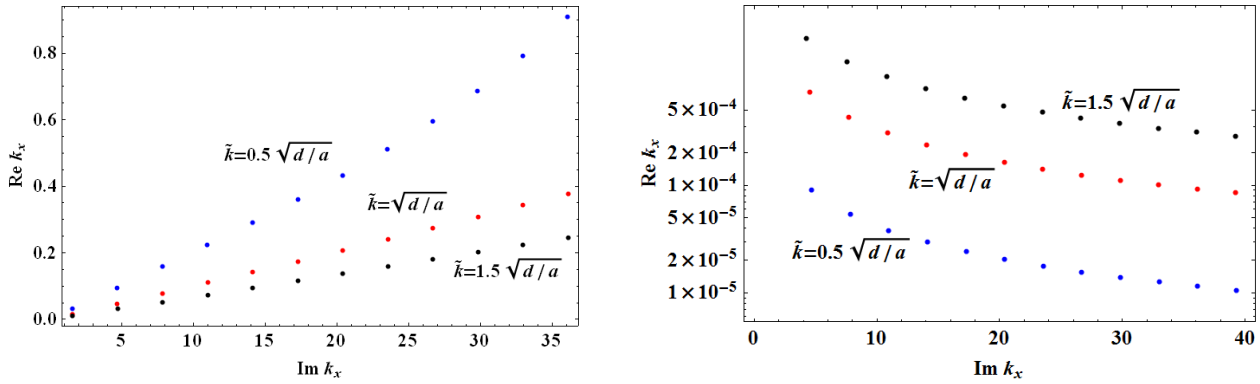

Fig.1.7: Eigenvalues of a planar two-layer structure. Solutions of equation 1.32a (left) and 1.32b (right) in the case of $\xi = 1$ for several values of frequency: $\tilde{k} = k_{rez}\tilde{d} = \sqrt{d/a}$, $\tilde{k} = 0.5\sqrt{d/a} < k_{rez}\tilde{d}$ and $\tilde{k} = 1.5\sqrt{d/a} > k_{rez}\tilde{d}$; $\tilde{d} = 10^{-4}$.

Figures 1.6 and 1.7 show the eigenvalue distributions of the synchronous mode of a two-layer planar structure. On the horizontal and vertical axes, respectively, the imaginary and real components of the eigenvalues are plotted on the graphs. The graphs are a result of the exact solution of Equations (1.32a, b). For small right-hand sides of equations (1.32), their asymptotic solution can be represented as the sum of the solution for ideally conducting plates ($k_{x0a} = j\,\pi/2 + j\pi(n-1)$ for Equation (1.32a) and $k_{x0b} = j\pi n$ for Equation (1.32b), $n = 1,2,4,\ldots$) and a small additive $\alpha_{a(b)}$, taking into account the presence of the inner coating:

$$k_{xa(b)} = jk_{x0a(b)} + \alpha_{a(b)},\ \ \alpha_{a(b)} = -j\frac{d_{a(b)}k_{0a(b)}}{1\pm d_{a(b)}} \tag{1.33}$$

where

$$d_a = \tilde{d}\,th\left(\sqrt{-j\xi\tilde{k}}\right)\Big/\sqrt{-j\xi\tilde{k}},\ \ d_b = \tilde{d}\sqrt{-j\xi\tilde{k}}\,Cth\left(\sqrt{-j\xi\tilde{k}}\right)/\tilde{k}^2 \tag{1.34}$$

The smallness of parameters $d_{a(b)}$ (1.34) is conditioned not only by the small relative thickness of the layer $\tilde{d}$, but also by the smallness of the other factors included in this parameter. Thus, for $\tilde{d} = 10^{-4}$ and $\xi = 1$ at the resonant frequency $\tilde{k} = \sqrt{d/a}$, the parameter d_b is of the order of unity ($\lfloor d_b \rfloor \approx 1$).

The eigenvalues k_{xa} (solutions of the equation (1.32a)) within the parameters shown in Figures 1.6, 1.7 (left), are approximated quite well by the formula (1.33). They are characterized by imaginary components close enough to the eigenvalues of the structure consisting of two parallel ideally conducting planes ($Imk_{xa} \approx k_{xa0}$), and by small real additions, the values of which decrease along with the increase of ξ parameter (Fig.1.6, left). We note that for fixed values of the parameter ξ, small real corrections are linearly increasing along with the increase of imaginary components (Fig. 1.6, 1,7, left) on x axis and decreases with increasing frequency (Fig. 1,7, left).

The behavior of k_b eigenvalue (solutions of equation (1.32b)) sequences is much more complicated. Their real components are two or three orders of magnitude smaller than the corresponding roots of equation (1.32a). For small ξ ($\xi = 1$ and $\xi = 2$ on Figure 1.6, right) they exponentially decrease along with the increase of imaginary components, deposited on the horizontal axis. With an increase of the parameter ξ, the lower values begin to increase to a certain limit, and then the increase goes down ($\xi = 5$ on Figure 1.6, right). In contrast to the eigenvalues of k_a (solutions of equation (1.32a)), there is a general increase of the real components of eigenvalues along with the increase of ξ parameter (Figure 1.6, right). The reverse order is also valid for fixed values of ξ: lower frequencies correspond to smaller values of the real components of the eigenvalues k_b. In contrast to the real values of k_a, they increase along with the frequency increase (Fig. 1.7, right).

The essential difference between the imaginary components of the eigenvalues k_b and the corresponding values for ideally conducting parallel planes is explained by the magnitude of the parameter d_b (1.34): its smallness is ensured at very low relative thicknesses of the metallic layer $\tilde{d}$ $(\tilde{d} \ll 1)$ or at sufficiently high frequencies $(\tilde{k} \gg \tilde{k}_{rez})$.

1.6 Summary

The first chapter establishes the connection between the radiation of a charged particle and the synchronous electromagnetic eigenmodes of two-layer cylindrical and flat metal structures.

For a two-layer metal cylindrical waveguide, it is shown, that a single slowly-propagating (with phase velocity equal to the speed of light) TM_{01} mode at certain frequency (resonant frequency $k = \sqrt{1/r_0 d}$, r_0 inner radius of waveguide, d inner layer thickness) is in phase with a radiation field of a charged particle and synchronized with the ultra-relativistic particle, moving along the waveguide axis. This circumstance is clearly demonstrated in Figure 1.2, where only one dispersion curve, corresponding to the above-mentioned mode, intersects a line describing the phase velocity equal to the speed of light.

The important results of this chapter also include the calculation of the attenuation coefficient of the synchronous mode for the resonance frequency (Eq. 1.8), which is defined as the real component of its phase.

The remarkable properties of the phase of synchronous mode, presented in Figure 1.3, are also determined.

The second main direction of this chapter is to investigate the mechanism of synchronization of the electromagnetic eigenoscillations of a two-layer flat metallic structure.

Equations for the eigenvalue numbers of free vibrations in the structure under consideration are obtained. A subsystem of free oscillations, synchronous with a particle, moving along a rectilinear trajectory parallel to the symmetry plane of structure, is distinguished from the complete set of free oscillations. Equations for eigenvalues are obtained both for a complete system of free oscillations and for their synchronous

subsystem. A unique relationship is established between the roots of the equations for synchronous oscillations and the complex poles of the integrand for the longitudinal impedance. Based on graphic constructions the behavioral regularities of eigenvalues are analyzed.

Important difference between the mechanisms of formation of synchronous oscillations for two-layer cylindrical and planar structures should be mentioned. In the first case, we have a single synchronous mode, with synchronization being achieved only at the resonant frequency $k = \sqrt{2/r_0 d}$. In the second case, there is an infinite set of eigen-oscillations, synchronous on the entire infinite frequency range. The radiation field of a particle is formed by the total contribution of the entire infinite sequence of natural synchronous oscillations of the structure.

As will be shown in the second chapter, the result of the total contribution of synchronous oscillations is radiation with a narrow-band frequency spectrum and a single resonant frequency $k = \sqrt{1/ad}$.

Chapter 2: Accelerating structures with flat geometry

2.1 Introduction

Impedances and wake functions in multilayer cylindrical structures are studied in [72]. It is shown that under certain conditions there is a narrow-band longitudinal impedance in the structure. The study of dispersive relations of a two-layer cylindrical structure shows that in the same conditions the structure becomes a high frequency, single slowly ($v < c$) traveling wave structure. Single-mode structures are good candidates both for novel accelerating structures and for being sources of high frequency monochromatic radiation. As it is shown in previous chapter, a single-mode structure can be used also for bunch compression and for microbunching. To be a high frequency single-mode structure, it requires a high accuracy μm – sub-μm low conductivity internal coating, and an inner diameter of about several mm, which is technically a complex problem for structures with mm diameters.

In this chapter multilayer flat metallic structure is studied as an alternative of the abovementioned cylindrical structure. The longitudinal impedance and dispersive relations of the structure are presented, wake fields generated by a particle travelling through the structure are observed. Analyses of symmetrical and asymmetrical multilayer flat waveguides are performed. Conditions in which the longitudinal impedance has a narrow-band resonance are obtained. Comparison of properties of multilayer flat metallic structure with cylindrical structure is done.

To calculate electromagnetic fields, the field matching technique, that implies the continuity of the tangential components of electric and magnetic fields at the borders of the layers, is used for solving Maxwell equation. The matrix formalism described in [72] is used to couple electromagnetic field tangential components in two borders of a layer. The longitudinal impedance of the structure and wake fields in it are obtained via Fourier inverse transformation of electromagnetic fields.

2.2 Multilayer flat structure

We will start with the most general case: a structure consisting of two parallel multilayer infinite plates (Figure 2.1). The boundaries between layers are infinite parallel planes. The number of layers in the top $n^{(t)}$ and bottom $n^{(b)}$ plates can generally be unequal ($n^{(t)} \neq n^{(b)}$). The filling of layers may be both dielectric or metallic and in general is characterized by a static complex dielectric permittivity $\varepsilon_i^{(u)}, i = 1,2,..n^{(u)}, u = t, b$, magnetic permeability $\mu_i^{(u)}$and conductivity $\sigma_i^{(u)}$. The dielectric constant material layer can be written as $\tilde{\varepsilon}_i^{(u)} = \varepsilon_i^{(u)} + j\,\sigma_i^{(u)}/\omega$, where ω is the frequency. For the majority of highly conductive metals $\varepsilon_i^{(u)} = \varepsilon_0$; for non-magnetic materials $\mu_i^{(u)} = \mu_0$ (ε_0, μ_0 permittivity and magnetic permeability of vacuum). The thickness of i-th layer is $d_i^{(u)}$. The distance from the symmetry plane of the vacuum chamber to the boundary planes, separating layers are equal to $a_i^{(u)}$; $a_{i+1}^{(u)} = a_i^{(u)} + d_i^{(u)}$, $i = 1,2,3,\ldots n^{(u)}$ (for upper half-space). The upper and lower unbounded regions can be filled by an arbitrary medium, the electromagnetic properties of which are characterized by parameters $\tilde{\varepsilon}_{n^{(u)}+1}^{(u)} = \varepsilon_{n^{(u)}+1}^{(u)} + j\,\sigma_{n^{(u)}+1}^{(u)}/\omega$, $\mu_{n^{(u)}+1}^{(u)} = \mu_0$.

The point-like charge is traveling through the layer metallic tube with velocity $\boldsymbol{v}$ parallel to the z-axis at vertical offset Δ.

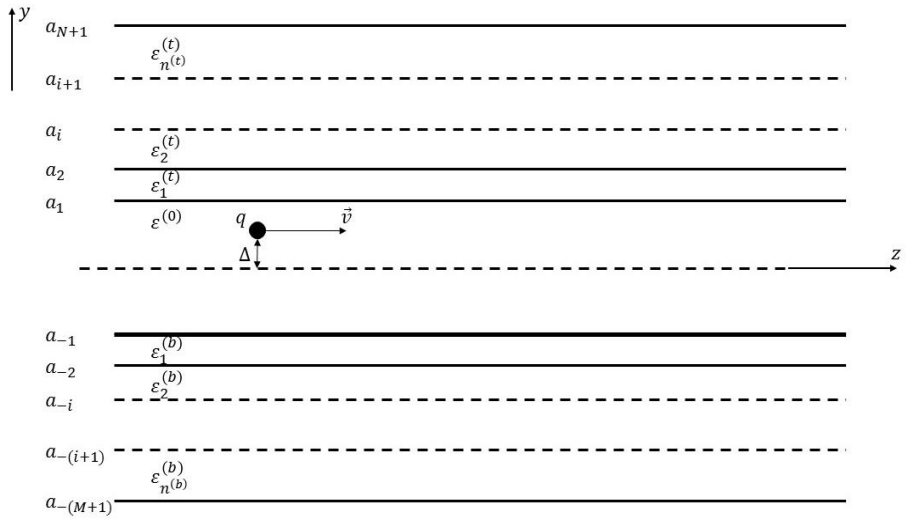

Figure 2.1: Geometry of multilayer flat metallic structure.

Maxwell's equations must be solved to calculate EM fields excited by the point charge. Cartesian coordinates $\vec{r} = (x, y, z)$ are used, where y is the direction of vertical axis. For $\left(n^{(t)}, n^{(b)}\right)$-layer tube there are $n^{(t)} + n^{(b)} + 3$ regions (including the inner and two outer regions of the structure) and $n^{(t)} + n^{(b)} + 2$ borders. The complete number of matching equations is $4\left(n^{(t)} + n^{(b)} + 2\right)$ with $4\left(n^{(t)} + n^{(b)} + 2\right)$ unknown coefficients as in each border there are four boundary conditions that match tangential (E_x, E_z, B_x, B_z) components of electromagnetic fields.

Radiation fields are searched by the method of partial areas [92]. The electromagnetic fields are derived by differently presenting the fields in three regions: charge existing region ($-a_{-1} \le y \le a_1$), metallic layers of the structure ($-a_{-\mathrm{n}^{(b)}} < y < -a_{-1}$, $a_1 < y < a_{\mathrm{n}^{(t)}}$) and outer vacuum region ($y < -\mathrm{a}_{-\mathrm{n}^{(b)}}$, $y > \mathrm{a}_{\mathrm{n}^{(t)}}$). In all regions the solution is sought in the form of general solution of the homogeneous Maxwell's equations except for the area between the plates. Here, a particular solution of inhomogeneous Maxwell's equations is added to the general solution of the homogeneous Maxwell's equations.

The electromagnetic fields and point charge are presented via Fourier transformation as:

$$\begin{aligned} E(x, y, z) &= \int_{-\infty}^{\infty} \widetilde{\boldsymbol{E}}(k_x, y, k_z) e^{ik_x x} e^{ik(z-ct)} dk_x dk_z \\ \rho(x, y, z) &= \int_{-\infty}^{\infty} \tilde{\rho}(k_x, y, k_z) e^{ik_x x} e^{ik_z z} dk_x dk_z \end{aligned} \tag{2.1}$$

where $k = {}^{\omega}/_{t}$ is the wave number.

Boundary conditions state that tangential components of full electric and magnetic fields should be continuous at layer boundaries.

$$\begin{aligned} \mathrm{E}_x^i(\pm a_i) &= \mathrm{E}_x^{i+1}(\pm a_i) \\ \mathrm{E}_z^i(\pm a_i) &= \mathrm{E}_z^{i+1}(\pm a_i) \\ \mathrm{B}_x^i(\pm a_i) &= \mathrm{B}_x^{i+1}(\pm a_i) \\ \mathrm{B}_z^i(\pm a_i) &= \mathrm{B}_z^{i+1}(\pm a_i) \end{aligned} \tag{2.2}$$

where $+$ and $-$ signs correspond to layer boundaries in the upper and lower regions, respectively.

An electric charge traveling in the structure produces an electromagnetic field, which can be presented as a sum of two parts:

$$\boldsymbol{E_{tot} = E_p + E}, \quad \boldsymbol{B_{tot} = B_p + B} \tag{2.3}$$

where $\boldsymbol{E_p}, \boldsymbol{B_p}$ are the electric and magnetic fields in the case of perfectly conducting plates and $\boldsymbol{E}, \boldsymbol{B}$ are the solutions of source free Maxwell's equations with a metallic current $\boldsymbol{j} = \sigma \boldsymbol{E}$. The dependence of the last ones on source particles is determined by boundary conditions.

Firstly, electric $\boldsymbol{E_p}$ and magnetic $\boldsymbol{B_p}$ fields in the perfectly conducting parallel plates with a static charge in the structure are calculated, then the fields, when there is a charge traveling in the direction of structure axis, can be obtained via Lorentz transformation [92].

Maxwell's equations for the structure with a static charge ρ in it are:

$$\begin{aligned} \nabla \cdot \boldsymbol{E_p} &= \frac{\rho}{\varepsilon_0} \\ \nabla \cdot \boldsymbol{B_p} &= 0 \\ \nabla \times \boldsymbol{E_p} &= 0 \\ \nabla \times \boldsymbol{B_p} &= 0 \end{aligned} \tag{2.4}$$

where ∇ is the nabla operator.

Using Fourier transformation in Maxwell's equations and expressing electric field x and y components via z component, the wave equation for a point charge can be derived:

$$\frac{\partial^2 E_{p_z}}{\partial y^2} - \alpha^2 E_{p_z} = \frac{q}{4\pi^2 \varepsilon_0} i k_z \delta(y - \Delta) \tag{2.5}$$

where $\alpha = \sqrt{{k_x}^2 + {k_z}^2}$ and Δ is the point charge deviation from the center of y axis.

The solution of Eq. 2.5 is a sum of homogenous equation solution ($\tilde{E}_{z,h}$) and a particular solution ($\tilde{E}_{z,p}$).

Presenting the solution of homogenous part as a sum of hyperbolic cosine and sine with unknown coefficients, and finding a particular solution by integrating two parts of the wave equation, the solution can be obtained.

$$E_{p_z}^{\pm}(k_x, y, k_z) = -\frac{q i k_z}{4\pi^2 \alpha \varepsilon_0} \frac{\sinh\big(\alpha(a \pm \Delta)\big) \sinh\big(\alpha(a \mp y)\big)}{\sinh(2\alpha a)} \tag{2.6}$$

where + sign stands for an electric field in upper part of the structure ($y > \Delta$) and – for an electric field in lower part ($y < \Delta$).

x and y components of the electric field can be obtained via Faraday's low and magnetic field is zero for a static charge.

$$\begin{aligned} E_{p_x}^{\pm}(k_x, y, k_z) &= -\frac{qik_x}{4\pi^2\alpha\varepsilon_0}\frac{sinh\big(\alpha(a\mp y)\big)\,sinh\big(\alpha(a\pm\Delta)\big)}{sinh(2\alpha a)} \\ E_{p_y}^{\pm}(k_x, y, k_z) &= \pm\frac{q}{4\pi^2\varepsilon_0}\frac{cos(\alpha(a\mp y))\,sinh(\alpha(a\pm\Delta))}{sinh(2\alpha a)} \end{aligned} \tag{2.7}$$

The Fourier components of the electromagnetic fields of a moving charge can be obtained via Lorentz transformation:

$$\begin{aligned} E_{p_z}^{\pm}(k_x, y, k_z) &= -\frac{1}{\gamma^2}\frac{qjk_z}{4\pi^2 k_x\varepsilon_0}\frac{\sinh\big(k_x(a\pm\Delta)\big)\sinh\big(k_x(a\mp y)\big)}{\sinh(2k_x a)} \\ E_{p_x}^{\pm}(k_x, y, k_z) &= \gamma^2\frac{k_x}{k_z}E_{p_z}^{\pm}(k_x, y, k_z) \\ E_{p_y}^{\pm}(k_x, y, k_z) &= \pm\gamma^2 j\frac{k_x}{k_z}\coth(k_x(a\mp y))\,E_{p_z}^{\pm}(k_x, y, k_z) \\ B_{p_z}^{\pm}(x, y, z) &= 0 \\ B_{p_x}^{\pm}(k_x, y, k_z) &= \frac{v}{c^2}E_{p_y}^{\pm}(k_x, y, k_z) \\ B_{p_y}^{\pm}(k_x, y, k_z) &= -\frac{v}{c^2}E_{p_x}^{\pm}(k_x, y, k_z) \end{aligned} \tag{2.8}$$

Note that the variable of integration is replaced by $k_z \to k_z'/\gamma$ and $\alpha = \sqrt{{k_x}^2 + \left(\frac{k_z'}{\gamma}\right)^2} \approx k_x$.

We write fields in Eq. 2.8 in the form of plane waves:

$$\begin{aligned} E_{p_{x,y,z}} &= E_{1,p_{x,y,z}} + E_{2,p_{x,y,z}} = A_{1,x,y,z}^{(\pm)}e^{(\mp)ka}e^{-ky} + A_{2,x,y,z}^{(\pm)}e^{(\pm)ka}e^{-ky} \\ B_{p_{x,y,z}} &= B_{1,p_{x,y,z}} + B_{2,p_{x,y,z}} = B_{1,x,y,z}^{(\pm)}e^{(\mp)ka}e^{-ky} + B_{2,x,y,z}^{(\pm)}e^{(\pm)ka}e^{-ky} \end{aligned} \tag{2.9}$$

where

$$\begin{aligned} A_{1,z}^{(\pm)} &= -j\gamma^{-2}\frac{qk_z}{8\pi^2\varepsilon_0 k}\cosh(2ka)\sinh\big(k(a\pm\Delta)\big) & A_{2,z}^{(\pm)} &= -A_{1,,z}^{(\pm)} \\ A_{1,x}^{(\pm)} &= -j\frac{qk_x}{8\pi^2\varepsilon_0 k}Csh(2ka)Sh\{k(a\pm\Delta)\} = \gamma^2 A_{1,z}^{(\pm)} & A_{2,z}^{(\pm)} &= -A_{2,z}^{(\pm)} \\ A_{1,y}^{(\pm)} &= \pm\frac{q}{8\pi^2\varepsilon_0}Csh(2ka)Sh\{k(a\pm\Delta)\} & A_{2,y}^{(\pm)} &= A_{2,,y}^{(\pm)} \end{aligned} \tag{2.10}$$

On the metallic surfaces, the electromagnetic field components are:

$$
\begin{aligned}
E_{p_x}(k_x, \pm a, k_z) &= E_{p_z}(k_x, \pm a, k_z) = 0 \\
E_{p_y}(k_x, \pm a, k_z) &= \frac{q}{4\pi^2\varepsilon_0}\frac{\sinh\left(k_x(\Delta \pm a)\right)}{\sinh(2k_x a)} \\
B_{p_x}(k_x, \pm a, k_z) &= \frac{q}{4\pi^2\varepsilon_0}\frac{v}{c^2}\frac{\sinh\left(k_x(\Delta \pm a)\right)}{\sinh(2k_x a)} \\
B_{p_y}(k_x, \pm a, k_z) &= B_{p_z}(k_x, \pm a, k_z) = 0
\end{aligned}
\tag{2.11}
$$

The only non-zero tangential component at the boundaries $y = \pm a$ is a component B_{p_x}, which in ultrarelativistic approximation $(v \to c)$ is

$$
B_{p_x}(k_x, \pm a, k_z) = \frac{q}{4\pi^2\varepsilon_0 c}\frac{\sinh\left(k_x(\Delta \pm a)\right)}{\sinh(2k_x a)} \tag{2.12}
$$

As it was mentioned, the total electromagnetic field excited by a point charge traveling in the multilayer structure was presented as a sum of two parts. Now the second part of total electromagnetic field will be calculated, i.e. solutions of the source free Maxwell's equations with a metallic current $\boldsymbol{j} = \sigma \boldsymbol{E}$. The fields inside layers are sought in the form of a general solution of the homogenous Maxwell's equations.

$$
\begin{aligned}
\boldsymbol{E}^{(i)}(x, y, z) &= \boldsymbol{E}_1^{(i)}(x, y, z) + \boldsymbol{E}_2^{(i)}(x, y, z) \\
\boldsymbol{B}^{(i)}(x, y, z) &= \boldsymbol{B}_1^{(i)}(x, y, z) + \boldsymbol{B}_2^{(i)}(x, y, z)
\end{aligned}
\tag{2.13}
$$

where

$$
\begin{aligned}
\boldsymbol{E}_{1,2}^{(i)}(x, y, z) &= \int_{-\infty}^{\infty}\int_{-\infty}^{\infty} \boldsymbol{E}_{1,2}^{(i)}(k_x, y, k_z) e^{j\left(k_x x + k_z(z - vt)\right)}\, dk_x dk \\
\boldsymbol{B}_{1,2}^{(i)}(x, y, z) &= \int_{-\infty}^{\infty}\int_{-\infty}^{\infty} \boldsymbol{B}_{1,2}^{(i)}(k_x, y, k_z) e^{j\left(k_x x + k_z(z - vt)\right)}\, dk_x dk
\end{aligned}
\tag{2.14}
$$

with

$$
\begin{aligned}
\boldsymbol{E}_{1,2}^{(i)}(k_x, y, k_z) &= \boldsymbol{A}_{1,2}^{(i)} e^{\mp k_y^{(i)} y} \\
\boldsymbol{B}_{1,2}^{(i)}(k_x, y, k_z) &= \frac{e^{-j\left(k_x x + k_z(z - vt)\right)}}{j k_z v} rot\left[\boldsymbol{E}_{1,2}^{(i)}(k_x, y, k_z) e^{j\left(k_x x + k_z(z - vt)\right)}\right]
\end{aligned}
\tag{2.15}
$$

For the inner region $(-a_{-1} < y < a_1)$ we should add the partial solution $\left(\boldsymbol{E}_p, \boldsymbol{B}_p\right)$ of inhomogeneous Maxwell's equation (Eq. 2.8) to the general solution of the homogeneous one:

$$\boldsymbol{E}^{(0)}(x,y,z) = \boldsymbol{E}_1^{(i)}(x,y,z) + \boldsymbol{E}_2^{(i)}(x,y,z) + \boldsymbol{E}_p(x,y,z)$$
$$\boldsymbol{B}^{(0)}(x,y,z) = \boldsymbol{B}_1^{(i)}(x,y,z) + \boldsymbol{B}_2^{(i)}(x,y,z) + \boldsymbol{B}_p(x,y,z) \quad (2.16)$$

Finally, for the upper and lower outer regions, fields are sought to be vanishing in infinity (at $y \to \pm\infty$)

$$\boldsymbol{E}^{(n^{(t)}+1)}(x,y,z) = \boldsymbol{E}_1^{(n^{(t)}+1)}(x,y,z)$$
$$\boldsymbol{B}^{(n^{(t)}+1)}(x,y,z) = \boldsymbol{B}_1^{(n^{(t)}+1)}(x,y,z)$$
$$\boldsymbol{E}^{(-n^{(b)}-1)}(x,y,z) = \boldsymbol{E}_2^{(-n^{(b)}-1)}(x,y,z) \quad (2.17)$$
$$\boldsymbol{B}^{(-n^{(b)}-1)}(x,y,z) = \boldsymbol{B}_2^{(-n^{(b)}-1)}(x,y,z)$$

for top $\left(y > a_{n^{(t)}+1}\right)$ and bottom $\left(y < -a_{-n^{(b)}-1}\right)$ regions, respectively.

As it is mentioned, we obtain a system of $4(N+M+2)$ equations for the same number of unknown amplitudes. Amplitudes $A_{z,1}^i$ and $A_{z,2}^i$ can be presented by $A_{x,1}^i, A_{y,1}^i$ and $A_{x,2}^i, A_{y,2}^i$ $A_{x,1}$ via Gauss's low

$$A_{z,1}^i = -\frac{k_x A_{x,1}^i + i k_y^i A_{y,1}^i}{k_z}$$
$$A_{z,2}^i = -\frac{k_x A_{x,2}^i - i k_y^i A_{y,2}^i}{k_z} \quad (2.18)$$

and magnetic field components can be derived via Faraday's low.

To determine the electromagnetic field we will use the field matching technique that implies the continuity of the tangential components of electromagnetic fields at the borders of layers ($y = \pm a_i$). We are interested in tangential components of fields, so we will introduce the tangential field vector $\hat{T}^i\left({E_x}^i, {E_z}^i, c{B_x}^i, c{B_z}^i\right)$. We will use the matrix approach introduced in [72] to obtain electromagnetic fields in the vacuum region.

Connection between the components of the fields and amplitudes is realized by using the basic transformation matrixes:

$$\widehat{W}_1^{(i)}(y) = \frac{e^{-k_y^i y}}{{k_z}^2}\begin{pmatrix} {k_z}^2 & 0 & 0 & 0 \\ -k_x k_z & -ik_y^i k_z & 0 & 0 \\ -ik_y^i k_x & {k_y^i}^2 - {k_z}^2 & 0 & 0 \\ -ik_y^i k_z & k_x k_z & 0 & 0 \end{pmatrix} \tag{2.19}$$

$$\widehat{W}_2^{(i)}(y) = \frac{e^{k_y^i y}}{{k_z}^2}\begin{pmatrix} 0 & 0 & {k_z}^2 & 0 \\ 0 & 0 & -k_x k_z & -ik_y^i k_z \\ 0 & 0 & ik_y^i k_x & {k_y^i}^2 - {k_z}^2 \\ 0 & 0 & -ik_y^i k_z & k_x k_z \end{pmatrix} \tag{2.20}$$

$$\widehat{W}^{(i)}(y) = \widehat{W}_1^{(i)}(y) + \widehat{W}_2^{(i)}(y) \tag{2.21}$$

where $k_y^{(i)} = k_x^2 + \left(1 - \varepsilon^{(i)}\mu^{(i)}v^2\right)k_z^2$.

Let us establish a connection between the field values on the lower borders of neighboring layers. The fields on upper and lower borders of the i-th layer of the upper half-space can be expressed in terms of values having the same amplitudes:

$$\begin{matrix} \hat{T}^i(a_i) = \widehat{W}_1^i(a_i)\hat{A}^i \\ \hat{T}^i(a_{i+1}) = \widehat{W}_1^i(a_{i+1})\hat{A}^i \end{matrix} \Rightarrow \quad \hat{T}^i(a_{i+1}) = \widehat{W}_1^i(a_{i+1})\widehat{W}_1^i(a_i)^{-1}\hat{T}^i(a_i) \tag{2.22}$$

From field tangential component continuity ($\hat{T}^{i+1}(a_{i+1}) = \hat{T}^i(a_{i+1})$), one obtains

$$\hat{T}^{i+1}(a_{i+1}) = \widehat{W}_1^i(a_{i+1})\widehat{W}_1^i(a_i)^{-1}\hat{T}^i(a_i) \tag{2.23}$$

Consistent application of (2.23) for upper half-spaces gives

$$\hat{T}^{n^{(t)}+1}\left(a_{n^{(t)}+1}\right) = Q^{(t)}\hat{T}^0(a_1) \tag{2.24}$$

where $Q^{(t)} = \prod_{i=1}^{n^{(t)}} Q_i^{(t)}$ and $Q_i^{(t)} = \widehat{W}^{(i)}(a_{i+1})\widehat{W}^{(i)}(a_i)^{-1}$.

Similar relation can be obtained for lower half-space

$$\hat{T}^{\left(-\left(n^{(b)}+1\right)\right)}\left(-a_{-\left(n^{(b)}+1\right)}\right) = Q^{(b)}\hat{T}^{(0)}(-a_{-1}) \tag{2.25}$$

where $Q^{(b)} = \prod_{i=1}^{n^{(b)}} Q_i^{(b)}$, $Q_i^{(b)} = \widehat{W}^{(-i)}\left(-a_{-(i+1)}\right)\widehat{W}^{(-i)}(-a_{-i})^{-1}$.

For the symmetrical case $Q_i^{(b)} = {Q_i^{(t)}}^{-1}$ and $Q^{(b)} = \prod_{i=1}^{n} {Q_i^{(t)}}^{-1}$.

Given the matching conditions on the borders of the plates, we finally have

$$\widehat{W}_1^{\left(n^{(t)}+1\right)}\left(a_{n^{(t)}+1}\right)\hat{A}^{(tb)} = Q^t\left[\widehat{W}^{(0)}(a_1)\hat{A}^{(0)} + \hat{B}^{(t)}\right] \tag{2.26}$$

$$\widehat{W}_2^{\left(-\left(n^{(b)}+1\right)\right)}\left(-a_{-\left(n^{(b)}+1\right)}\right)\hat{A}^{(tb)} = Q^b\left[\widehat{W}^{(0)}(-a_{-1})\hat{A}^{(0)} + \hat{B}^{(b)}\right] \tag{2.27}$$

where $\hat{B}^{(t,b)}$ and $\hat{A}^{(t,b)}$ are the single-column matrixes:

$$\begin{aligned}\hat{B}^{(t,b)} &= \left\{\{0\},\{0\},\left\{2k_y^{(0)} v\,\mathrm{csch}\left(2k_y^{(0)}a\right)\sinh\left[k_y^{(0)}(\Delta \pm a_1)\right]\right\},\{0\}\right\}\\ \hat{A}^{(tb)} &= \left\{\left\{A_{x,1}^{\left(n^{(t)}+1\right)}\right\},\left\{A_{y,1}^{\left(n^{(t)}+1\right)}\right\},\left\{A_{x,2}^{\left(-\left(n^{(b)}+1\right)\right)}\right\},\left\{A_{y,2}^{\left(-\left(n^{(b)}+1\right)\right)}\right\}\right\}\end{aligned} \tag{2.28}$$

In Eq. 2.9 and Eq. 2.10, the condition that fields are vanishing on $y = \pm\infty$ is taken into account.

The amplitudes $\hat{A}^{(0)}$ may be expressed in terms of $\hat{A}^{(tb)}$ amplitudes, using Eq. 2.26 and Eq. 2.27

$$\begin{aligned}\hat{A}^{(0)} &= \hat{G}^t\hat{A}^{(tb)} - \widehat{W}^{(0)}(a_1)^{-1}\hat{B}^{(t)}\\ \hat{A}^{(0)} &= \hat{G}^b\hat{A}^{(tb)} - \widehat{W}^{(0)}(-a_{-1})^{-1}\hat{B}^{(b)}\end{aligned} \tag{2.29}$$

where

$$\begin{aligned}\hat{G}^t &= \widehat{W}^{(0)}(a_1)^{-1}{T^t}^{-1}\widehat{W}_1^{\left(n^{(t)}+1\right)}\left(a_{n^{(t)}+1}\right)\\ \hat{G}^b &= \widehat{W}^{(0)}(-a_{-1})^{-1}{T^b}^{-1}\widehat{W}_2^{\left(-\left(n^{(b)}+1\right)\right)}\left(-a_{-\left(n^{(b)}+1\right)}\right)\end{aligned} \tag{2.30}$$

Eliminating the outer layer coefficients, we obtain explicit expressions for the amplitudes of the particle radiation field in the space between the plates:

$$\hat{A}^{(0)} = \frac{1}{2}\left(\hat{G}^{(+)}{\hat{G}^{(-)}}^{-1}\hat{D}^{(-)} - \hat{D}^{(+)}\right) \tag{2.31}$$

with

$$\hat{G}^{(\pm)} = \hat{G}^t \pm \hat{G}^b,\ \hat{D}^{(\pm)} = \widehat{W}^{(0)}(a_1)^{-1}\hat{B}^{(t)} \pm \widehat{W}^{(0)}(-a_{-1})^{-1}\hat{B}^{(b)} \tag{2.32}$$

Amplitudes of the radiation field for the structure with an arbitrary number of layers in each of the plates can numerically be obtained by Eq. 2.31. The particle velocity can also be arbitrary.

2.3 Two-layer flat structure

Note that in the symmetric case $\left(a_i = a_{-i},\ k_y^{(i)} = k_y^{(-i)},\ n^{(t)} = n^{(b)}\right)\ U_i^{(b)} = U_i^{(t)^{-1}}$ and $Q^{(b)} = Q^{(t)^{-1}}$. For some important special cases, it is possible to obtain explicit expressions.

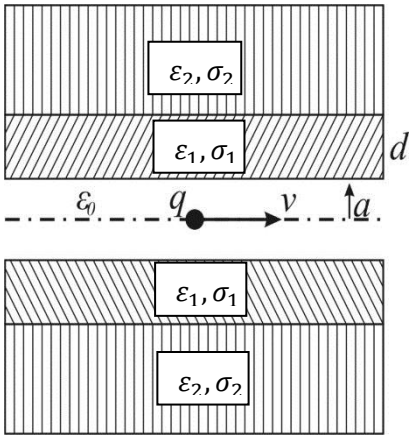

Figure 2.2: Two-layer flat structure. Geometry and electromagnetic parameters.

An important special case is a symmetrical two-layer structure with unbounded external walls (Figure 2.2). We write the amplitudes of the longitudinal electric component of the radiation field of the particles in the vacuum region between the plates (corresponds to Eq. 2.15 for $i = 0$)

$$A_{z,1,2}^{(0)} = A_C \cosh\left(k_y^{(0)}\Delta\right) \mp A_S \sinh\left(k_y^{(0)}\Delta\right) \tag{2.33}$$

where

$$A_C = j\frac{qk_z}{16\pi^2\varepsilon_0}\frac{v^2}{c^2}\frac{A+B\ \tanh\left(k_y^{(0)}a_1\right)}{D_1^C D_2^C}, \quad A_S = j\frac{qk_z}{16\pi^2\varepsilon_0}\frac{v^2}{c^2}\frac{A+B\ \coth\left(k_y^{(0)}a_1\right)}{D_1^S D_2^S} \tag{2.34}$$

The following notations are made in Eq. 2.34

$$A = k_y^{(0)}\left[\left(k_y^{(1)^2} - k_y^{(2)^2}\right)\left(k_x^2 K_1^2 - k_y^{(1)^2}k_z^2\right) + \left(k_y^{(1)^2} - k_x^2\right)P\right]$$

$$B = 2k_y^{(1)}\left(k_x^2 - {k_y^{(0)}}^2\right)S_1\tilde{S}_2$$

$$D_1^C = k_y^{(1)}S_2\cosh\left(k_y^{(0)}a_1\right) + k_y^{(0)}S_1\sinh\left(k_y^{(0)}a_1\right)$$

$$D_1^S = k_y^{(1)}S_2\sinh\left(k_y^{(0)}a_1\right) + k_y^{(0)}S_1\cosh\left(k_y^{(0)}a_1\right)$$

$$D_2^C = k_y^{(0)}K_1^2\tilde{S}_1\cosh\left(k_y^{(0)}a_1\right) + k_y^{(1)}K_0^2\tilde{S}_2\sinh\left(k_y^{(0)}a_1\right)$$

$$D_2^S = k_y^{(0)}K_1^2\tilde{S}_1\sinh\left(k_y^{(0)}a_1\right) + k_y^{(1)}K_0^2\tilde{S}_2\cosh\left(k_y^{(0)}a_1\right) \qquad (2.35)$$

$$S_1 = k_y^{(1)}\cosh\left(k_y^{(1)}d\right) + k_y^{(2)}\sinh\left(k_y^{(1)}d\right)\, S_2 = k_y^{(2)}\cosh\left(k_y^{(1)}d\right) + k_y^{(1)}\sinh\left(k_y^{(1)}d\right)$$

$$\tilde{S}_1 = k_y^{(1)}K_2^2\cosh\left(k_y^{(1)}d\right) + k_y^{(2)}K_1^2\sinh\left(k_y^{(1)}d\right)\tilde{S}_2 = k_y^{(2)}K_1^2\cosh\left(k_y^{(1)}d\right) + k_y^{(1)}K_2^2\sinh\left(k_y^{(1)}d\right)$$

$$P = \left({k_y^{(2)}}^2K_1^2 + {k_y^{(1)}}^2K_2^2\right)\cosh\left(2k_y^{(1)}d\right) + k_y^{(1)}k_y^{(2)}(K_1^2 + K_2^2)\sinh\left(2k_y^{(1)}d\right)$$

$$K_i^2 = {k_y^{(i)}}^2 - k_x^2 - k_z^2, \quad i = 0,1,2$$

Expressions 2.33–2.35 are a generalization of the well-known result [92] on the two-layer structure for an arbitrary velocity of the particle. In the transition to single-layer unbounded plates $\left(k_y^{(1)} = k_y^{(2)}\right)$ the first term in A vanishes. In the transition to ultra-relativistic approximation $\left(k_y^{(0)} = k_x\right)$ factor B vanishes. The following are the values of field amplitudes for the structure, consisting of two unbounded parallel plates and an arbitrary particle velocity.

$$A_C = j\frac{qk_z}{8\pi^2\varepsilon_0}\frac{v^2}{c^2}\frac{\left(k_x^2-{k_y^{(1)}}^2\right)k_y^{(0)}+k_y^{(1)}\left(k_x^2-{k_y^{(0)}}^2\right)\tanh\left(k_y^{(0)}a_1\right)}{\left(k_y^{(1)}\cosh\left(k_y^{(0)}a_1\right)+k_y^{(0)}\sinh\left(k_y^{(0)}a_1\right)\right)\left(k_y^{(0)}K_1^2\cosh\left(k_y^{(0)}a_1\right)+k_y^{(1)}K_0^2\sinh\left(k_y^{(0)}a_1\right)\right)}$$
$$A_S = j\frac{qk_z}{8\pi^2\varepsilon_0}\frac{v^2}{c^2}\frac{\left(k_x^2-{k_y^{(1)}}^2\right)k_y^{(0)}+k_y^{(1)}\left(k_x^2-{k_y^{(0)}}^2\right)\coth\left(k_y^{(0)}a_1\right)}{\left(k_y^{(0)}\cosh\left(k_y^{(0)}a_1\right)+k_y^{(1)}\sinh\left(k_y^{(0)}a_1\right)\right)\left(k_y^{(1)}K_0^2\cosh\left(k_y^{(0)}a_1\right)+k_y^{(0)}K_1^2\sinh\left(k_y^{(0)}a_1\right)\right)} \qquad (2.36)$$

At $k_y^{(0)} = k_x$ and $v = c$ amplitudes in Eq. 2.36 coincide with the corresponding amplitudes in [92], obtained in the ultra-relativistic approximation.

In the case of high conductivity of outer layer, it can be considered as a perfect conductor. Transition to this case is made by means of equating to infinity the wave number $k_y^{(2)}$ in Eq. 2.34. In this case the field amplitudes are:

$$A_{1C} = j\frac{qk_z}{16\pi^2\varepsilon_0}\frac{v^2}{c^2}\frac{\left(k_x^2-k_y^{(1)^2}\right)k_y^{(0)}\sinh\left(2\,k_y^{(1)}d\right)+2k_y^{(1)}\left(k_y^{(0)^2}-k_x^2\right)\sinh^2\left(k_y^{(1)}d\right)\tanh\left(k_y^{(0)}a_1\right)}{R_1^C R_2^C}$$
$$A_{1S} = j\frac{qk_z}{16\pi^2\varepsilon_0}\frac{v^2}{c^2}\frac{\left(k_x^2-k_y^{(1)^2}\right)k_y^{(0)}\sinh\left(2\,k_y^{(1)}d\right)+2k_y^{(1)}\left(k_y^{(0)^2}-k_x^2\right)\sinh^2\left(k_y^{(1)}d\right)\coth\left(k_y^{(0)}a_1\right)}{R_1^S R_2^S} \quad (2.37)$$

where the following notations are made:

$$\begin{aligned} R_1^C &= k_y^{(1)}\cosh\left(k_y^{(1)}d\right)\cosh\left(k_y^{(0)}a_1\right)+k_y^{(0)}\sinh\left(k_y^{(1)}d\right)\sinh\left(k_y^{(0)}a_1\right)\\ R_1^S &= k_y^{(1)}\cosh\left(k_y^{(1)}d\right)\sinh\left(k_y^{(0)}a_1\right)+k_y^{(0)}\sinh\left(k_y^{(1)}d\right)\cosh\left(k_y^{(0)}a_1\right)\\ R_2^C &= k_y^{(0)}K_1^2\cosh\left(k_y^{(1)}d\right)\cosh\left(k_y^{(0)}a_1\right)+k_y^{(1)}K_0^2\sinh\left(k_y^{(1)}d\right)\sinh\left(k_y^{(0)}a_1\right)\\ R_2^S &= k_y^{(0)}K_1^2\cosh\left(k_y^{(1)}d\right)\sinh\left(k_y^{(0)}a_1\right)+k_y^{(1)}K_0^2\sinh\left(k_y^{(1)}d\right)\cosh\left(k_y^{(0)}a_1\right) \end{aligned} \quad (2.38)$$

Below the longitudinal electric field, in case of asymmetric filling of plates, is presented. A structure with perfectly conducting plates, and only one of them covered with a layer of finite conductivity material is considered.

$$E_z = j\frac{qk_z}{16\pi^2\varepsilon_0}\left\{A_{1_z}e^{-k_xa_1}+A_{2_z}e^{k_xa_1}\right\} = j\frac{qk_zA_0}{8\pi^2\varepsilon_0}Ch(2k_xa_1)$$
$$A_{1,2_z} = -A_0Sh\{k_x(a_1+\Delta)\}e^{\mp k_xa_1} \quad (2.39)$$

with

$$A_0 = k_x\left(k_y^{(1)^2}-k_x^2\right)Sh\left(2dk_y^{(1)}\right)\left\{\left(k_xCh(2a_1k_x)Sh\left(dk_y^{(1)}\right)+k_y^{(1)}Sh(2a_1k_x)Ch\left(dk_y^{(1)}\right)\right)\right.$$
$$\left.\left(k_y^{(1)}k_z^2Ch(2a_1k_x)Sh\left(dk_y^{(1)}\right)-k_xK_1^2Sh(2a_1k_x)Ch\left(dk_y^{(1)}\right)\right)\right\} \quad (2.40)$$

2.4 Impedance of two-layer symmetrical flat structure

As it is mentioned in the first chapter, the longitudinal impedance is a Fourier transformation of normalized longitudinal component of Lorentz force. The general expression of Lorentz force is:

$$\boldsymbol{F}(x,y,z) = q[\boldsymbol{E}(x,y,z)+\boldsymbol{v}\times\boldsymbol{B}(x,y,z)] \quad (2.41)$$

The longitudinal (z direction) impedance $Z_{\parallel}(x, y, k_z)$ is a Fourier transformation of normalized longitudinal component of Lorenz force $F_z(k_x, y, k_z)$. In the case, when a charge q is traveling along z axis, the longitudinal component of Lorentz force becomes

$$F_z(k_x, y, k_z) = qE_z(k_x, y, k_z) \tag{2.42}$$

and consequently the longitudinal impedance becomes

$$Z_{\parallel}(x, y, k_z) = -\frac{1}{qc}\int_{-\infty}^{\infty} E_z(k_x, y, k_z)e^{-ik_x x}dk_x \tag{2.43}$$

Consider the most important and at the same time a quite simple special case: symmetrical two-layer flat structure. In the case of the perfectly conductive outer layer $\left(k_y^{(2)} \to \infty\right)$ and the particle velocity equal to the velocity of light $\left(k_y^{(0)} = k_x,\ v = c\right)$, the formulae Eq. 2.37 is simplified to the form

$$A_{1C_{(S)}} = j\frac{qk_z k_y^{(1)}}{16\pi^2\varepsilon_0}\frac{\left(k_x^2 - {k_y^{(1)}}^2\right)\sinh\left(2k_y^{(1)}d\right)}{R_1^{C(S)}R_2^{C(S)}} \tag{2.44}$$

where

$$\begin{aligned} \begin{Bmatrix} R_1^C \\ R_2^C \end{Bmatrix} &= \begin{Bmatrix} k_y^{(1)} \\ k_x K_1^2 \end{Bmatrix} Ch\left(k_y^{(1)}d\right)Ch(k_x a_1) \pm \begin{Bmatrix} k_x \\ k_y^{(1)}k_x^2 \end{Bmatrix} Sh\left(k_y^{(1)}d\right)Sh(k_x a_1) \\ \begin{Bmatrix} R_1^S \\ R_2^S \end{Bmatrix} &= \begin{Bmatrix} k_y^{(1)} \\ k_x K_1^2 \end{Bmatrix} Ch\left(k_y^{(1)}d\right)Sh(k_x a_1) \pm \begin{Bmatrix} k_x \\ k_y^{(1)}k_x^2 \end{Bmatrix} Sh\left(k_y^{(1)}d\right)Ch(k_x a_1) \end{aligned} \tag{2.45}$$

This case fairly well simulates the highly conducting outer wall and is a two-dimensional analogue of a two-layer cylindrical tube, the unique resonant properties were discovered earlier. In the cylindrical waveguide, with two-layer metal walls under high conductivity of the thick outer wall and the relatively low conductivity of the thin inner layer, the radiation of the driving particles has a narrow-band resonance. Resonance is the sole and formed by single slowly propagating waveguide mode. We show that the same is true also of the two-dimensional two-layer metal structure.

In the cylindrical case, the resonance frequency is equal to $k_{z,rez} = \sqrt{2/a_1 d}$ (a_1 waveguide inner radius, d inner layer thickness). Minimum damping (in case of a perfect

conductor outer layer) is provided by the condition $\zeta = \frac{1}{\sqrt{3}} Z_0 \sigma_1 d$ ($Z_0 = 120\pi\ \Omega$, σ_1-inner layer conductivity).

First of all, let us demonstrate the single narrow-band extremal nature of the longitudinal impedance of the two-dimensional two-layer structure.

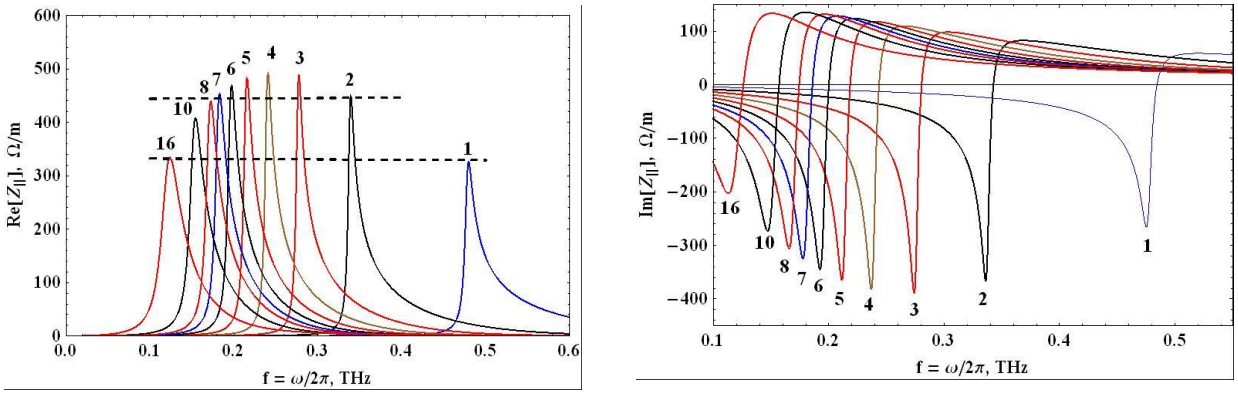

Figure 2.3: Real (left) and imaginary (right) parts of the longitudinal impedance of two-layer flat structure. On the graphs the thicknesses of the inner layer in micrometers are shown.

Figure 2.3 shows a series of real and imaginary component distributions for the longitudinal impedance of a two-layer planar structure with a perfectly conducting outer layer (Figure 4). The distance between the plates is $2\ cm$ (half-height $a_1 = 1\ cm$) and the conductivity of the inner layer is $2 \times\ 10^3\ \Omega^{-1} m^{-1}$ The numbers on the curves in the graph indicate the thickness of the inner layer (μm): "1" ($1 \mu m$), "2" ($2 \mu m$) and so on. As we see, the longitudinal impedance has a single narrow-band resonance with a resonance frequency dependent on the thickness of the inner layer. As is shown in Table 2.1, it is quite well defined by the formula

$$f_{rez} = \frac{c}{2\pi} \sqrt{\frac{1}{a_1 d}} \tag{2.46}$$

where $a_1 = a/2$ is a half-height of a structure.

$d\ (\mu m)$	1	2	3	4	5	6	7	8	10	16
$f_{rez}\ (THz)$	0.477	0.338	0.276	0.239	0.214	0.195	0.180	0.169	0.151	0.119
$f_{max}\ (THz)$	0.479	0.339	0.277	0.241	0.215	0.197	0.183	0.171	0.154	0.124
$f_0\ (THz)$	0.479	0.503	0.277	0.241	0.215	0.197	0.183	0.171	0.154	0.124
ς_i	0.251	0.339	0.754	1.001	1.257	1.508	1.760	2.011	2.513	4.021

Table 2.1: Resonance frequencies of two-layer flat structure, calculated analytically (f_{rez}), numerically (f_{max}), impedance imaginary component vanishing frequency (f_0) and a parameter ς_i.

In Table 2.1: line f_{rez} shows the resonance frequency calculated by Eq. 2.46; in line f_{max} the resonance frequencies calculated numerically by the exact formulae are given; line f_0 shows the frequency values in which the imaginary components of the impedance vanish; in the last row the values of the parameter $\varsigma_i = \frac{1}{3} Z_0 \sigma_1 d_i$ are given. As the table shows, there is a good coincidence between the frequency values f_{rez} and f_{max}. Thus, the resonant frequency in a flat two-layer metal structure, in contrast to the corresponding cylindrical structure, is defined by Eq. 2.46. In cylindrical case $f_{rez} = \frac{c}{2\pi}\sqrt{\frac{2}{a_1 d}}$., i.e. $\sqrt{2}$ times higher. There is also a complete coincidence of frequencies f_{max} and f_0, i.e. the maximum value of the impedance is purely real. Comparing the maximum values of the real component of impedance distributions (Figure 2.3, left) with the corresponding parameter ς_i values, we note the following regularities: impedance reaches the highest value at $d = 4\ \mu m$, which corresponds to value of parameter ς_i equal to unity. The maximum values of the other curves (Figure 2.3, left) on either side of it, decrease along with the distance.

As it is shown in Figure 2.3 (left), there is a pair of curves, maximum values of which are located on the same level. These curves correspond to a pair of mutually ς_i parameter reverse values. Thus, as it follows from Figure 2.3 and Table 2.1: $\varsigma_1 \approx 1/\varsigma_{16}$ and $\varsigma_2 \approx 1/\varsigma_8$. Similar phenomena occur also in a two-layer cylindrical waveguide. The difference is in the value of the parameter ς_i: $\varsigma = \frac{1}{3} Z_0 \sigma_1 d$ for planar and $\varsigma = \frac{1}{\sqrt{3}} Z_0 \sigma_1 d$ for cylindrical cases, i.e. $\sqrt{3}$ times less. Recall that the resonance frequencies in the planar case are $\sqrt{2}$ times less than in the corresponding cylindrical: $\omega_{rez} = c\sqrt{1/a_1 d}$ (a_1 inner half height of planar structure) instead of $\omega_{rez} = c\sqrt{2/a_1 d}$ (a_1 inner radius of cylinder). Such

relations for broadband resonance frequencies have been identified in [93] for the single-layer resistive two-dimensional flat and cylindrical structures (Figure 2.4). For comparison, Figure 2.4 shows the longitudinal impedance distributions for a two-layer metal tube with an ideally conducting outer layer. Its geometric and electromagnetic parameters are brought into correspondence with the parameters of the flat two-layer metal structure considered above. The internal radius of the cylinder $r_0 = 1\ cm$, the conductivity of the inner layer is $\sigma = 2 \times 10^3\ \Omega^{-1} m^{-1}$, and its thickness varies between $1\ \mu m$ and $5\ \mu m$.

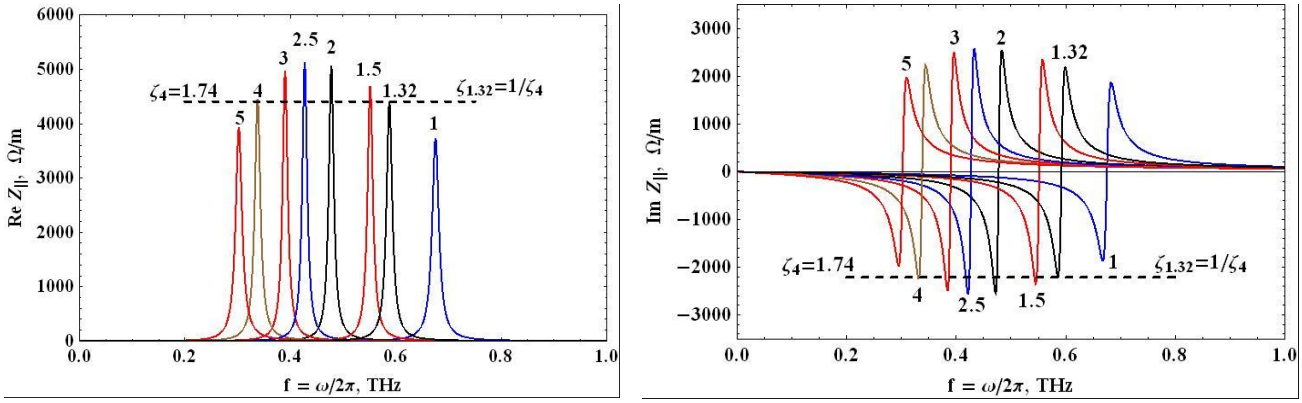

Figure 2.4: Real (left) and imaginary (right) parts of the longitudinal impedance of two-layer cylindrical structure. On the graphs, the thicknesses of the inner layer in microns are shown.

The wake potential is defined as the inverse Fourier transform of impedance (2.43)

$$W_{\|}(x, y, s) = \int_{-\infty}^{\infty} Z_{\|}(x, y, k)\, e^{-jks} ds, \quad s = z - vt \tag{2.47}$$

Figure 2.5 shows the distribution of the longitudinal wake potential for three different thicknesses of the inner layer at the fixed conductivity. In all three cases the wake potentials are quasi-periodic functions with the period Δs given by the resonant frequency $\Delta s = c/f_{rez}$, $f_{rez} = \frac{c}{2\pi}\sqrt{1/a_1 d}$. The latter indicates the particle radiation monochromaticity similar to two-layer cylindrical metal waveguide [74].

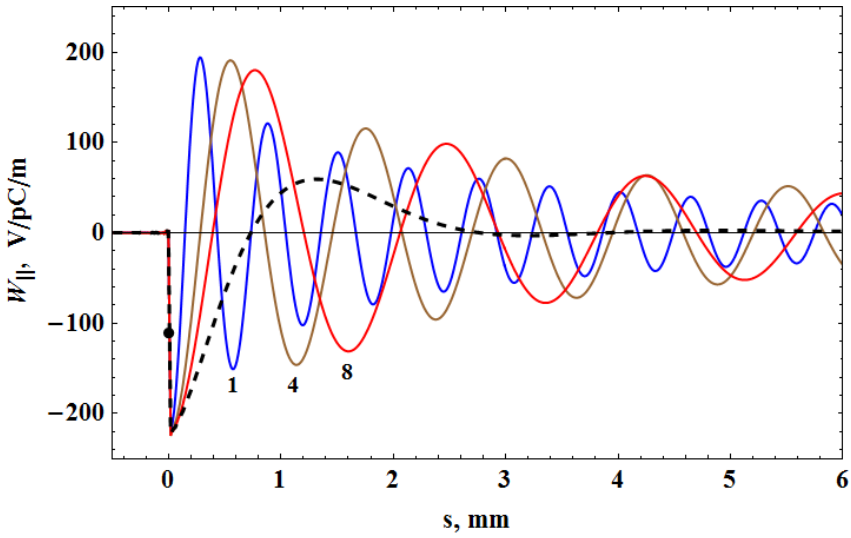

Figure 2.5: Longitudinal wake potential of the two-layer flat structure for different values of inner layer thickness and the fixed conductivity $\sigma = 2 \times 10^3\ \Omega^{-1}m^{-1}$; half-height of structure $a_1 = 1\ cm$. For comparison, the wake function for two unbounded infinite single-layer plates with halt-width $a_1 = 1\ cm$ and $\sigma = 2 \times 10^3\ \Omega^{-1}m^{-1}$ is given (dashed curve).

Figure 2.6 shows the wake potential distributions for a two-layer cylindrical structure.

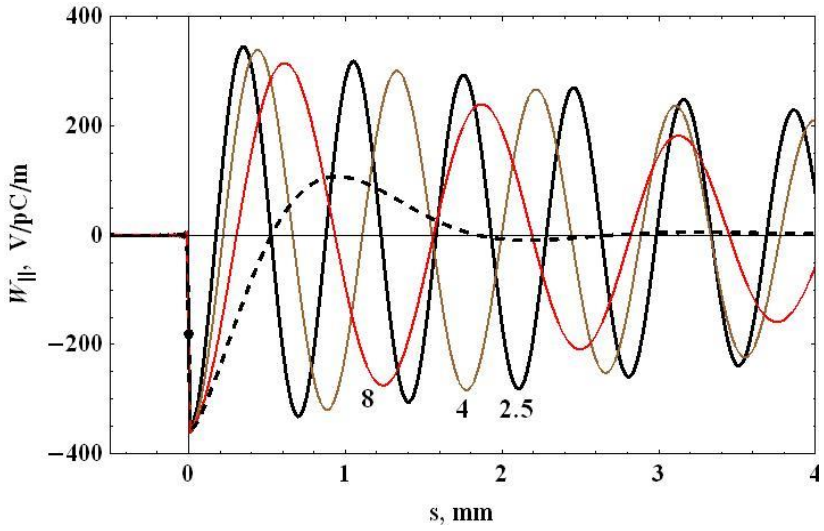

Figure 2.6: Longitudinal wake potential of the two-layer cylindrical waveguide for different values of inner layer thickness and the fixed conductivity $\sigma = 2 \times 10^3\ \Omega^{-1}m^{-1}$; inner radius of cylinder is equal to half height of flat structure (Figure 2.5) $r_0 = a_1 = 1\ cm$. The designations of the curves correspond to the thicknesses of the inner coating in microns. The wake potential for unbounded single-layer resistive cylinder with radius $r_0 = 1\ cm$ and $\sigma = 2 \times 10^3\ \Omega^{-1}m^{-1}$ is given in addition (dashed curve).

As in the plane case, the wake function of a cylindrical structure is a quasi-monochromatic oscillating damped function with a single oscillation frequency $f_{rez} = \frac{c}{2\pi}\sqrt{2/a_1 d}$. The period of the oscillations is $\Delta s = c/f_{rez}$ ($\sqrt{2}$ times less than the one of the flat case).

Comparing the curves for impedances and wake potentials for a two-layer cylindrical structure, we notice from Figure 2.4 (curve with label “2.5”), that in the frequency representation the maximum quality factor (maximum amplitude) of the impedance is reached at the thickness of inner coating equal to $2.5\ \mu m$. In the space-time representation this correlates with the minimum attenuation of the wake (Figure 2.6, curve with label “2.5”). In the cylindrical case, the attenuation coefficient is proportional to the value of $\zeta = \xi + \xi^{-1}$, with $\xi = \frac{1}{\sqrt{3}} Z_0 d\sigma$ and attains its minimum value at $\xi = 1$ [74].

The above-mentioned patterns (Figure 2.3 and Figure 2.5) are revealed in case of a fixed value of the inner layer conductivity. The regularities of the structure with a fixed thickness of the inner layer are denoted in Figure 2.7. The Figure shows the distribution of amplitude values of the impedance curve at $d = 1\mu m$ and $1500\ \Omega^{-1}m^{-1} < \sigma < 11000\ \Omega^{-1}m^{-1}$, which corresponds to the range of variation of $\xi = \frac{1}{\sqrt{3}} d\sigma Z_0$ parameter within $0.3 < \xi < 2.5$.

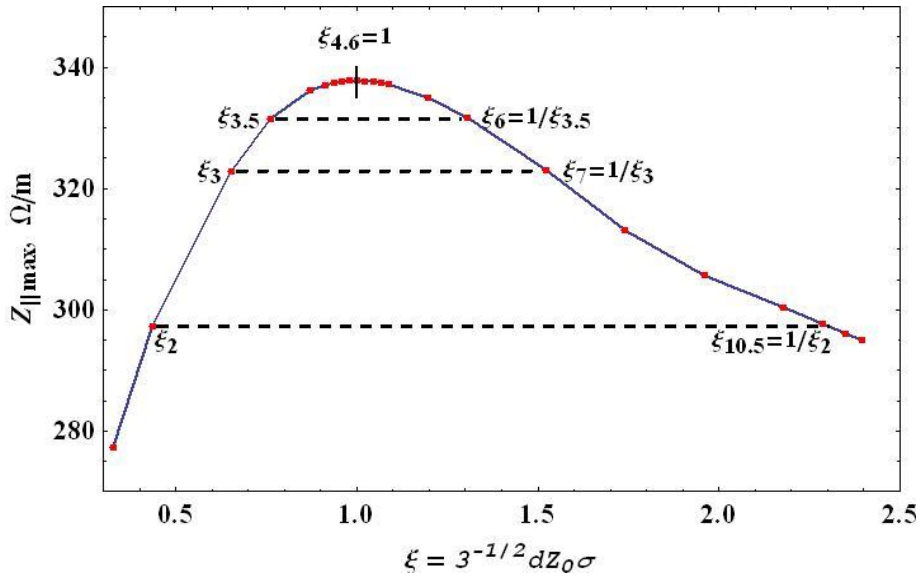

Figure 2.7: Distribution of resonance values of the two-layer flat structure impedance as a function of the inner layer conductivity σ for fixed geometric parameters($a_1 = 1cm,\ d = 1\ \mu m$). The horizontal dashed lines indicate the mutually conjugated values of the conductivities σ_a and σ_b for which $\zeta_b = 1/\zeta_a$ with $\zeta_{a(b)} = 3^{-1/2} d Z_0 \sigma_{a(b)}$. The red dots indicate the maximum possible level of impedance for a given thickness of the inner layer $d = 1\ \mu m$.

A significant difference between the cylindrical and flat cases is that in the first case the optimal condition (for the maximum Q of the system) is the fulfillment of equality $\xi = \frac{1}{\sqrt{3}} Z_0 \sigma d = 1$. In the second case, when fixing the conductivity value of the inner layer σ, the condition for optimizing the structure is the equality $\xi = \frac{1}{3} Z_0 \sigma d = 1$, i.e. the optimum layer thickness in this case is determined through its conductivity σ by the expression $d = \frac{3}{Z_0 \sigma}$. On the other hand, the fixed thickness of the inner layer d leads to the optimization condition $\xi = \frac{1}{\sqrt{3}} Z_0 \sigma d = 1$ and to the optimal conductivity of the layer $\sigma = \frac{\sqrt{3}}{Z_0 d}$. Thus, for a given conductivity of the inner layer, in order to select the optimum thickness of the layer, it is necessary to use the relation $d = \frac{3}{Z_0 \sigma}$, and for a given layer thickness d, its optimal conductivity is determined by the expression $\sigma = \frac{\sqrt{3}}{Z_0 d}$.

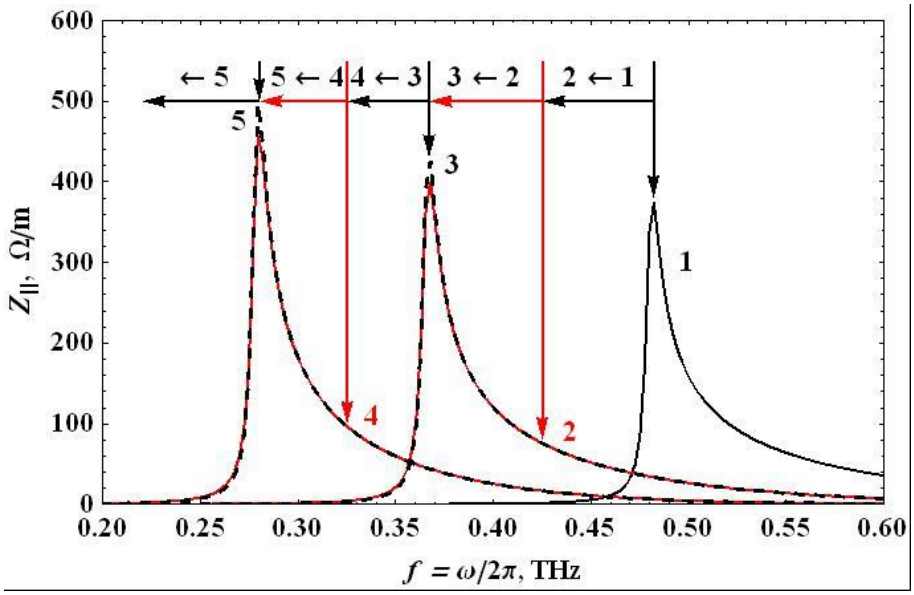

Figure 2.8: Parameter optimization of two-dimensional two-layer metal structure with an initial $d = 1\ \mu m$ thickness fixation of the inner layer.

Figure 2.8 shows the results of a sequential optimization process with the initial $d = 1\mu m$ thickness fixation of the inner layer. The figure shows 5 curves depicting the distribution of longitudinal impedances for the half-height of structure $a = 1\ cm$. Curve "1" (black solid curve) is plotted for the thickness of the inner layer $d = 1\ \mu m$ with a conductivity $\sigma = 4594\ \Omega^{-1}m^{-1}$, determined by the formula $\sigma = \frac{\sqrt{3}}{Z_0 d}$, i.e. curve "1" represents the impedance with the highest possible amplitude level, achievable at $d = 1\ \mu m$ by means of a corresponding selection of the inner layer conductivity. Afterwards, fixing the received value of conductivity, we determine the optimum value of layer thickness by the formula $d_2 = \frac{3}{Z_0 \sigma} = 1.732\ \mu m$, wich is optimal for this value of conductivity. As a result, we obtain curve 2 (red solid curve). Optimization leads to an increase in the thickness of the inner layer and, consequently, to a decrease in the resonant frequency. Further optimization again assumes the use of the formula $\sigma_2 = \frac{\sqrt{3}}{Z_0 d}$. As a result, we have curve "3" with a reduced conductivity $\sigma_3 = 2653\ \Omega^{-1}m^{-1}$ and a resonance conserved frequency. This procedure, consisting of the successive application of formulas $d_i = \frac{3}{Z_0 \sigma_i}$ and $\sigma_{i+1} = \frac{\sqrt{3}}{Z_0 d_i}$, can be repeated many times, successively increasing the thickness of the inner layer and its conductivity and decreasing the resonance frequency (Figure 2.8).

An alternative way to perform a series of optimizations is shown in Figure 2.9. It is obtained by firstly fixing the conductivity of the inner layer of the structure. In the figure curve “1” corresponds to the originally selected conductivity of the inner layer $\sigma = 2 \times 10^3\ \Omega^{-1}m^{-1}$. Its thickness is optimized using the formula $d = \frac{3}{Z_0\sigma} = 3.98\ \mu m$. Curve “2” (red, dashed) is obtained by optimizing the conductivity for the resulting length: $\sigma_2 = \frac{\sqrt{3}}{Z_0 d} = 1154\ \Omega^{-1}m^{-1}$. The resonant frequency does not change in this case. The further optimization step, corresponding to curve “3”, is carried out using the formula $d_2 = \frac{3}{Z_0\sigma_2} = 6.89\ \mu m$. This optimization stage is accompanied by an increase in the thickness of inner layer and by a decrease of resonant frequency. At the next stage, the optimum conductivity value is determined for the layer new thickness $\sigma_3 = \frac{\sqrt{3}}{Z_0 d_2} = 385\ \Omega^{-1}m^{-1}$ (curve “3”) and so on.

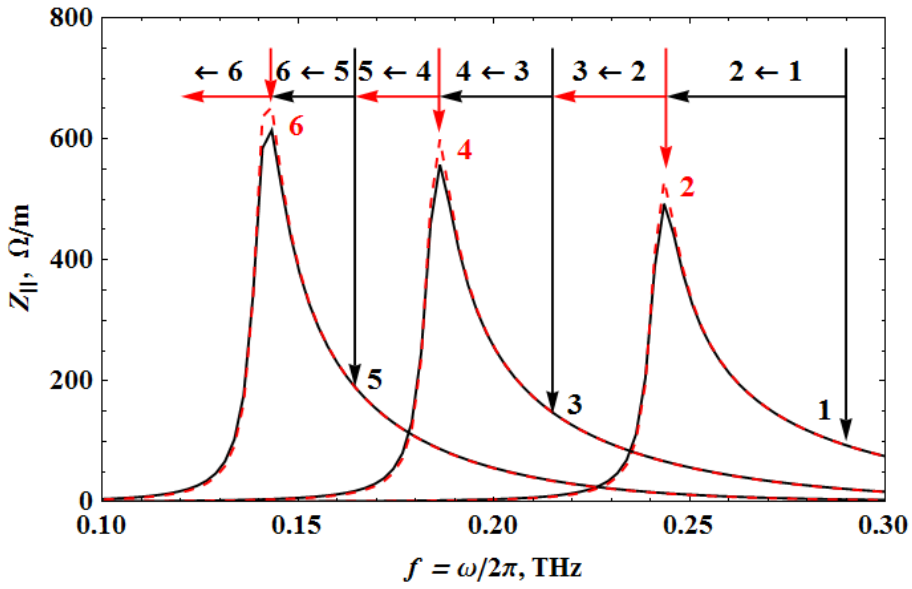

Figure 2.9: Optimization of the parameters of a two-dimensional two-layer metal structure with an initial fixation of the inner layer conductivity $\sigma = 2 \times 10^3\ \Omega^{-1}m^{-1}$.

Thus, there are two different possibilities to optimize a two-dimensional two-layer metal structure: the first (Figure 2.8) is accompanied by an increase of material conductivity of the inner layer, while the second (Figure 2.9) lowers it.

The practical significance of the above study is the ability to correctly select the thickness of the inner layer and the electromagnetic characteristics of the material filling it.

This, for example, was successfully done when experimentally testing the resonant properties of a two-layer metal structure [90] with severe limitations on the measuring equipment, the frequency range of which was limited by 14 GHz bandwidth.

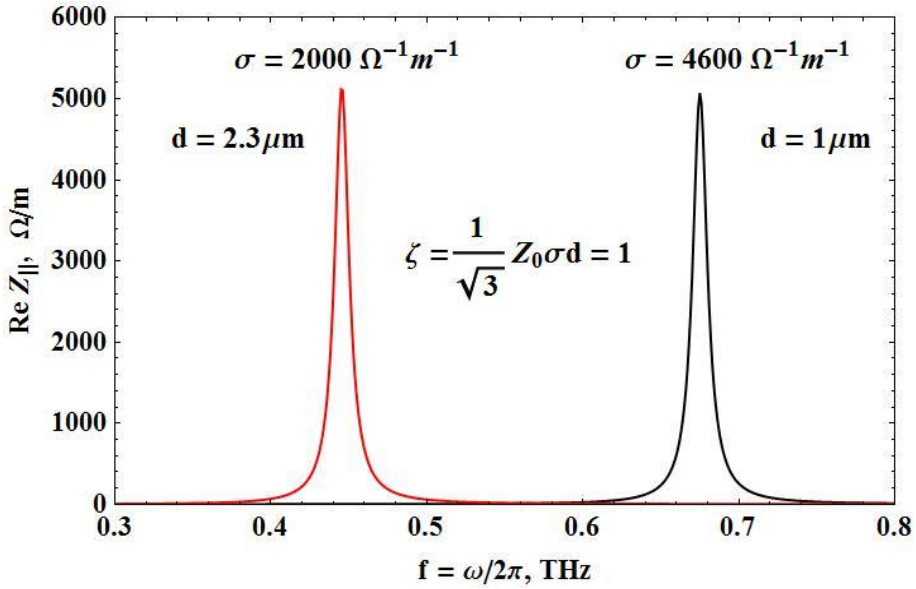

Figure: 2.10: Longitudinal impedance of cylindrical pipe with optimized parameters: optimal inner layer width $d = 2.3\ \mu m$ for given conductivity $\sigma = 2000\ \Omega^{-1}m^{-1}$ (left one); optimal inner layer conductivity $\sigma = 4600\ \Omega^{-1}m^{-1}$ for given layer width $d = 1\ \mu m$ (right one).

In the case of a two-layer cylindrical structure, the picture is much simpler. In this case, the character of narrow-band resonance of the impedance curve is completely due to the unity proximity of parameter $\xi = \frac{1}{\sqrt{3}} Z_0 \sigma d$ [66]. The impedance curve is completely determined by setting two parameters (ξ, σ; ξ, d or σ, d) out of three (ξ, σ, d).

2.5 Approximate analytical representation of impedance

The integral representation of the longitudinal impedance (Eq. 2.43 – Eq. 2.45) is accurate (exact) and, as was shown above, it is possible to calculate both the impedance and the wake potential (represented in the form of a double integral (Eq. 2.47)). For calculation, a corresponding software package has been developed by using the software package Mathematica. The integral form of the expressions for the impedance and the wake function, as well as the complexity of the integrand leads, however, to some difficulties in interpreting them. Integration by means of its contour deformation and its transfer to the complex plane is associated by taking into account (in addition to complex

poles of denominator) also the integration along the cuts on Riemann surface. The latter circumstance is connected with the non-analyticity of the function $k_y^{(1)} = \sqrt{k_x^2 + (1 - \varepsilon^{(1)}\mu^{(1)}c^2)k^2}$, which leads to the non-analyticity of the denominator of the integrand as a whole.

The analysis of the integrand in (Eq. 2.43) is performed taking into account the smallness of parameter d ($d \ll a_1$), characterizing the thickness of the inner layer. For this purpose, we rewrite the function A_{1C} (Eq. 2.44) in the form

$$A_{1C} = \frac{qZ_0k_x}{8\pi^2}\frac{Z_0\sigma k}{\tilde{R}}, \quad \tilde{R} = \tilde{R}_1^C\tilde{R}_2^C \tag{2.48}$$

where

$$\begin{gathered}\tilde{R}_1^C = k_y^{(1)}Ch(k_xa_1)Cth\left(k_y^{(1)}d\right) + k_xSh(k_xa_1) \\ \tilde{R}_2^C = k_x(k + j\,Z_0\sigma)Ch(k_xa_1) + kk_y^{(1)}Sh(k_xa_1)Th\left(k_y^{(1)}d\right)\end{gathered} \tag{2.49}$$

After multiplication, the denominator in Eq. 2.48 takes the form

$$\begin{gathered}\tilde{R} = k_y^{(1)}k_x(k + j\,Z_0\sigma)Ch^2(k_xa_1)Cth\left(k_y^{(1)}d\right) + \\ \frac{1}{2}\left(k_y^{(1)^2}k + k_x^2(k + j\,Z_0\sigma)\right)Sh(2k_xa_1) + k_y^{(1)}k_xkSh^2(k_xa_1)Th\left(k_y^{(1)}d\right)\end{gathered} \tag{2.50}$$

Further, we expand $\tilde{R}$ in series with respect to the small parameter d and leave the first three terms of the expansion (d^{-1}, d^0 and d). As a result, we get

$$\tilde{R} \approx u_{-1}/d + u_0 + u_1d \tag{2.51}$$

where

$$\begin{gathered}u_1 = \frac{1}{3}k_y^{(1)^2}k_x\left((k + j\,Z_0\sigma)Ch^2(k_xa_1) + 3kSh^2(k_xa_1)\right) \\ u_0 = \frac{1}{2}\left(k_y^{(1)^2}k + k_x^2(k + j\,Z_0\sigma)\right)Sh(2k_xa_1) \\ u_{-1} = k_x(k + j\,Z_0\sigma)Ch^2(k_xa_1)\end{gathered} \tag{2.52}$$

Expression 2.51, with taking into account Eq. 2.52, no longer contains square roots of the integration variables and is analytical.

Further, supposing $k_x^2 \ll Z_0 \sigma k$, (in the cylindrical case this approximation is equivalent to the one for the permittivity of the metal $\varepsilon \approx j\,\sigma/\omega$, which is valid for not very large frequencies) we have:

$$k_y^{(1)^2} \approx -jZ_0\sigma k \tag{2.53}$$

and instead of Eq. 2.52, we can write

$$\begin{aligned} u_1 &= -\frac{1}{3} jZ_0\sigma k k_x \left((k + j\,Z_0\sigma) Ch^2(k_x a_1) + 3kSh^2(k_x a_1)\right) \\ u_0 &= \frac{1}{2}\left(kk_x^2 + j\,Z_0\sigma(k_x^2 - k^2)\right) Sh(2k_x a_1) \\ u_{-1} &= k_x(k + j\,Z_0\sigma) Ch^2(k_x a_1) \end{aligned} \tag{2.54}$$

Figures (2.11–2.15) show the comparison of calculations of exact formulae with the approximated ones (Eq. 2.51 – Eq. 2.54) for three different half-widths of a plane structure: $a_1 = 10\ cm$ (Figure 2.11 and Figure 2.12), $a_1 = 1\ cm$ (Figure 2.13 and Figure 2.14) and $a_1 = 1\ mm$ (Figure 2.15). The thickness of the inner layer is chosen equal to $7\ \mu m$. Dashed red curves represent the results obtained from exact formulae. The approximate results are represented by solid black curves.

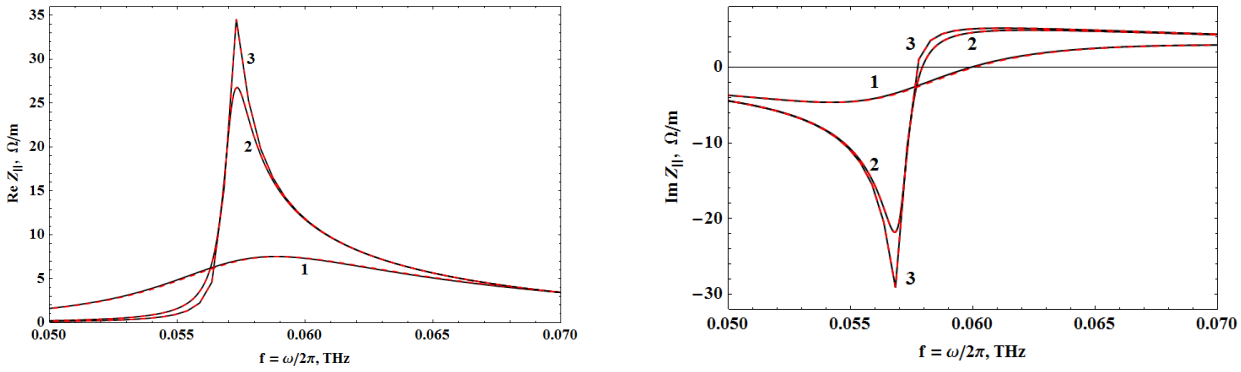

Fig. 2.11: Real (left) and imaginary (right) components of the longitudinal impedance of a two-layer metal structure, calculated by exact formulae (red, dashed) and using the approximation (2.48, 2.51) (black, solid): 1 - $\sigma = 2 \times 10^4\ \Omega^{-1}m^{-1},\ \zeta = 30.5$; 2 - $\sigma = 2 \times 10^3\ \Omega^{-1}m^{-1},\ \zeta = 3.05$; 3 - $\sigma = 656\ \Omega^{-1}m^{-1},\ \zeta = 1$; $a_1 = 10\ cm,\ d = 7\ \mu m$.

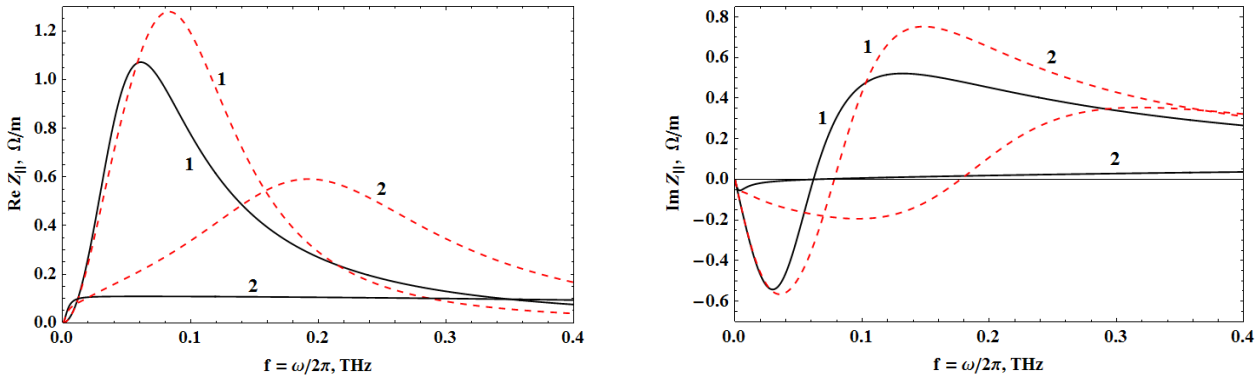

Fig. 2.12. Real (left) and imaginary (right) components of the longitudinal impedance of a two-layer metal structure, calculated by exact formulae (dashed) and using the approximation (2.48, 2.51) (black, solid): 1 - $\sigma = 2 \times 10^5\ \Omega^{-1}m^{-1},\ \zeta = 135$; 2 - $\sigma = 2 \times 10^6\ \Omega^{-1}m^{-1},\ \zeta = 1523$; $a_1 = 10\ cm,\ d = 7\ \mu m$.

As can be seen from Figure 2.11 and Figure 2.13, for relatively large values of the half-widths of the structure ($1\ cm \le a_1 \le 10\ cm$) there is a complete coincidence of the approximation calculations with the exact ones even for much larger (in comparison with unity) values of the parameter $\zeta = \frac{1}{\sqrt{3}} Z_0 d$ (up to $\zeta \sim 30$). Significant discrepancies occur at large values of this parameter $\zeta \sim 100$ (Figure 2.12 and Figure 2.14).

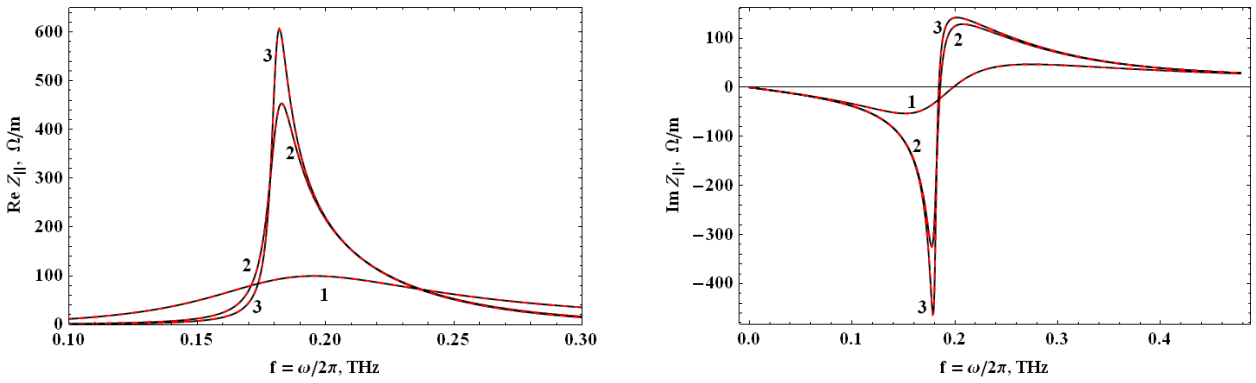

Fig. 2.13: Real (left) and imaginary (right) components of the longitudinal impedance of a two-layer metal structure, calculated by exact formulae (red, dashed) and using the approximation (2.48, 2.51) (black, solid): 1 - $\sigma = 2 \times 10^4\ \Omega^{-1}m^{-1},\ \zeta = 30.5$; 2 - $\sigma = 2 \times 10^3\ \Omega^{-1}m^{-1},\ \zeta = 3.05$; 3 - $\sigma = 656\ \Omega^{-1}m^{-1},\ \zeta = 1$; $a_1 = 1\ cm,\ d = 7\ \mu m$.

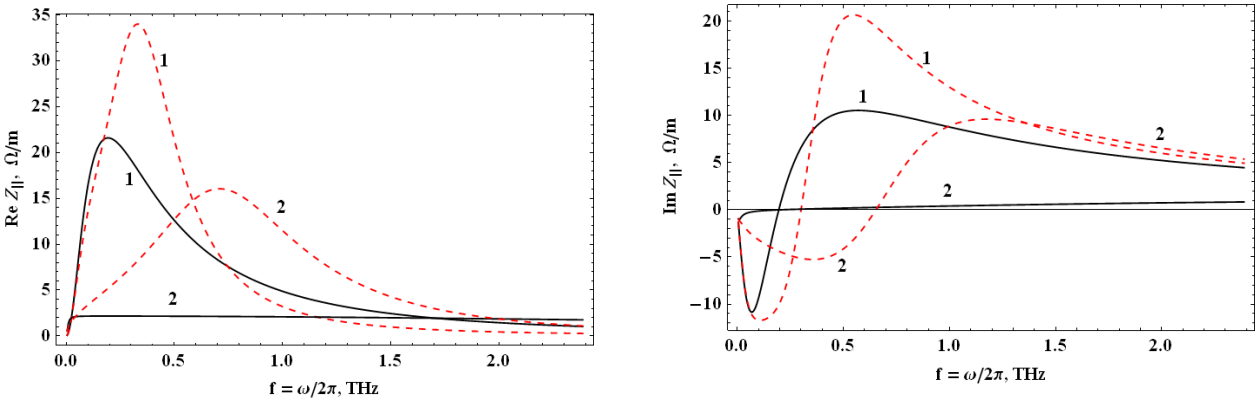

Fig. 2.14: Real (left) and imaginary (right) components of the longitudinal impedance of a two-layer metal structure, calculated by exact formulae (dashed) and using the approximation (2.48, 2.51) (black, solid): 1 - $\sigma = 2 \times 10^5\ \Omega^{-1}m^{-1},\ \zeta = 135;$ 2 - $\sigma = 2 \times 10^6\ \Omega^{-1}m^{-1},\ \zeta = 1523;$ $a_1 = 1\ cm,\ d = 7\ \mu m.$

As follows from Figure 2.15, a decrease in the gap between the plates leads to a toughening of requirement ζ to be close to unity. Thus, for $\zeta = 30$ (curve “1” on Figure 2.15) there is an essential discrepancy between the exact and approximate solutions, whereas for $\zeta = 7.6$ (curve “2” on Figure 2.15) they practically coincide.

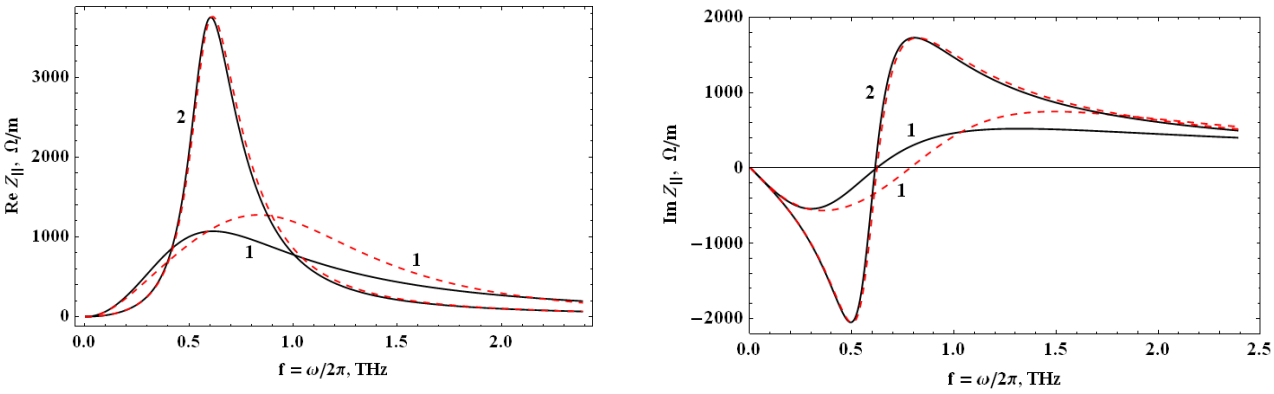

Fig. 2.15: Real (left) and imaginary (right) components of the longitudinal impedance of a two-layer metal structure, calculated by exact formulae (dashed) and using the approximation (2.48, 2.51) (black, solid): 1 - $\sigma = 2 \times 10^4\ \Omega^{-1}m^{-1},\ \zeta = 30.5;$ 2 - $\sigma = 5 \times 10^3\ \Omega^{-1}m^{-1},\ \zeta = 7.6;$ $a_1 = 1\ mm,\ d = 7\ \mu m.$

Further simplification of the integrand (Eq. 2.50 – Eq. 2.53) is achieved by replacing the hypergeometric functions by their decomposition. The expansions in a series of hypergeometric functions $Sh(x)$ and $Ch(x)$ have the following form [94]:

$$Sh(x) = \sum_{n=1}^{\infty} \frac{x^{2n-1}}{(2n-1)!}, \qquad Ch(x) = \sum_{n=1}^{\infty} \frac{(x)^{2n-2}}{(2n)!} \tag{2.55}$$

Inserting Eq. 2.55 into Eq. 2.54 and leaving the first N terms of the expansion in them, instead of Eq. 2.48 we have the following:

$$A_{1C} = \frac{qZ_0}{8\pi^2} \frac{Z_0 \sigma k}{\tilde{R}'} \tag{2.56}$$

where

$$\tilde{R}' \approx u'_{-1}/d + u'_0 + u'_1 d \tag{2.57}$$

and

$$\begin{gathered} u'_1 = \frac{1}{6} jk\sigma Z_0 \big((2k - i\sigma Z_0) - (4k + i\sigma Z_0) Ch_N(2a_1 k_x)\big) \\ u'_{-1} = \frac{1}{2}(k + j\, Z_0 \sigma)(1 + Ch_N(2a_1 k_x)) \\ u'_0 = \frac{1}{2}\big(kk_x^2 + j\, Z_0 \sigma (k_x^2 - k^2)\big) \frac{Sh_N(2k_x a_1)}{k_x} \end{gathered} \tag{2.58}$$

with

$$Sh_N(x) = \sum_{n=1}^{N} \frac{x^{2n-1}}{(2n-1)!}, \;\; Ch_N(x) = \sum_{n=1}^{N} \frac{x^{2n-2}}{(2n)!} \tag{2.59}$$

In this approximation, the denominator (Eq. 2.57) is represented in the form of an algebraic polynomial of 2N-th order in powers of k_x

$$\tilde{R}' = \sum_{n=0}^{2N} a_n k_x^n \tag{2.60}$$

and can be written in a form containing its complex roots $x_i, \; i = 1,2, \ldots 2N$

$$\tilde{R}' = a_{2N} \prod_{i=1}^{2N} (k_x - x_i) \tag{2.61}$$

Thus, Eq. 2.56 can be rewritten as follows:

$$A_C = \frac{qZ_0}{8\pi^2} \frac{Z_0 \sigma k}{a_{2N} \prod_{i=1}^{2N} (k_x - x_i)} \tag{2.62}$$

The longitudinal impedance, which is an integral of this expression over k_x, can explicitly be expressed in terms of the roots x_i of the equation $\tilde{R}'(k_x) = 0$

$$Z_{||} = \int_{-\infty}^{\infty} A_C dk_x = -\frac{Z_0^2 \sigma k}{4\pi^2 a_{2N}} \sum_{n=1}^{2N} \frac{ln\{-x_n\}}{\prod_{\substack{i=1 \\ i\neq n}}^{2N} (x_n - x_i)} \qquad (2.63)$$

The roots x_i of the equation $\tilde{R}'(k_x) = 0$ are determined numerically for an arbitrary value of N with the help of the software package Mathematica.

The longitudinal impedance of a two-layer metal structure calculated by exact and approximate formulas formulae is presented in Figure 2.16. In the figure, the black solid impedance curves are calculated using the approximate equations 2.51 and 2.53, the blue dashed ones are from Eq. 2.63 for $n = 5$ and the red dashed ones are for the impedances calculated by exact formula.

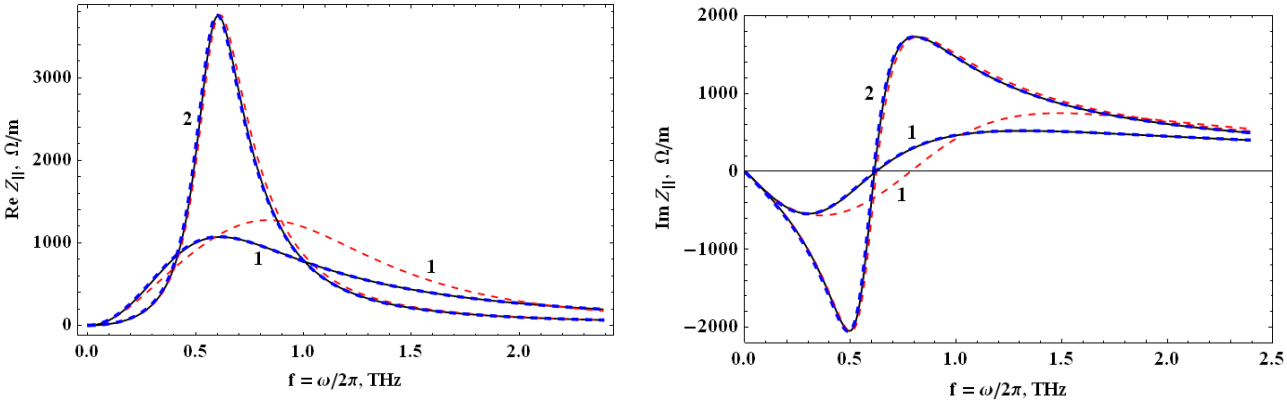

Fig. 2.16: Real (left) and imaginary (right) components of the longitudinal impedance of a two-layer metal structure, calculated by exact formulae (red, dashed), using the approximation (2.48, 2.51) (black, solid) and using approximation (2.60) for n=5 (blue, dashed): 1 - $\sigma = 2 \times 10^4\ \Omega^{-1}m^{-1}, \zeta = 30.5$; 2 - $\sigma = 5 \times 10^3\ \Omega^{-1}m^{-1}, \zeta = 7.6$; $a_1 = 1\ mm, d = 7\ \mu m$.

In Figure 2.16, the impedance curves calculated using the asymptotic (Eq. 2.62) are superimposed on the impedance curves shown in Fig. 2.15.

2.6 Summary

A method of calculating the longitudinal impedance of a multilayer two-dimensional flat structure is presented. The matrix formalism that allows to couple electromagnetic field components in the inner and outer regions of the structure has been developed. Non-ultrarelativistic particle radiation fields in the multilayer flat symmetric and asymmetric structure are obtained. Explicit expressions of the radiation fields in two-layer structure

with unbounded external walls and in single-layer unbounded structure are derived as a special case of fields in multilayer structure.

An ultrarelativistic particle radiation in a symmetrical two-layer flat structure with perfectly conducting outer layer is derived. Longitudinal impedance of this structure with low conductivity thin inner layer and high conductivity thick outer layer wall is numerically obtained. It is shown that the impedance has a narrow-band resonance. The resonance frequency dependence on structure parameters is obtained. Parameter $\varsigma_i = \frac{1}{3} Z_0 \sigma_1 d_i$ is introduced, which describes the maximum values of impedance. It is shown that impedances of structures with reverse ς parameters ($\varsigma_i * \varsigma_j = 1$) have the same maximum values and reach their highest maximum when ς_j are equal to unity.

Chapter 3: Rectangular resonator with two-layer vertical walls

3.1 Introduction

In this chapter, dispersion relations are obtained for the electromagnetic eigen-oscillations in a rectangular resonator with ideally conducting walls. The horizontal (top and bottom) walls of this resonator are covered from inside by a thin low-conductive layer. In the second chapter it is shown that double-layer parallel plates for appropriate parameters have a distinct, narrow band resonance. In this chapter rectangular copper cavity with two-layer horizontal walls is observed. Here, unlike the parallel plates, one has a discrete set of wavenumbers in all three degrees of freedom. Compared with two-dimensional structure, the pattern of modal frequency distribution in such a resonator is distorted: in addition to the fundamental resonance frequency, a set of secondary resonances, caused by side walls, exists. It is important to note the presence of the fundamental resonance, fixed by measurements, and caused by the two-layer horizontal cavity walls. To be able to distinguish the main mode from secondary resonances, finite wall resonator model is developed and resonance frequencies of the resonator are calculated.

In this chapter secondary resonances caused by side walls are obtained. The criterions for the choice of resonator materials are interpreted and resonance frequencies are predicted via the resonator model with ideal conducting walls. The choice is conditioned by the frequency bandwidth of the experimental set-up ($14\,GHz$) and the predicted single resonance for two parallel laminated plates (chapter 2). The electro-dynamical properties of test resonator model (perfectly conducting rectangular cavity with inner low conducting layers) are studied. Resonance frequencies of the test structure are experimentally measured and a comparison with the predicted resonant frequencies of resonator model and two parallel double-layer plates is done. A good agreement between these results is obtained.

The experimentally obtained resonance frequencies are subjected to the laws specific to this kind of structures: their value decreases with the increasing height of the cavity. At the same time, the difference between the measured and calculated values

increases. By decreasing a structure height, the contribution of its sidewalls also decreases, that is why for a structure with small height there is a good agreement between experimental and theoretical resonant frequencies.

3.2 IHLCC cavity with ideally conductive walls

To analytically obtain dispersion relations for a tested cavity, a simplified resonator model is studied. It is assumed that all four sidewalls of internal horizontal low conductive coatings (IHLCC) cavity are ideally conductive materials, and the upper and lower ideally conductive walls are covered by a thin layer of low-conductive material (Fig 3.1).

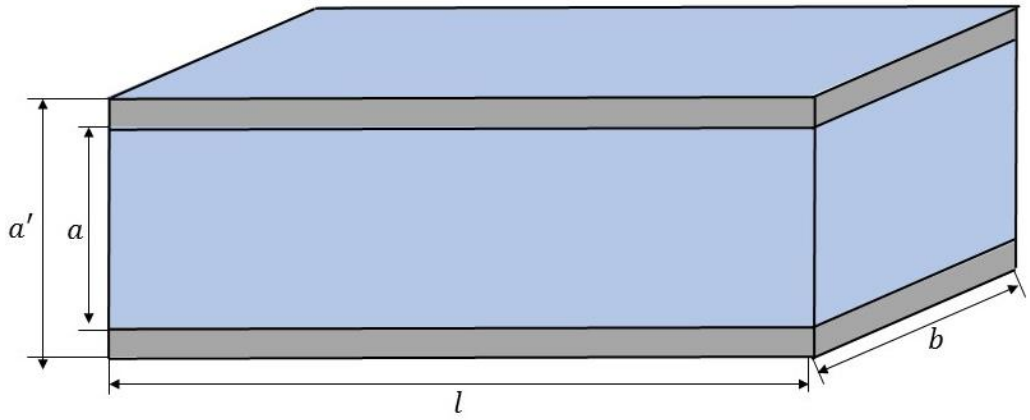

Figure 3.1: IHLCC cavity shape.

This model is very close to the cavity with copper walls, so it is expected that the analytical results would be in a good agreement with the ones of tested cavity. Exact dispersion equations may be obtained for a similar structure by the method of partial areas. In this case, three regions may be distinguished:

1. $0 \le x \le b,\ 0 \le z \le l$ top low conductivity material plate
2. $0 \le x \le b,\ 0 \le z \le l$ vacuum chamber of cavity (3.1)
3. $0 \le x \le b,\ 0 \le z \le l$ bottom low conductivity material plate

Electric and magnetic fields of cavity in each of the three regions are sought in the following form:

$$\vec{E}_i = \vec{E}_i^{(1)} + \vec{E}_i^{(2)}, \vec{B}_i = (jkc)^{-1} rot\vec{E}_i, \qquad i = 1,2,3 \tag{3.2}$$

with

$$\left.\begin{matrix} E_{x,i}^{(1)} \\ E_{x,i}^{(2)} \end{matrix}\right\} = \left\{\begin{matrix} A_{x,i}^{(1)} Ch(Q_i y) \\ A_{x,i}^{(2)} Sh(Q_i y) \end{matrix}\right\} Cos(k_x x) Sin(k_z z)$$
$$\left.\begin{matrix} E_{y,i}^{(1)} \\ E_{y,i}^{(2)} \end{matrix}\right\} = \left\{\begin{matrix} A_{y,i}^{(1)} Sh(Q_i y) \\ A_{y,i}^{(2)} Ch(Q_i y) \end{matrix}\right\} Sin(k_x x) Sin(k_z z) \quad (3.3)$$
$$\left.\begin{matrix} E_{z,i}^{(1)} \\ E_{z,i}^{(2)} \end{matrix}\right\} = \left\{\begin{matrix} A_{z,i}^{(1)} Ch(Q_i y) \\ A_{z,i}^{(2)} Sh(Q_i y) \end{matrix}\right\} Sin(k_x x) Cos(k_z z)$$

where $A_{x,y,z,i}^{(1,2)}$ are arbitrary amplitudes, $Q_{1,3} = K, Q_2 = k_y$ and

$$K = \sqrt{k^2(1 - \varepsilon'\mu') + k_y^2}, \qquad k = \frac{\omega}{c} = \sqrt{k_x^2 + k_z^2 - k_y^2}, \quad (3.4)$$

The boundary conditions on the perfectly conducting sidewalls are

$$\begin{matrix} E_{x,i} = E_{y,i} = 0 \\ E_{y,i} = E_{z,i} = 0 \end{matrix} \quad \text{at} \begin{matrix} z = 0,\ z = l \\ x = 0,\ x = b \end{matrix}, \quad i = 1,2,3 \quad (3.5)$$

To satisfy these conditions, horizontal wavenumbers should be in the form of $k_x = (m-1)\frac{\pi}{b}$, $k_z = (n-1)\frac{\pi}{l}$, $m, n = 1,2,3 \ldots$. k_y , transverse vertical wavenumbers should be determined from boundary conditions on low-conductive layer surfaces and vertical walls.

On vacuum-low conductive layer borders, from the continuity of tangential electric and magnetic field components, we have:

$$\begin{matrix} E_{x,1} = E_{x,2},\ E_{z,1} = E_{z,2} \\ B_{x,1} = B_{x,2},\ B_{z,1} = B_{z,2} \end{matrix} \quad \text{at } y = a/2 \quad (3.6)$$

$$\begin{matrix} E_{x,2} = E_{x,3},\ E_{z,2} = E_{z,3} \\ B_{x,2} = B_{x,3},\ B_{z,2} = B_{z,3} \end{matrix} \quad \text{at } y = -a/2 \quad (3.7)$$

On the outer boundaries, between low conductive layers and ideal conductors, electrical tangential components of fields must vanish:

$$\begin{matrix} E_{x,1} = 0,\ E_{z,1} = 0 \\ E_{x,3} = 0,\ E_{z,3} = 0 \end{matrix} \quad \text{at} \begin{matrix} y = a'/2 \\ y = -a'/2 \end{matrix} \quad (3.8)$$

Using Maxwell's equation $div\vec{E}_i^{(1,2)} = 0$, the amplitudes $A_{z,i}^{(1,2)}$ can be expressed by $A_{x,i}^{(1,2)}$ and $A_{y,i}^{(1,2)}$. Thus, we have a linear homogeneous system consisting of 12 equations (Eq. 3.6 - Eq. 3.8) and containing the same number of indeterminate coefficients: $A_{x,i}^{(1,2)}$, $A_{y,i}^{(1,2)}$ with $i = 1,2,3$. The condition for the existence of non-trivial solutions of this system is the vanishing of its determinant:

$$D = P_1 P_2 P_3 P_4 = 0 \tag{3.9}$$

where

$$P_1 = K_{nm} Ch(dK) Sh(ak_{yf}) + k_{yf} Sh(dK_{nm}) Ch(ak_{yf}) \tag{3.10.a}$$

$$P_2 = K_{nm} Ch(dK_{nm}) Ch(a_1 k_{yf}) + k_{yf} Sh(dK_{nm}) Sh(a_1 k_{yf}) \tag{3.10.b}$$

$$P_3 = -K_{nm} k^2 Sh(dK_{nm}) Ch(ak_{yf}) - k_{yf} k^2 \varepsilon' \mu' Ch(dK_{nm}) Sh(ak_{yf}) \tag{3.10.c}$$

$$P_4 = -k_{yf} k^2 \varepsilon' \mu' Ch(dK_{nm}) Ch(ak_{yf}) - K_{nm} k^2 Sh(dK_{nm}) Sh(ak_{yf}) \tag{3.10.d}$$

where $K_{nm} = \sqrt{k_{xn}^2 + k_{zm}^2 - k^2 \varepsilon' \mu'}$, $k = \frac{\omega}{c} = \sqrt{k_{xn}^2 + k_{zm}^2 - k_{yf}^2}$, $n, m, f = 1,2,3, \ldots$.

As a result we have four independent dispersion equations:

$$P_i = 0, i = 1,2,3,4 \tag{3.11}$$

Each of these four equations includes three eigenvalues: k_{xn}, k_{zm} and k_{yf}. Moreover, the horizontal transverse k_{xn} and longitudinal k_{zm} wave numbers are fixed for given numbers n and m. They form two infinite sequences generated by integer indices m and n. Thus, each of equations (Eq. 3.10.a -3.10d) defines the sequence of $k_{yf}, (f = 1,2,3, \ldots)$ values for each fixed combination of indices m and n. From these equations we get sequences of eigenvalues $k_y = k_{mnf}^{(i)}$ $(i = 1,2,3,4)$ for $= 1,2,3$ ..., which are dependent on m and n.

Let us compare the obtained expressions with the corresponding ones, obtained for the two-layer flat structure in chapter 1 (1.24):

$$
\begin{aligned}
T_1 &= k_y^{(1)} Ch\left(dk_y^{(1)}\right) Sh\left(ak_y^{(0)}\right) + k_y^{(0)} Sh\left(dk_y^{(1)}\right) Ch\left(ak_y^{(0)}\right) \\
T_2 &= k_y^{(1)} Ch\left(dk_y^{(1)}\right) Ch\left(ak_y^{(0)}\right) + k_y^{(0)} Sh\left(dk_y^{(1)}\right) Sh\left(ak_y^{(0)}\right) \\
T_3 &= -k_y^{(0)} k^2 \varepsilon_i' \mu_i' Ch\left(dk_y^{(1)}\right) Sh\left(ak_y^{(0)}\right) - k_y^{(1)} k^2 Sh\left(dk_y^{(1)}\right) Ch\left(ak_y^{(0)}\right) \\
T_4 &= -k_y^{(0)} k^2 \varepsilon_i' \mu_i' Ch\left(dk_y^{(1)}\right) Ch\left(ak_y^{(0)}\right) - k_y^{(1)} k^2 Sh\left(dk_y^{(1)}\right) Sh\left(ak_y^{(0)}\right)
\end{aligned}
\tag{3.12}
$$

Obviously, there is a correspondence: $P_i \leftrightarrow T_i, i = 1,2,3,4$. A complete coincidence cannot take place, since in the case of an infinite two-dimensional structure, the variables k_x and k_z are integration variables, but in the case of a resonator, the wave numbers k_{xn} and k_{zm} are discrete and fixed for specified indexes n and m.

The standing wave excited in the resonator consists of the imposition of two traveling waves propagating in opposite directions: a wave incident on the front wall of the resonator $(\vec{E}_1)$ and reflected from it $(\vec{E}_2)$:

$$
E_{x,y,z} = E_{1,x,y,z} \pm E_{2,x,y,z},\ E_{1,2,x,y,z} = A_{1,2,x,y,z} e^{j(\pm k_z z - \omega t)} \tag{3.13}
$$

The wave $\vec{E}_1$ can serve as an analog of a wave propagating in an infinite planar two-layer structure, generated by a particle. Since its frequency ω in this case is complex, it can be represented in the form:

$$
\omega = c\sqrt{A + jB} = c\sqrt{\frac{\sqrt{A^2+B^2}+B}{2}} + jc\ Sign\ B\sqrt{\frac{\sqrt{A^2+B^2}-B}{2}} \tag{3.14}
$$

with $k_{yf} = k_{yf}' + jk_{yf}''$, $A = k_{xn}^2 + k_{zm}^2 - k_{yf}'^2 + k_{yf}''^2$, $B = 2k_{yf}' k_{yf}''$.

The real part of (3.14) determines the phase velocity of the wave, and the imaginary part characterizes its damping. The phase velocity of the wave, incident on the front wall of the resonator, is determined by the following relation:

$$
v_{ph} = \frac{Re\{\omega\}}{k_z} \tag{3.15}
$$

This speed can be either more (at $k_{xn}^2 > k_{x0n}^2$) or less (at $k_{xn}^2 < k_{x0n}^2$) than the speed of light, where

$$k_{x0n}^2 = k_{yf}'^2 - k_{yf}''^2 - k_{zm}^2 \pm 2k_{zm}\sqrt{2k_{yf}'k_{yf}'' + k_{zm}^2} \tag{3.16}$$

Equality $k_{xn}^2 = k_{x0n}^2$ (at which the wave has a phase velocity equal to the speed of light) cannot be fulfilled exactly because $k_{yf}'^2, k_{yf}''^2$ and k_{zm}^2 are discrete and fixed. The condition for the greatest closeness of the phase velocity of a wave to the velocity of light is $min|k_{xn}^2 - k_{x0n}^2|$. The mode (or set of modes), that satisfies this requirement, forms the main resonance arising as a result of the interactions of elementary free oscillations.

3.3 Pure copper cavity. Measurements and interpretation

To check the accuracy of manufacturing, first of all experimentally obtained resonances of pure copper cavity are compared with the theoretical results of the cavity.

The resonant behavior of pure copper cavity has experimentally been investigated at CANDLE SRI by measuring the transmission S-parameter $\boldsymbol{S_{12}}$ (forward voltage gain) [95] of the testing cavity, using Network Analyzer ZVB14 [96]. The measurements are performed for the rectangular cross-section copper cavities.

The measured narrow-band extremes are compared with the standing wave eigenfrequencies of rectangular cavity with perfectly conducting walls [97], having the same dimensions ($a' = 22, 32, 42\ mm, b = 65\ mm, l = 200\ mm$):

$$f_{mnq} = \frac{c}{2}\sqrt{\left(\frac{m-1}{a'}\right)^2 + \left(\frac{n-1}{b}\right)^2 + \left(\frac{q-1}{l}\right)^2} \quad m,n,q = 1,2,3 \ldots \quad \begin{cases} if\ m = 1,\ n,q > 1 \\ if\ n = 1,\ m,q > 1 \\ if\ q = 1,\ m,n > 1 \end{cases} \tag{3.17}$$

Note that in IHLCC cavity, when $d = 0$, both equations (P_1 and P_2) are transformed to the expression for the vertical wave number of the ideal resonator (Eq. 3.12): $Sh(ak_y) = 0$ with solution $k_y = j\,\pi(q-1)/a$. Similarly, in the limiting case of $K = k_y$ ($\varepsilon'\mu' = 1$) we have both from (Eq. 3.10.a) and (Eq. 3.10.b): $Sh(a'k_y) = 0$ with solution $k_y = j\,\pi(q-1)/a'$. In these extreme cases, all three eigenvalues are independent from each other.

$a' = 22\ cm$						$a' = 32\ cm$					
N	m	n	q	Exp.	Calc.	N	m	n	q	Exp.	Calc.
1	2	2	6	8.04	8.116	1	1	1	12	8.25	8.25
2	2	2	6	8.12	8.116	2	1	4	8	8.7	8.69
3	2	2	7	8.48	8.489	3	1	1	13	9.06	9
4	2	2	8	8.86	8.909	4	3	1	2	9.4	9.405
5	1	2	13	9.31	9.291	5	1	3	12	9.46	9.453
6	2	2	9	9.39	9.371	6	3	2	2	9.69	9.684
7	2	1	10	9.56	9.594	7	2	3	11	9.97	9.976
8	1	4	10	9.65	9.670	8	3	2	6	10.36	10.358
9	1	5	6	9.92	9.963	9	3	3	5	10.88	10.872
10	1	2	14	10.04	10.019	10	3	2	8	10.97	10.99
11	2	4	5	10.15	10.169	11	1	6	1	11.58	11.539
12	1	5	7	10.28	10.269	12	1	6	3	11.65	11.636
13	1	1	15	10.51	10.50	13	3	4	3	11.76	11.750
14	1	5	8	10.6	10.619	14	1	6	5	11.91	11.922
15	1	5	9	11.01	11.009	15	1	4	14	11.96	11.960
16	1	3	15	11.46	11.470	16	3	3	9	12.05	12.050
17	1	6	5	11.93	11.922	17	1	3	16	12.16	12.160
18	1	5	12	12.3	12.38	18	3	3	10	12.43	12.440
19	2	1	15	12.53	12.519	19	3	2	12	12.7	12.700
20	2	5	8	12.605	12.62	20	3	1	13	13.0	12.996
21	2	2	15	12.71	12.73	21	2	2	17	13.11	13.088
22	1	5	13	12.9	12.892	22	3	4	10	13.48	13.468
23	2	1	16	13.14	13.155						
24	2	3	15	13.33	13.343						
25	2	6	3	13.47	13.486						
26	2	4	6	13.57	13.59						
27	2	5	11	13.7	13.709						
28	2	1	17	13.8	13.802						
29	2	3	16	13.94	13.941						
30	1	5	15	13.98	13.980						

Table 3.1: Comparison of the measured (Exp., GHz) and calculated (Calc., GHz) eigenfrequency values of a rectangular cavity of $22\ cm$ and $32\ cm$ height.

Tables 3.1 and 3.2 show the correlation of eigenfrequencies of the cavity with the perfectly conducting walls, calculated by Eq. 3.12, with measured peaks.

$a' = 42\ cm$											
N	m	n	q	Exp.	Calc.	N	m	n	q	Exp.	Calc.
1	1	4	7	4.12	4.129	10	1	3	10	8.18	8.177
2	1	4	8	4.33	4.344	11	1	2	12	8.56	8.5666
3	1	5	2	4.65	4.63	12	2	1	12	8.98	8.9899
4	1	2	7	5.04	5.057	13	1	4	9	9.17	9.1601
5	1	3	5	5.52	5.505	14	1	3	12	9.45	9.4533
6	1	3	16	6.08	6.080	15	2	5	2	9.93	9.9260
7	2	3	5	6.66	6.562	16	3	3	9	10.42	10.408
	1	1	10		6.75	17	3	3	10	10.84	10.857
8	1	4	5	7.55	7.545	18	3	4	7	10.90	10.918
9	2	3	8	7.85	7.850						

Table 3.2: Comparison of the measured (Exp., GHz) and calculated (Calc., GHz) values of the eigenfrequencies of a rectangular cavity with $42\ cm$ height.

As can be seen from Table 3.1 and 3.2, there is a good matching (up to the second decimal) between experimentally obtained and calculated eigenvalues. This is achieved due to the high precision machining of internal surfaces of the cavity with keeping dimensional accuracy.

The main result of the above research is the establishment of agreement of experimentally obtained narrowband peaks with resonant frequencies of the rectangular copper cavities. This means that the accuracy of manufacturing of copper resonator component allows to obtain the corresponding frequency distribution for the IHLCC cavity with acceptable distortions.

3.4 IHLCC cavity resonance frequency comparison with experimental results

The transmission $\boldsymbol{S_{12}}$ parameters of IHLCC cavity have been measured to perform a comparison between resonant behaviors of real structure and IHLCC.

The defining parameters of the cavity are the following: the height of the inner chamber a, the thickness of the low conductive layer $d = \frac{a'-a}{2}$, the width b and length l of the chamber, conductivity σ_1 and relative dielectric constant ε_1 of low conductive layer.

The choice of material and the thickness of a low-conductive metallic layer, covering the top and bottom walls of cavity, is conditioned by following two factors:

1. The network analyzer ZVB14 provides spectral distribution in the range of $0-14\ GHz$. The resonance frequency is determined roughly by the geometrical parameters of the cavity cross-section: $f_{rez} \approx \frac{c}{2\pi}\sqrt{2/ad}$, which depends on the thickness of the inner layer d and structure height a. Having a bunch in a structure imposes a lower limit on its height ($a{\sim}1\ cm$). Also with the height increase, the impedance decreases, so the height should be near to its lower limit. For a structure with $2-4\ cm$ height, the thickness of the coating should be about $1-0.5\ mm$ to have a resonance frequency in $0-14\ GHz$ range, given by the measuring device.
2. For the double-layer parallel plates the condition of resonance $\zeta \approx Z_0\sigma_1 d{\sim}1$ is derived in chapter 2. Assuming that for the resonator the condition should be approximately the same, the low conducting material is chosen to have $\sigma_1{\sim}2.65\ {}^{S}/_{m}$ conductivity for a layer with $d = 1\ mm$ thickness.

As a result, germanium (Ge) crystal plates with sizes $l = 30\ cm,\ b = 6\ cm,\ d = 1\ mm$ with conductivity $\sigma_1 = 2\ \Omega^{-1}m^{-1}$ [98] and the relative dielectric constant $\varepsilon_1 = 16$, were selected. Measurements were carried out for three different heights: $a = 2\ cm$, $a = 3\ cm$ and $a = 4\ cm$ ($a' = 2.2$ cm, $a' = 3.2$ cm and $a' = 4.2\ cm$, respectively).

For the above-given vertical apertures and the Ge layer thickness, the skin depth at resonant frequency δ is larger than the Ge layer thickness by factor of 3 ($\delta/d > 3$). The predicted resonant frequencies of the corresponding two parallel plates lie in the X-Band region between $9-15\ GHz$.

3.4.1 Comparison with flat two-layer structure

The measured resonant frequencies of the test cavity with laminated horizontal walls have been compared with the ones of the corresponding two-dimensional two-layer structure (outer layer is assumed as a perfect conductor) with inner $1\ mm$ Ge layers.

The longitudinal impedance of two parallel infinite laminated plates is derived in the second chapter of the dissertation. For an ultrarelativistic particle moving parallel with the plates along geometrical axis of the structure with perfectly conducting outer and low

conducting inner metallic layers, the longitudinal impedance can be presented as (Eq. 2.15, Eq. 2.33, Eq. 2.43 and Eq. 2.44)

$$Z_{\parallel} = \frac{Z_0}{16\pi^2}\int_{-\infty}^{\infty}\frac{ku(p^2-u^2)Sh(2pd)}{S_1 S_2}du \tag{3.18}$$

where

$$\begin{aligned} S_1 &= pCh(pd)Ch(ua) + uSh(pd)Sh(ua) \\ S_2 &= (u^2+k^2-p^2)Ch(pd)Ch(ua) + \frac{Kk^2}{q}Sh(pd)Sh(ua) \end{aligned} \tag{3.19}$$

with $a_1 = a/2$, $k = \omega/c$ longitudinal wavenumber and

$$K = \sqrt{u^2 + k^2(1-\varepsilon_1) - jkZ_0\sigma} \tag{3.20}$$

Figure 3.2 presents the longitudinal impedance curves for such parallel laminated plates with $2\ cm,\ 3\ cm$ and $4\ cm$ vertical apertures. The distances between the plates and material of the inner layers (germanium) are the same as in the tested cavities. The dashed lines indicate the measured main resonant frequencies of the corresponding copper cavities with laminated top and bottom walls.

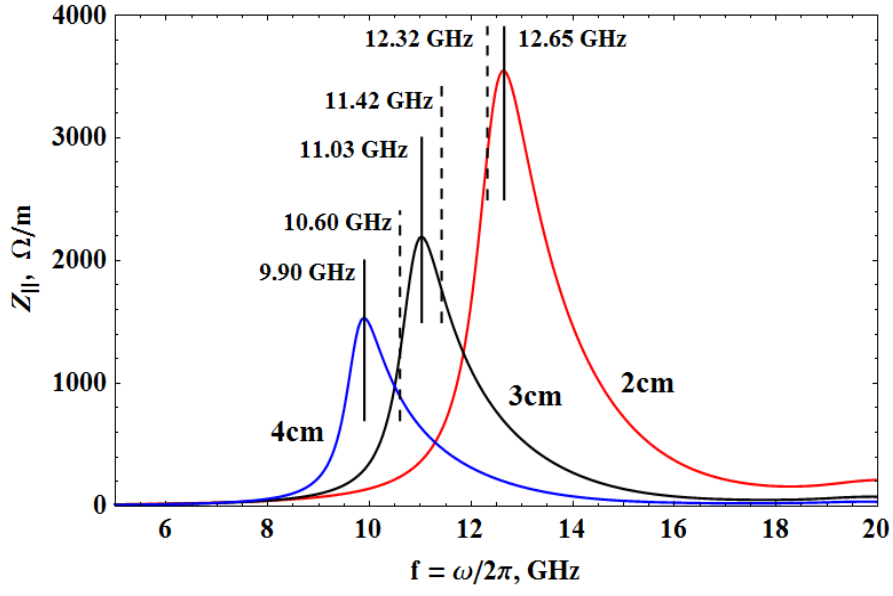

Figure 3.2: The longitudinal impedance of perfect conductor-Ge infinite parallel plates (solid lines) and measured resonant frequencies of copper cavity with Ge inner layers at the top and bottom walls (dashed lines). The Ge layer thickness is $1\ mm$, the vertical apertures are $2\ cm,\ 3\ cm$ and $4\ cm$.

Figure 3.2 shows that there is a good agreement between measured and calculated resonant frequencies. The relative difference in resonant frequency is $2.6\ \%$ for $2\ cm$, $3.5\ \%$ for $3\ cm$ and $7\ \%$ for $4\ cm$ aperture cavities. The difference is caused mainly due to the limited volume of the cavity: the presence of highly conductive sidewalls. The presence of additional bursts is the result of the display of modal structure of the test cavity. Their contribution is weakened by the distance decrease between plates. Thus, by decreasing the height of cavity, its resonant characteristics approach to the characteristics of a flat structure consisting of two identical two-layer parallel plates.

3.4.2 Comparison with the theoretical results of IHLCC resonator

Resonant frequencies of the cavity with outer perfectly conducting walls and inner germanium layers at the top and bottom walls can be obtained from Eq. 3.11. Experimentally fixed resonances (Figure 3.5) can be identified as concrete solutions (modes) of dispersion relations given by Eq. 3.11. Choosing the required mode (k_x, k_z) the main resonance frequencies can be obtained for our IHLCC cavity with ideally conductive walls. Table 3.3 shows the comparison of experimentally observed resonance frequencies of the test cavity ("Experiment" in table) and analytically calculated resonances of cavity with outer perfectly conducting walls ("Calculated" in table).

Aperture	Experiment	Calculated	Rel. dif.
$2\ cm$	$12.32\ GHz$	$12.29\ GHz$	$0.2\ \%$
$3\ cm$	$11.42\ GHz$	$11.36\ GHz$	$0.5\ \%$
$4\ cm$	$10.6\ GHz$	$10.49\ GHz$	$1\ \%$

Table 3.3: The main resonances obtained experimentally and calculated for a cavity with perfectly conducting walls and inner Ge layers at the top and bottom walls.

As can be seen from Table 3.3, there is a good agreement between the measured and calculated results. The relative differences between the calculated and measured frequencies ("Rel. dif." in table) are below $1\ \%$.

As it was noted earlier (see section 3.2), free electromagnetic waves formed in the resonator form standing waves, which can be represented as the superimposition of two oppositely directed traveling waves: incident on the front wall of the resonator and going in

the opposite direction (see Eq.3.13). The phase velocities of these waves are equal in absolute value and opposite in sign (since they propagate in opposite directions): $v_{ph} = c\,Re(k)/k_z$ with $k = \frac{\omega}{c} = \sqrt{k_x^2 + k_z^2 - k_y^2}$; k_x and k_z are real numbers determined by the indices m and n and k_y is determined by the equations (3.10) and is a set of complex numbers. Thus, k is a complex number, the real part of which determines a discrete series of eigenfrequencies of the resonator, and its imaginary part, caused by the finite conductivity of the inner layers covering the inside walls, determines the finite Q of the resonator at its eigen frequencies. Determining k from the equations (3.10), we can obtain the dependence of the phase velocity of the partial traveling waves in the cavity, depending on the frequency. As noted earlier, the exact equality of the phase velocity of the partial wave in the resonator with the speed of light is unlikely. Investigations of the equation solutions (3.10) show that in the frequency range 0 - 14 GHz with the corresponding cavity parameters, only equation $P_4 = 0$ (3.10d) give solutions for slow partial waves. The corresponding graphs are shown in Figure 3.3.

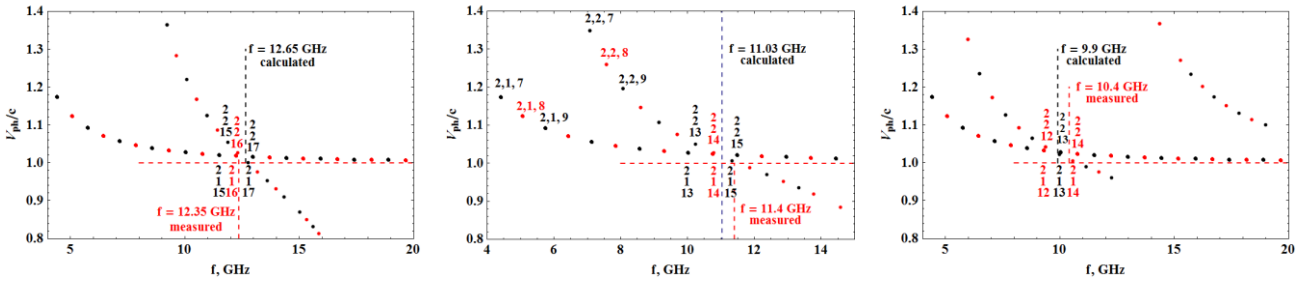

Figure 3.3: The phase velocities of the partial waves in the resonator for modes $P_{4,nfm}$ (solutions of equation $P_4 = 0$) for $n = 2$, $f = 1{,}2$, $m = 1{,}2{,}3{,}4$, ...; $a = 1\ cm$ (left), $1.5\ cm$ (middle), $a = 2\ cm$ (right).

Each of the graphs shows two sequences (discrete curves) of phase velocities of the modes: $P_{4;21m}$ and $P_{4;2,2m}$ with monotonically decreasing phase velocities. On all three graphs, a discrete curve depicting a sequence of modes $P_{4;2,2m}$ intersects the synchronization line $v_{ph}/c = 1$. The second discrete curve containing the phase velocities of the modes $P_{4;21m}$ is located above the line $v_{ph}/c = 1$, gradually approaching it as the frequency increases and intersecting with the first line. In the first and second cases (for $a = 1\ cm$ and $a = 1.5\ cm$) the measured fundamental resonance frequency corresponds to the intersection point of two discrete lines adjacent to the synchronization

line and is calculated (for two – dimensional planar case) close to the intersection point of the first curve and line of synchronization. In the third case, the situation is reversed: the measured fundamental resonance frequency corresponds to the intersection point of the first curve and line of synchronization.

It is obvious, that in all three cases, the main resonance is formed by several modes with close frequencies and close phase velocities: modes $P_{4;2,1,15}$, $P_{4;2,1,16}$, $P_{4;2,2,15}, P_{4;2,2,16}, P_{4;2,2,17}$ for $a = 1\ cm$, $P_{4;2,1,13}, P_{4;2,1,14}$, $P_{4;2,1,15}, P_{4;2,213}, P_{4;2,2,14}, P_{4;2,2,15}$ for $a = 1.5\ cm$ and $P_{4;2,1,13}, P_{4;2,1,14}, P_{4;2,1,15}, P_{4;2,213}, P_{4;2,2,14}, P_{4;2,2,15}$ for $a = 2cm$.

3.5 Summary

This chapter is a logical follow-up of the study of high frequency single-mode accelerating structures with laminated metallic walls (flat and cylindrical) [66, 75, 89, 99].

A theoretical model of a rectangular cavity with horizontal double layer metallic walls is created and electro-dynamic properties of the model are studied. The model with sufficient accuracy displays a test device and enables to clearly interpret the measurement results. Extreme frequencies on the experimental curves have been correlated with the respective modes of resonator model. The experimental results are also compared with the theoretical ones for two infinite parallel plates. A good agreement between them stimulates the experimental study of beam radiation and acceleration in laminated structures. The corresponding experimental program at AREAL test facility is foreseen.

Chapter 4: Electron bunch compression in single-mode structures

4.1 Introduction

The formation and acceleration of ultrashort electron bunches is an important issue for generation of coherent radiation in THz and Infrared regions, driving the free electron lasers (FEL) and direct applications for ultrafast electron diffraction [17-19, 100-102].

Length of bunches generated in RF guns is limited due to technical characteristics of photocathode and lasers. So for having sub-ps bunches one needs to shorten ps bunches generated in RF gun. There are several methods for obtaining sub-ps bunches, e.g. magnetic chicanes are used for high energy beams shortening [41], velocity and ballistic bunching are for low energy beams [42-45]. For all these methods one needs to have an energy modulated beam.

It is well known that the relativistic charge, moving along the structure, interacts with the surrounding environment and excites the electromagnetic field known as wakefield [52-54]. Structures are usually disk, plasma or dielectric loaded channels that drive the corresponding wakefield accelerator (WFA) concepts, the performance of which can be improved by using the asymmetric driving beam to achieve high transformer ratio [61, 103]. For the charge distribution the wakefield acts back to bunch particles producing an energy modulation within the bunch by longitudinal wake potential. The form of longitudinal wake potential depends both on the bunch charge distribution and the surrounding structure [52]. Although for Gaussian bunch the energy modulation is driven by the bunch head-tail energy exchange, for rectangular and parabolic bunch shapes the energy modulation at high frequency can be obtained.

To have an energy modulation, disc and dielectric loaded structures are used. These kind of structures have high order modes excited by a charge when it passes the structure, which leads to energy storage in that parasitic modes and beam instabilities [51-62]. To avoid such effects, one needs a single-mode structure. In this chapter wakefield induced bunch energy modulation during bunch interaction with the single-mode

structures is studied. As a single mode structure, cold plasma and recently proposed internally coated metallic tube (ICMT) are considered [63-66]. In cold plasma purely sine-like wakefields without damping are generated, while in ICMT, wakefields are sine-like with damping factor [66].

The direct application of the holding integral for bunch rectangular or parabolic shape and point wake potential leads to energy modulation within the bunch at the excited mode frequency. To obtain sub-ps bunches, a structure with excited frequency higher than THz is needed. In cold plasma and ICMT, for appropriate parameters, the excited mode is within sub-THz to THz frequency region.

For comparatively low energy bunches wakefield generated energy modulation causes velocity modulation and for proper ballistic distance it leads to density modulation or microbunching. To have that effect in proper distance, energy modulation in a bunch after the structure should be greater than several keV, which can be achieved by $100\ \mu m - 500\ \mu m$ bunches. Electron bunches with $100\ pC$ charge and $10\ MeV$ energy are observed, which correspond to usual values of modern linear accelerators [88].

4.2 Wakefields and Impedances

A relativistic charge Q, passing throw a structure interacts with it. Due to this interaction the particle radiates electromagnetic fields, known as wakefields, which then can act to the test charge q. From the causality principle, wakefields generated by an ultrarelativistic driving charge should vanish in front of it [52, 53]. The longitudinal component of the wakefield produces energy gain (or loss) of the test particle, while the transverse component produces the transverse kick of the test particle.

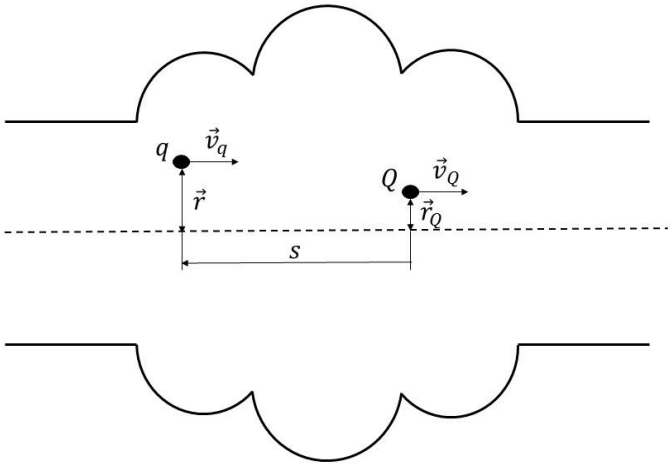

Figure 4.1: Driving Q and test q charge moving in a structure.

The longitudinal wake function (point wake potential) is the integrated longitudinal Lorentz force excited in a structure by a point charge Q experienced by the test particle traveling on an s distance behind it [52]

$$w_z(\boldsymbol{r}, \boldsymbol{r_Q}, s) = -\frac{1}{Q}\int_{-\infty}^{\infty} E_z\left(\boldsymbol{r}, \boldsymbol{r_Q}, z, t = \frac{z+s}{c}\right) dz \tag{4.1}$$

where E_z is the longitudinal component of excited electric field, $\boldsymbol{r}$ is a transverse offset of test particle, $\boldsymbol{r_Q}$ is a transverse offset of source particle and c is the speed of light in vacuum (Figure 4.1). Here $s > 0$ corresponds to the distance behind the driving point charge, $s = 0$ to the position of the charge and $s < 0$ to the distance in front of the charge.

The transverse wake function is defined as an integrated transverse Lorentz force acting on a test particle

$$\boldsymbol{w}_\perp(\boldsymbol{r}, \boldsymbol{r_Q}, s) = -\frac{1}{Q}\int_{-\infty}^{\infty} (\boldsymbol{E} + \boldsymbol{v} \times \boldsymbol{B})_\perp\left(\boldsymbol{r}, \boldsymbol{r_Q}, z, t = \frac{z+s}{c}\right) dz \tag{4.2}$$

For a longitudinal distributed $\lambda(s)$ driving bunch, the wake potentials are defined as an integrated longitudinal and transverse Lorentz forces excited by a bunch at the position of the test particle traveling on an s distance behind it. Here distance s is measured from the center of driving bunch. The longitudinal wake potential could be obtained from the wake functions using the convolution integral

$$W_{\parallel}(s) = \int_{-\infty}^{s} w_z(s-s')\lambda(s)\,ds' \tag{4.3}$$

here integration is from $-\infty$ to s, because there is no field in front of driving bunch.

The total energy loss of the driving charge in a structure due to its radiation is proportional to the square of the charge

$$\Delta U = Q^2 K_{loss} \tag{4.4}$$

The proportionality factor K_{loss} is a longitudinal loss factor and can be presented by wake potentials

$$k_{loss} = \int_{-\infty}^{\infty} W_{\parallel}(\tau)\lambda(\tau)d\tau \tag{4.5}$$

The wake potential is a function of time, while Fourier transformation of the wake potential gives formation in frequency domain and is called the impedance [52, 53]

$$\begin{gathered} Z_{\parallel}(\omega) = \int_{-\infty}^{\infty} W_z(\tau)e^{-i\omega\tau}d\tau = \frac{1}{c}\int_{-\infty}^{\infty} W_z(z)e^{-i\omega z/c}dz \\ W_z(\tau) = \frac{1}{2\pi}\int_{-\infty}^{\infty} Z_{\parallel}(\omega)e^{i\omega\tau}d\omega \end{gathered} \tag{4.6}$$

4.3 Ballistic bunching

Traveling in the structure bunch particles gain (loss) energy due to interaction with wakefields generated by themselves and particles in front of them. Ballistic bunching method of studying microbunching and bunch compression is used. In ballistic method it is assumed that in structure the charge is rigid and only energy modulations occur. The energy modulation leads to the velocity change of particles in the structure and for non-ultrarelativistic bunch charge density redistribution occurs in drift space after the structure (Figure 4.2). For appropriate initial bunch energy and energy spread after the structure, bunches with several μm length can be formed.

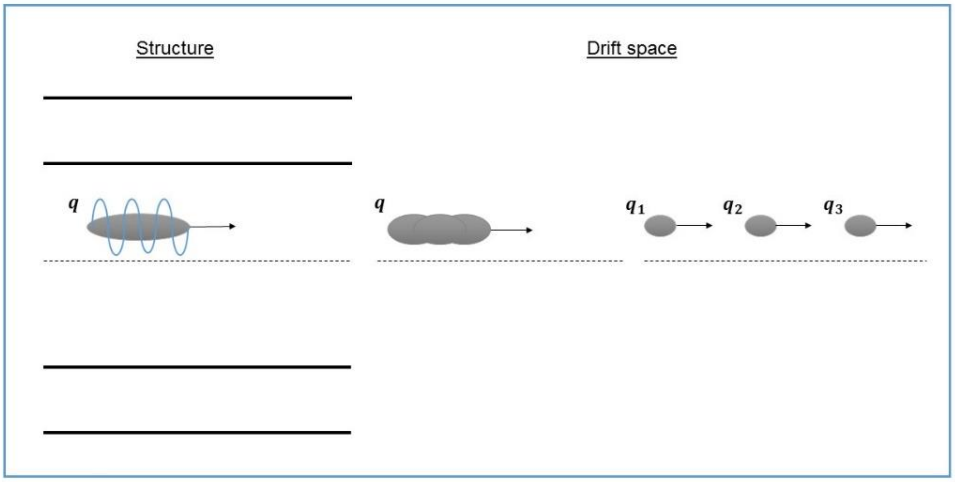

Figure 4.2: Geometry of ballistic bunching (blue line illustrates the wakefield).

After bunch passes the structure, the energy gain (loss) of i-th particle, with initial s_i coordinate, is determined by:

$$\Delta U(s_i) = qQW_z(s_i)L \tag{4.7}$$

where q is the charge of test particle, Q is the total charge of a source bunch, $W_z(s_i)$ is the wake potential in a structure and L is the structure length.

Velocity of i-th particle on the entrance of drift space can be presented as

$$\beta(s_i) = \sqrt{1 - \left(\frac{U_{rest}}{U_f(s_i)}\right)^2} \tag{4.8}$$

where U_{rest} is a particle rest energy and $U_f(s_i) = U_0 + \Delta U(s_i)$ is an energy of i-th particle after the structure. Here cold bunch approximation is assumed, which means that there is no energy spread in the initial bunch. Having a velocity of each particle at the end of the structure, the coordinate $s_{i,f}$ of i-th particle after passing l_{drift} distance in a drift space can be calculated by

$$s_{i,f} = s_i + \Delta s_i = s_i + l_{drift}\left(1 - \frac{\beta(s_i)}{\beta_0}\right) \tag{4.9}$$

where s_i is the initial coordinate of i-th particle, $\beta_0 = \sqrt{1 - \left(\frac{U_{rest}}{U_0}\right)^2}$ is the bunch initial velocity, $\beta(s_i)$ is the velocity of i-th particle after passing the structure. Having the coordinate of each particle in a bunch after a drift space, one can obtain the bunch shape.

Numerical simulations are done for observing wakefield effects on various line charge distributions. The bunch is presented as an ensemble of N particles that experience the energy deviations due to longitudinal wakefield. For simulations $N = 10^6$ particles have been used.

4.4 Energy modulation, bunch compression and microbunching in cold neutral plasma

Bunch charge density modulation in infinite cold neutral plasma is studied via ballistic bunching method. It is assumed that the temperature of electrons is much higher than the one of ions (cold plasma). Under this assumption plasma can be considered as a medium with $\varepsilon = 1 - \omega_p^2/\omega^2$ macroscopic dielectric constant, where the plasma frequency is $\omega_p = 56.4 * 10^3\sqrt{n_e}\, Hz$, with n_e being the plasma electron density (in cm^{-3} units) [63]. The wake function of the relativistic point charge, passing the cold neutral plasma, is given by [63, 64]

$$w_z(s) = -2H(s)K_{loss}\cos\left(k_p s\right) \tag{4.10}$$

where $H(s)$ is the Heaviside step function, $k_p = {}^{\omega_p}/_{c}$ is the wave number, K_{loss} is the longitudinal loss factor of plasma channel.

a

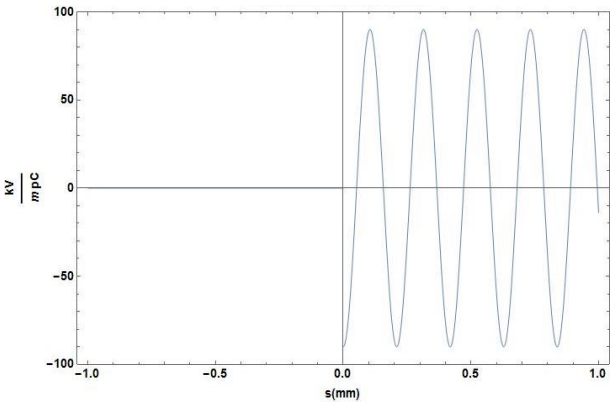

b

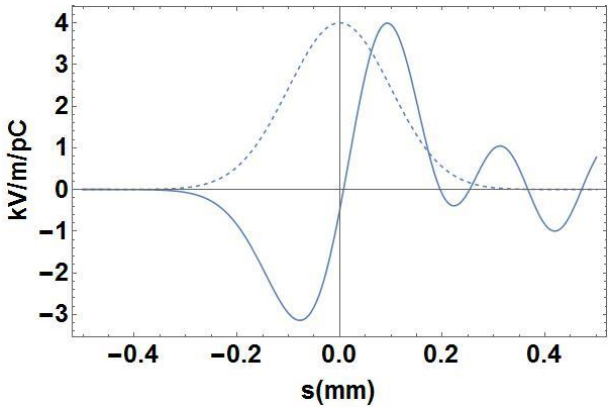

Figure 4.3: Point charge wake function in cold neutral plasma ($\omega_p = 56.4 * 10^3 \sqrt{n_e}\, Hz$ and $K_{loss} = 45\ \frac{kV}{m}/pC$) (left) and Gaussian bunch wake potential (right).

Numerical simulations of bunch compression and microbunching have been performed for the driving bunch with $100\ pC$ charge and $10\ MeV$ initial energy.

Wake potential generated by a Gaussian bunch in plasma channel can be obtained by Eq. 4.2:

$$W_{\parallel}(s) = \frac{1}{\sqrt{2\pi}\sigma} \int_{-\infty}^{s} w_z(s - s') e^{-\frac{s^2}{2\sigma^2}}\, ds' \tag{4.11}$$

Figure 4.3.b presents the wake potential of the Gaussian charge distribution with $0.1\ mm$ rms bunch length in plasma channel with $f_p = {\omega_p}/{2\pi} = 1.43\ THz$ plasma frequency (wavelength $\lambda_p = 0.2\ mm$).

It can be seen that the wake potential is decelerating at the bunch head ($s < 0$) and accelerating at its tail ($s > 0$). This leads to bunch compression till some critical drift space distance, after which particles with coordinates $s > 0$ overtake particles with coordinates $s < 0$. For distances longer than the critical distance, the bunch starts to expand and debunching process begins. From Figure 4.3.b it can be seen that the central part $(\sim 70\%)$ of the bunch is affected by a focusing wake, while the bunch tail is affected by a decelerating wake.

Compressed bunch shape at various drift space distances after $2\ m$ plasma channel is shown in Figure 4.4. The dashed line represents the initial Gaussian bunch distribution.

It can be seen, that till $3.5\ m$ drift space length, the bunch is compressing, after which it starts to expand. On $3.5\ m$ drift space length the rms length of the bunch central part, that contains $70\ \%$ of the particles, is $15\ \mu m$.

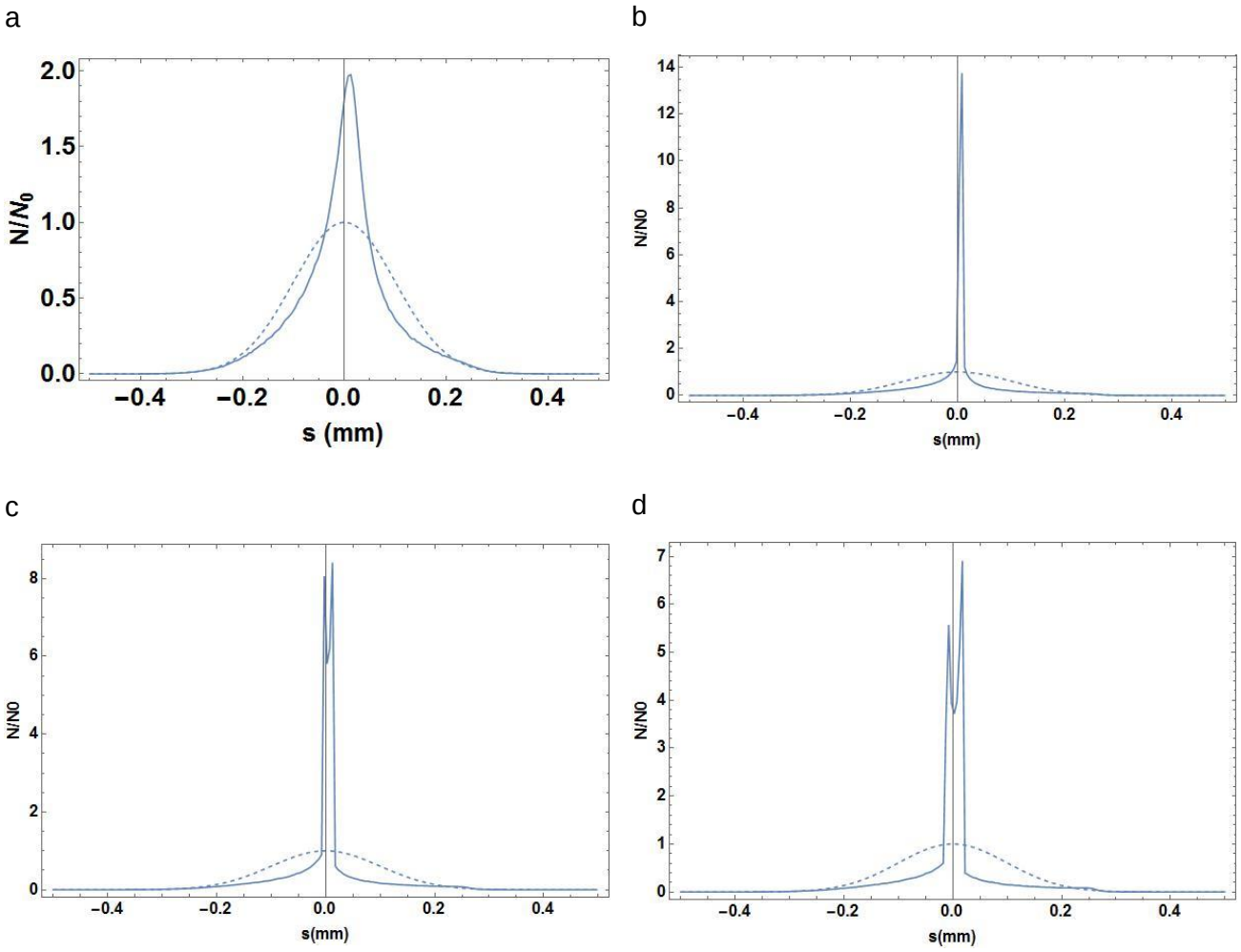

Figure 4.4: Line charge distribution after bunch passes l_{drift} distance in drift space

$a)\ l_{drift} = 1.5\ m$, b) $l_{drift} = 3.5\ m$, c) $l_{drift} = 4\ m$, d) $l_{drift} = 4.5\ m$.

To find the maximum compression, rms length dependence on distance is calculated. The rms length of the Gaussian bunch $70\ \%$ (central part) and $100\ \%$ particles dependence on bunch travel distance in drift space is shown in Figure 4.5. As it was mentioned, the bunch tail is affected by defocusing wakefield. This defocused part artificially increases rms length of a whole bunch and it always stays above $70\ \mu m$. For $70\ \%$ bunch particles, maximum bunch compression is reached at $4\ m$ distance (bunch rms length is $\sim 12\ \mu m$) after which the debunching process starts.

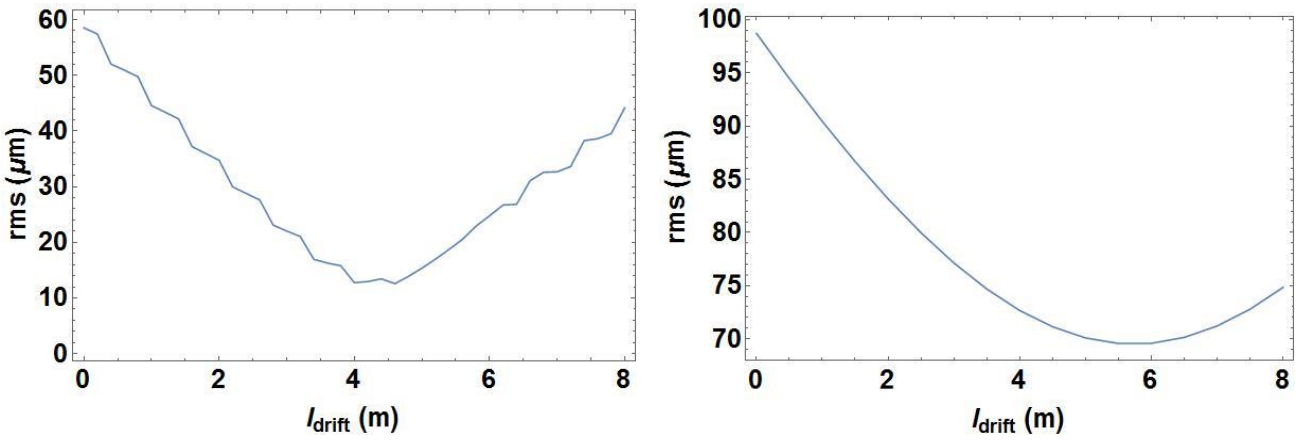

Figure 4.5: The Gaussian bunch longitudinal rms length for 70 % (left) and 100 % (right) versus drift distance.

To have a microbunching, one needs a wakefield with several times smaller wave length than the bunch length. High frequency fields generated by Gaussian distribution are very low because of exponential damping factor in distribution. While for Gaussian bunch it is not possible to have a microbunching in appropriate distances, for some non-Gaussian distributed bunches it is possible.

For the rectangular uniform charge distribution the wake potential in plasma channel produces bunch energy modulation at the excited mode wavelength.

Rectangular uniform line charge distribution is in the form of

$$\lambda(s) = \begin{cases} \frac{1}{2a}, & |s| \le a \\ 0\,, & |s| > a \end{cases} \tag{4.12}$$

and the rms length of the bunch is given by $\sigma = \frac{a}{\sqrt{3}}$.

Wake potential of such a bunch can be derived from Eq. 4.2

$$W_z(s) = \int_{-\infty}^{\infty} w_z\left(k_p(s-s')\right)\lambda(s')ds' = \begin{cases} 0 & ,s < -a \\ \frac{k_{loss}}{2ak}\sin\left(k_p(s+a)\right) & ,|s| \le a \\ \frac{k_{loss}}{ak}\sin\left(k_p a\right)\cos\left(k_p a\right), & s > a \end{cases} \tag{4.13}$$

Figure 4.6 shows the wake potential generated by a rectangular uniform distributed bunch of $0.58\,mm$ rms length ($2\,mm$ total length) in a plasma channel with $0.6\,mm$ ($f_p \approx 0.5\,THz$) excited mode wavelength.

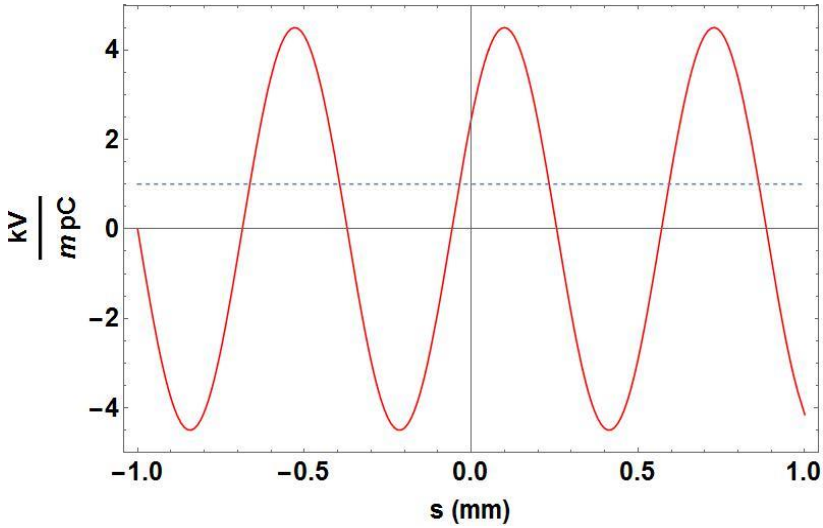

Figure 4.6: Uniform bunch wake potential.

The energy modulation at the wakefield excited mode frequency leads to the charge density modulation as the beam travels in free space.

Charge density modulation at various drift space distances after $0.3\,m$ plasma channel is shown in Figure 4.7. As it can be seen, the density modulation leads to the formation of three microbunches.

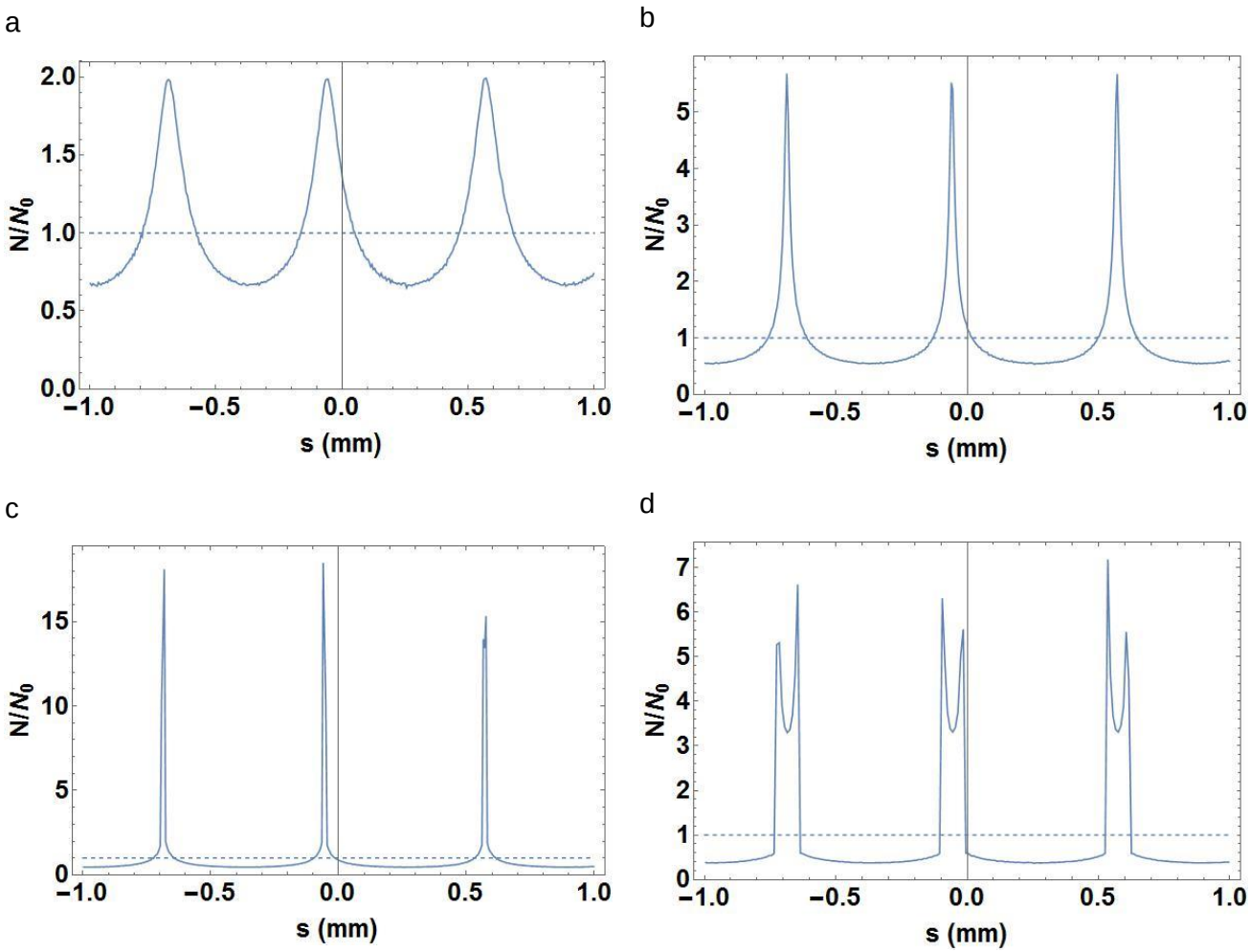

Figure 4.7: Line charge distribution after passing l_{drift} distance in a drift space $a)$ $l_{drift} = 1.5\ m$, b) $l_{drift} = 2.5\ m$, c) $l_{drift} = 3.5\ m$, d) $l_{drift} = 5\ m$.

The best bunching is at the $3.5\ m$ drift space distance, where the initial rectangular bunch is transformed into three microbunches with $14\ pC$ charge and $40\ \mu m$ full-width at half maximum (FWHM). After that distance debunching process starts (Figure 4.7.d).

Parabolic line charge distribution is taken in the form of

$$\lambda(s) = \begin{cases} \frac{1}{2a^3}(a^2 - s^2), & |s| \le a \\ 0 \quad , & |s| > a \end{cases} \tag{4.14}$$

and rms length of the bunch is determined by $\sigma = \frac{a}{\sqrt{5}}$.

The longitudinal wake potential of parabolic charge can be derived from Eq. 1.2

$$W_z(s) = \int_{-\infty}^{\infty} w_z\big(k(s-s')\big)\lambda(s')ds' =$$

$$\begin{cases} 0 & , \ s < -a \\ \frac{k_{loss}}{a^3k^3}\left[\sin\big(k(s+a)\big) - ka\cos\big(k(s+a)\big) - ks\right] & , |s| \le a \\ \frac{k_{loss}}{a^3k^3}\left[\sin\big(k(a+s)\big) + \sin\big(k(a-s)\big) - ka\Big(\cos\big(k(a+s)\big) + \cos\big(k(a-s)\big)\Big)\right], & s > a \end{cases} \quad (4.15)$$

The wake potential for parabolic charge distribution of $0.45\,mm$ rms length ($2\,mm$ full length) is shown in Figure 4.8. The dashed line represents bunch shape. To satisfy the microbunching criterion a plasma channel with $0.6\,mm$ ($f_p \approx 0.5\,THz$) excited mode wavelength is taken.

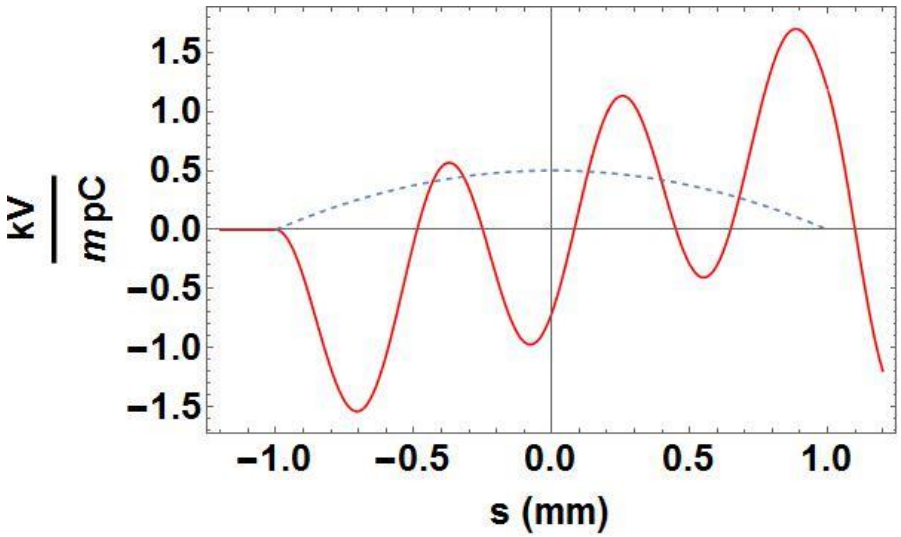

Figure 4.8: Parabolic bunch wake potential.

The energy modulation of particles is observed with linear ramp of the average energy deviation.

Figure 4.9 shows the parabolic charge density modulation at various drift space distances after $1\,m$ plasma channel length. The density modulation leads to microbunching and initial bunch transforms into three microbunches.

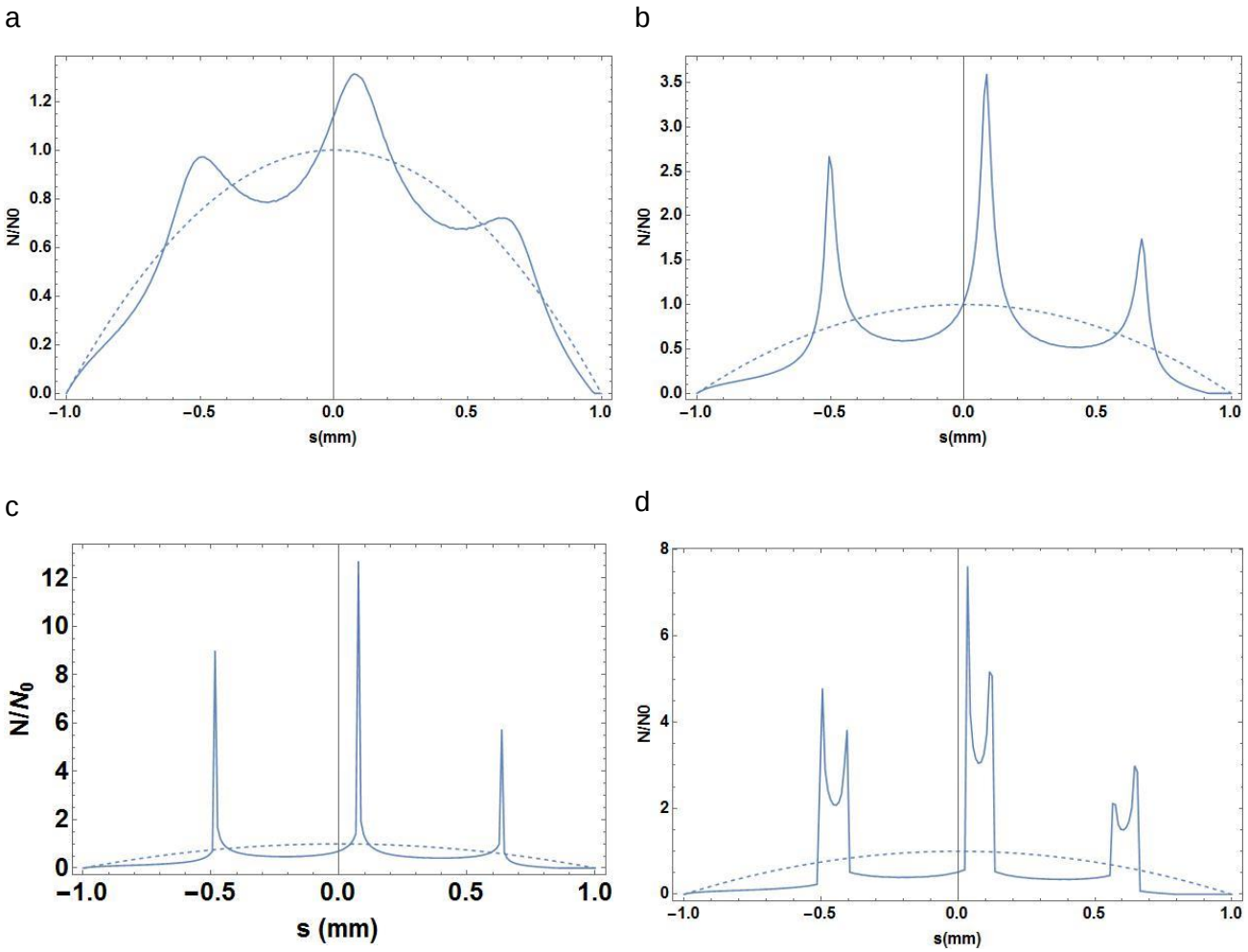

Figure 4.9: Line charge distribution after passing l_{drift} distance in a drift space $a)$ $l_{drift} = 1\ m$, b) $l_{drift} = 3\ m$, c) $l_{drift} = 5\ m$, d) $l_{drift} = 7\ m$.

The best bunching is observed on a $5\ m$ drift space length, where microbunches with $10\ pC$ charge $20\ \mu m$ length (FWHM) are formed. It can be seen that at $7\ m$ drift space length, debunching of all three microbunches occurs.

4.5 Energy modulation, bunch compression and microbunching in internally coated metallic tube

Energy and charge density modulation of Gaussian, rectangular uniform and parabolic charge distributions in ICMT are observed. The geometry of ICMT is shown in Figure 4.10.

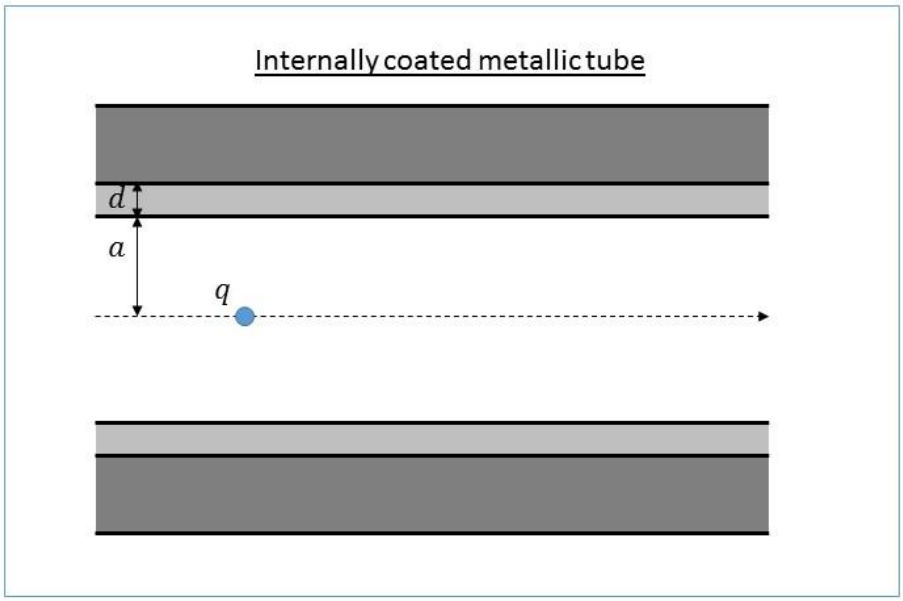

Figure 4.10: Geometry of the ICMT.

In a high frequency range, for a thin, low conductivity inner layer and infinite thick, perfectly conducting outer layer the ICMT is a single-mode structure with $f_0 = \frac{c}{2\pi}\sqrt{2/ad}$ resonant frequency, where a is the inner radii of a layer and d is its thickness.

Wake function generated in ICMT by an ultrarelativistic point charge moving along the structure axis can be presented as [66]:

$$w_{\parallel}(s) = -\frac{Z_0 c}{\pi a^2} e^{-\alpha s}\left[\cos(k_a s) - \frac{\alpha}{k_a}\sin(k_a s)\right] \tag{4.17}$$

where, $k_a = \sqrt{{k_0}^2 - \alpha^2}$, $k_0 = \frac{2\pi}{c} f_0$ and α damping factor is a function of layer thickness and conductivity.

For non-ultrarelativistic particle ($10\ MeV$), the longitudinal wake function calculated in [104] is used. Wake functions of a point charge with various energies are shown in Figure 4.11.

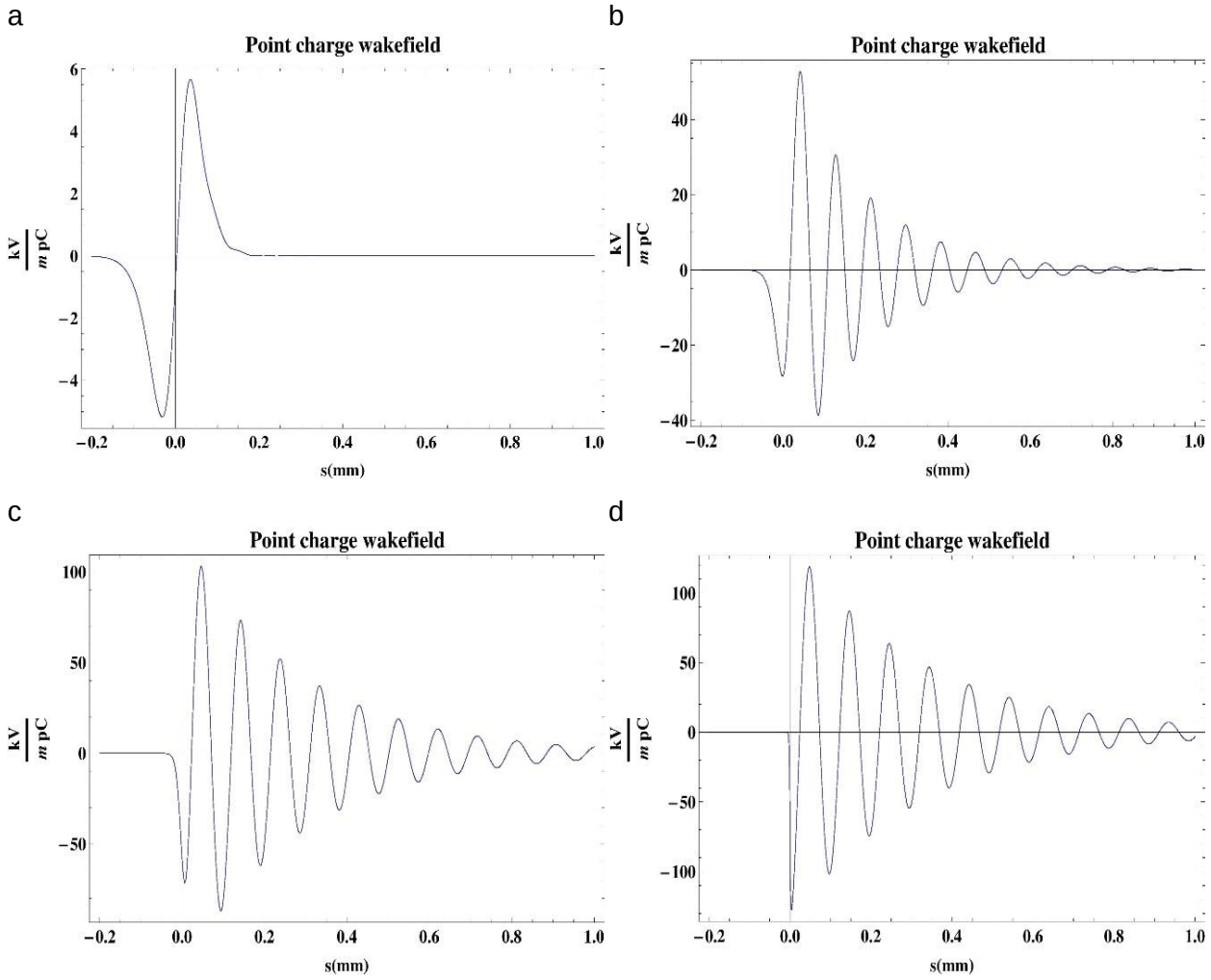

Figure 4.11: Wake functions of a point charge with gamma factor γ

a) $\gamma = 10$, b) $\gamma = 20$, c) $\gamma = 40$, d) $\gamma = 80$.

Matching the inner radii of the internal cover and its thickness, one can obtain a resonant frequency in THz region in the ICMT.

Numerical simulations are performed to determine the bunch shape after drift space for a driving bunch charge of $q = 100\,pC$ with $U_0 = 10\,MeV$ initial energy. The inner diameter of a structure is $0.5\,mm$, electric conductivity of the first layer is $10^4\,\frac{S}{m}$, thickness of the first layer is $1\,\mu m$. Excited mode frequency in ICMT with these parameters is approximately $f_0 = \frac{c}{2\pi}\sqrt{2/ad} = 3\,THz$, which corresponds to $0.1\,mm$ wavelength. Point wake function of such a structure is shown in Figure 4.11.b.

Figure 4.12 presents the wake potential of the Gaussian charge distribution with $0.1\ mm$ rms length (the dashed line shows bunch shape).

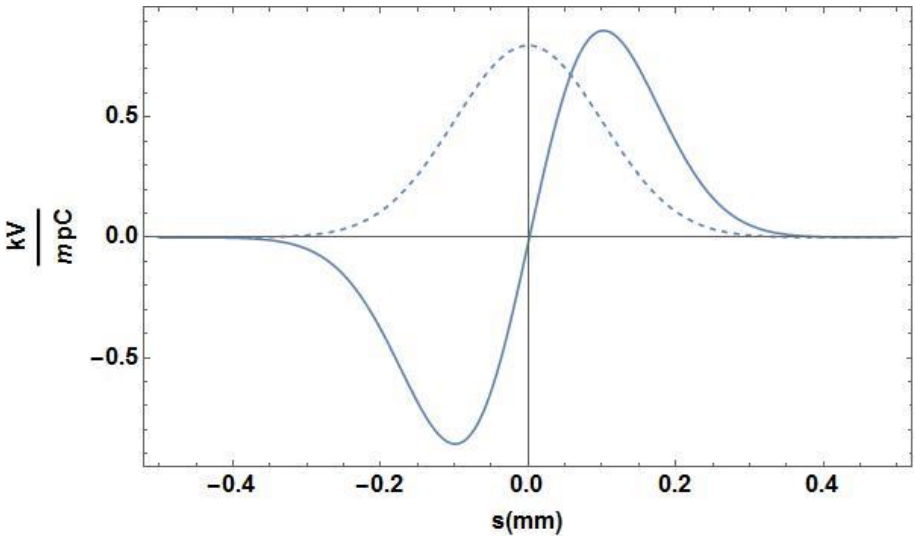

Figure 4.12: $100\ \mu m$ Gaussian bunch wake potential.

The wake potential is decelerating at the bunch head ($s < 0$) and accelerating at its tail ($s > 0$). This energy modulation can lead to bunch compression for appropriate drift space length.

The compressed bunch shape at various drift space distances after $1\ m$ ICMT is shown in Figure 4.13. The dashed line presents the initial Gaussian bunch distribution. The bunch is compressing till about $4\ m$ drift space length after which the bunch tail passes its head and the bunch starts to expand.

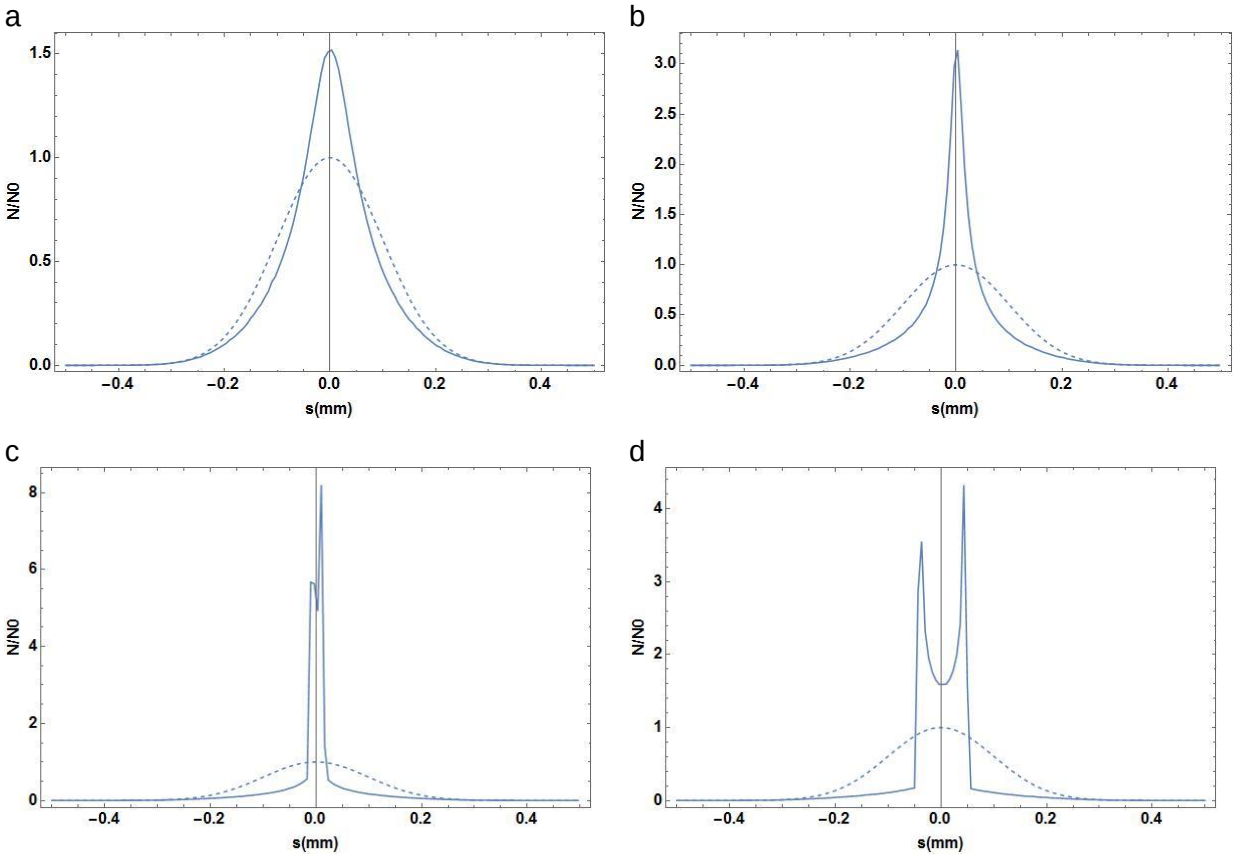

Figure 4.13: Line charge distribution at l_{drift} drift space distances $a)$ $l_{drift} = 1\ m$, b) $l_{drift} = 2\ m$, c) $l_{drift} = 4\ m$, d) $l_{drift} = 6\ m$.

In ICMT, like in plasma, the Gaussian bunch is affected by a strong focusing field on its central part, while in its head and tail there is a weak field. Note that in ICMT there is no debunching field on the bunch tail. The rms lengths of $70\ \%$ (central part) and $100\ \%$ particles versus bunch travel distance in drift space is shown in Figure 4.14. The best compression is reached at $3.8\ m$ drift space distance, where a bunch with $70\ pC$ charge and $8.02\ \mu m$ rms length is formed.

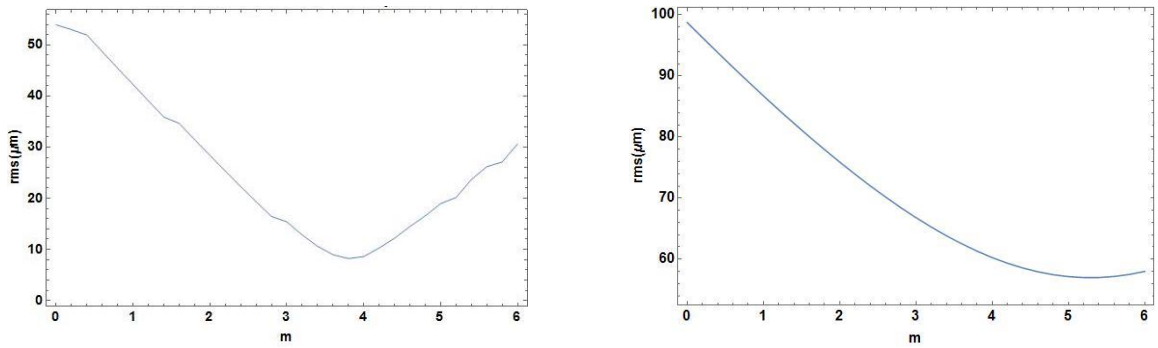

Figure 4.14: rms of 70% (left) and 100% (right) of particles in a bunch versus drift space distance.

To have a microbunching process in a structure one needs a bunch several times longer than the excited wavelength ($0.1\,mm$). This criterion is taken into account for studying microbunching of uniform rectangular and parabolic bunches.

Microbunching of rectangular uniform charge distribution with $0.17\,mm$ rms length ($0.6\,mm$ total length) in ICMT is studied. Wake potential of the bunch is presented in Figure 4.15 (dashed line shows bunch shape). This wake potential generates an energy modulation within the bunch at excited mode wavelength.

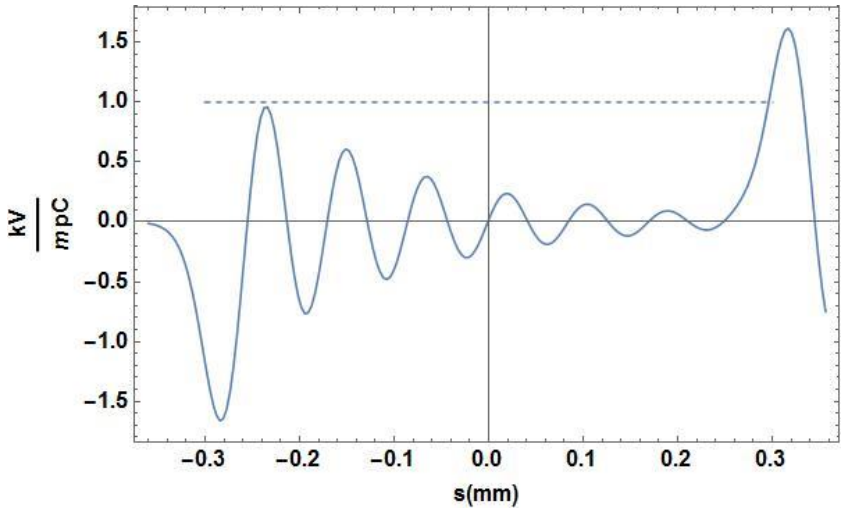

Figure 4.15: Uniform bunch wake potential.

The excited energy modulation leads to charge density modulation while it travels in a free space. Figure 4.16 shows charge density modulations in various drift space distances after $0.2\,m$ ICMT. The initial uniform bunch is transformed into several microbunches.

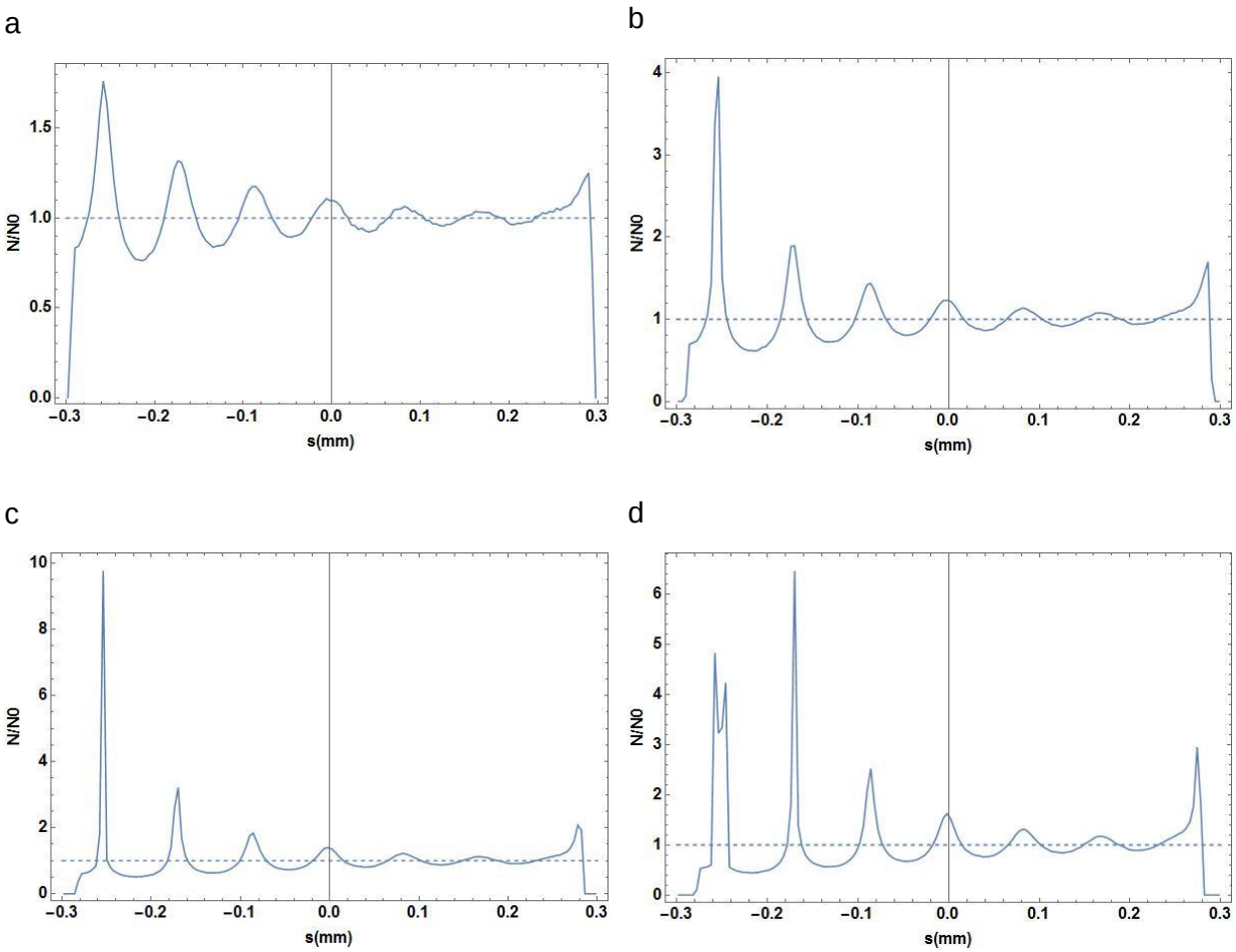

Figure 4.16: Line charge distribution after passing l_{drift} distance in a drift space $a)$ $l_{drift} = 1\ m$, b) $l_{drift} = 2\ m$, c) $l_{drift} = 3\ m$, d) $l_{drift} = 4\ m$.

The best bunching is on $3\ m$ drift space length, after which a debunching process starts. Full-width at half maximum (FWHM) of the first microbunch is $8\ \mu m$, which is a good length for generating THz radiation. $7.8\ \%$ of total charge is concentrated in a full-width region of the first microbunch, and $10\ \%$ in a three-full-width region. The full-width of the second microbunch is $16\ \mu m$. $5.94\ \%$ of total charge is concentrated in a full-width region and $10.5\ \%$ in three-full-width region.

Wake potential of parabolic charge distribution with $0.13\ mm$ rms length ($0.6\ mm$ total length) is presented in Figure 4.17 (the dashed line shows bunch shape). Bunch damping energy modulation with linear ramp of the average energy deviation is observed.

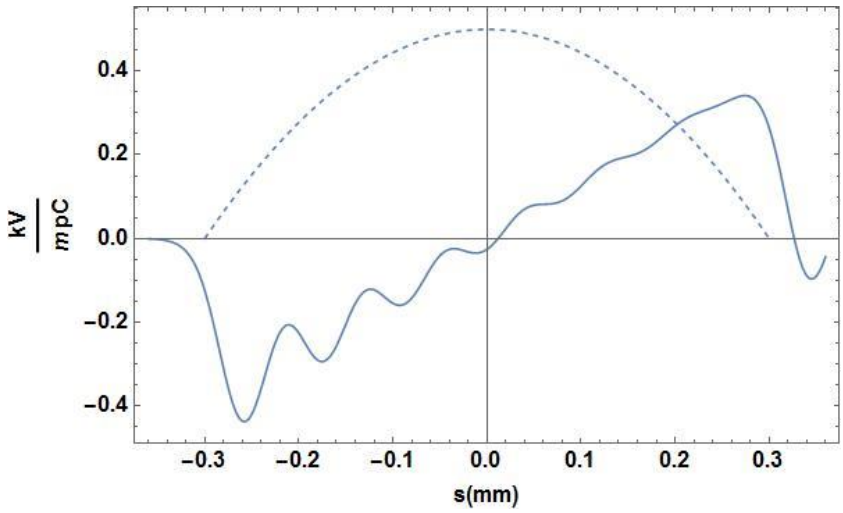

Figure 4.17: Parabolic bunch wake potential.

Bunch shape change in various drift space lengths after $1\ m$ ICMT is shown in Figure 4.18. The initial parabolic bunch transforms into several microbunches.

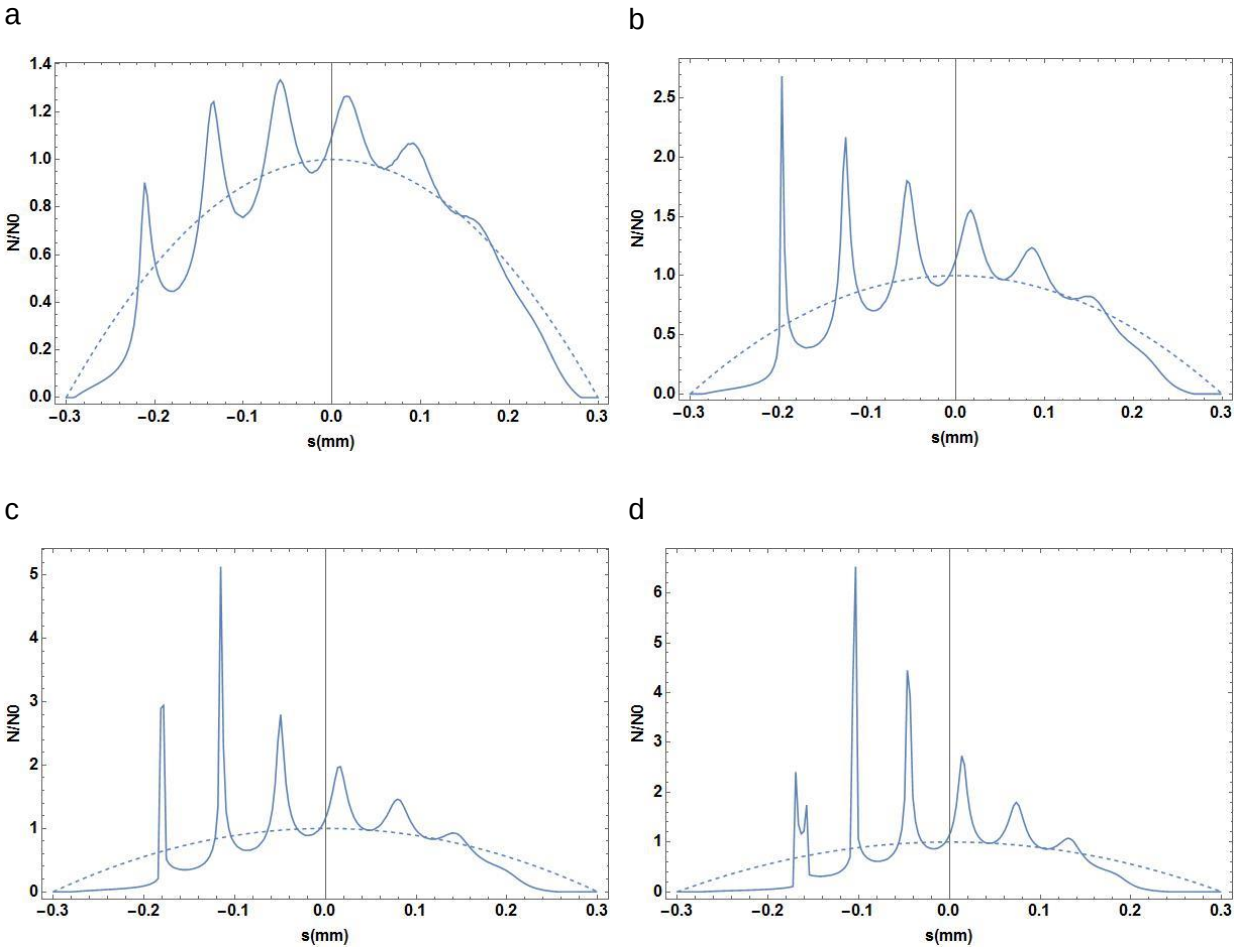

Figure 4.18: Line charge distribution after passing l_{drift} distance in a drift space $a)\ l_{drift} = 3\ m$, b) $l_{drift} = 5\ m$, c) $l_{drift} = 7\ m$, d) $l_{drift} = 9\ m$.

The best bunching is on $7\ m$ drift space length. On that distance FWHM of the first microbunch is $7.5\ \mu m$. $1.8\ \%$ of total charge is concentrated in a full-width region of the first microbunch, and $2.2\ \%$ in a three-full-width region. FWHM of the second microbunch is $3\ \mu m$. $1.54\ \%$ of total charge is concentrated in a full-width region and $2.42\ \%$ in a three-full-width region.

4.6 Summary

Energy and charge density modulations of relativistic electron bunch, after its interaction with cold plasma and ICMT, have been studied. The bunching and microbunching processes of cold, low energy ($10\ MeV$) electron bunches of Gaussian, rectangular and parabolic charge distributions are researched by ballistic method. It is shown, that the Gaussian bunch interaction with these structures leads to its compression.

Bunch shape	q_0	U_0	σ_0	σ_p, q_p	σ_t, q_t
Gaussian	$100\ pC$	$10\ MeV$	$100\ \mu m$	$12\ \mu m$, $70\ pC$	$8.02\ \mu m$, $70\ pC$

Table 4.1: Gaussian bunch parameters before and after interaction with plasma and ICMT.

Table 4.1 shows Gaussian bunch compression after plasma channel and ICMT. In the table q_0 is for bunch initial charge, U_0 is for initial energy, σ_0 is the initial rms length, σ_p and q_p are compressed bunch rms length and charge for plasma channel and finally σ_t and q_t are rms length and charge for ICMT.

In cold plasma, a Gaussian bunch with $0.1\ mm$ rms length and $100\ pC$ charge can be compressed by factor of 8, while in ICMT it can be compressed by factor of 12. For the rectangular and parabolic bunches, several times longer than the structure excited frequency, the microbunching process can be obtained.

	Plasma		ICMT		
Bunch shape	$a_{0,p}$	a_p, q_p	$a_{0,t}$	a_t, q_t	a_t, q_t
Rectangular	$2\ mm$	$40\ \mu m$, $14\ pC$	$0.6\ mm$	$8\ \mu m$, $7.8\ pC$	$16\ \mu m$, $6\ pC$
Parabolic	$2\ mm$	$20\ \mu m$, $10\ pC$	$0.6\ mm$	$7.5\ \mu m$, $1.8\ pC$	$3\ \mu m$, $1.5\ pC$

Table 4.2: Parameters of rectangular and parabolic bunches before and after interaction with plasma and ICMT.

Table 4.2 shows microbunching results for rectangular and parabolic bunches. In the table indexes p and t are for plasma channel and ICMT, respectively. a_0 is for the bunch initial length (FWHM), a and q represent the lengths and charges of microbunches.

It is shown that in cold plasma a uniform bunch with $2\ mm$ total length ($0.58\ mm$ rms) and $100\ pC$ charge can be splitted into three microbunches with $40\ \mu m$ FWHM length and $14\ pC$ charge. Parabolic bunch with $2\ mm$ full length ($0.45\ mm$ rms) and $100\ pC$ charge forms three microbunches of $20\ \mu m$ full-width and $10\ pC$ charges. The study of microbunching process of rectangular bunch in ICMT shows that it is possible to generate microbunches of $8\ \mu m$ FWHM length with $7.8\ pC$ charge and $16\ \mu m$ FWHM length with $5.94\ pC$ charge. Having an initial parabolic charge distribution, it is possible to generate microbunches of $7.5\ \mu m$ FWHM length with $1.8\ pC$ charge and $3\ \mu m$ FWHM length with $1.54\ pC$ charge.

Summary

It is shown that in single-mode structures sub-ps bunches can be formed from longer ones. The sub-ps bunch formation is researched in plasma channels and internally coated metallic tubes. The ballistic bunching method is used in research. Bunch shape is numerically reconstructed.

It is shown that two-layer structures with inner low conductivity materials are high frequency single-mode structures. The theory of flat two-layer structure is developed. It is shown that electrodynamic properties of the flat structure are similar to properties of the cylindrical one. Rectangular cavity with horizontal two-layer metallic walls is studied and correlation between modes (obtained experimentally and theoretically) is performed.

The main results of the dissertation are as follows:

- Matrix formalism has been developed which allows to couple point charge radiated electromagnetic fields in the inner and outer regions of multilayer parallel infinite plates.
- Non-ultrarelativistic point charge excited electromagnetic fields in multilayer parallel infinite plates are analytically obtained.
- Explicit expression of non-ultrarelativistic point charge radiation fields in two-layer parallel infinite plates with unbounded external walls is analytically derived. Also point charge radiation fields in single-layer unbounded structures are derived as a special case of two-layer structure.
- Longitudinal impedance and dispersion relations of symmetrical two-layer parallel infinite plates are derived. It is shown that for low-conductivity thin inner layer and high conductivity thick outer layer, the longitudinal impedance has a narrow-band resonance in high frequency region.

- The resonant frequency dependence of the parameters for two-layer parallel infinite plates is studied and resonance frequency dependence on structure parameters is empirically derived.
- Longitudinal wakefields generated by a point charge traveling through the center of the two-layer parallel infinite plates, with outer perfectly conducting material, are calculated. The longitudinal wake potential is a quasi-periodic function with a period given by the resonant frequency as $\frac{c}{f_{res}}$.
- Resonance frequencies of a rectangular cavity with horizontal laminated walls are analytically obtained.
- It is shown that for rectangular cavity with vertical dimensions much bigger then horizontal ones, the resonance frequencies are in a good agreement with frequencies of two-layer parallel infinite plates.
- The measured resonances of copper cavity with horizontal walls, internally covered by germanium thin layer, are correlated with analytically obtained resonance modes of rectangular cavity. All resonances of the test cavity are in conformity with analytically obtained modes.
- It is shown that for appropriate structure parameters the rectangular cavity with internally covered horizontal walls is a good candidate for bunch acceleration and sub-ps (micro) bunch generation.
- Compression of Gaussian bunches and microbunching of rectangular and parabolic bunches is numerically studied in plasma channels and internally coated metallic structures, based on the ballistic bunching method.
- It is shown that Gaussian distributed bunches with initial $100\ \mu m$ rms length can be compressed to $12\ \mu m$ and $8\ \mu m$ rms length in plasma channel and ICMT, respectively.

- It is shown that bunches with $20\ \mu m$ and $3\ \mu m$ full length can be formed due to microbunching of parabolic bunches in plasma channel and ICMT, respectively.
- It is shown that bunches with $40\ \mu m$ and $8\ \mu m$ full length can be formed due to microbunching of rectangular bunches in plasma channel and ICMT, respectively.

The results of the study can be useful for the development of new accelerating structures for particle acceleration, monochromatic coherent radiation sources, ultrashort bunch generation.

Acknowledgements

I would like to express my gratitude to everyone who has supported me during the course of this thesis.

A special note of thanks to my scientific supervisor Dr. M. Ivanyan for guiding and supporting me over these years.

I want to express my thanks to Prof. V. Tsakanov, without whom this dissertation could not be accomplished.

I would also like to express my gratitude to A. Grigoryan, who has helped me during all the work period.

I am also grateful to the stuff of CANDLE SRI for their constant support and assistance. A special thanks to A. Mikayelyan for checking the English grammar of my thesis. My thanks to my wife V. Zakaryan for her patience during this period.

References

[1] A. H. Zewail, “Femtochemistry: Atomic-Scale Dynamics of the Chemical Bond”, J. Phys. Chem. A 104, 5660–5694 (2000).

[2] R. Kuroda,, H. Ogawa, N. Sei, H. Toyokawa, K. Yagi-Watanabe, M. Yasumoto, M. Koike, K. Yamada, T. Yanagida, T. Nakajyo and F. Sakai, “Development of Cs2Te photocathode rf gun system for compact THz SASE-FEL”, Nucl. Instr. and Meth. A 593, 91-93 (2008).

[3] C. Yim, S. Noh, S. Ko, “Beam Parameter measurements of rf-THz linac at PAL”, Proceedings of the International Particle Accelerator Conference, 1059-1061 (2010).

[4] J.B. Hasting, F. M. Rudakov et al., “Ultrafast time-resolved electron diffraction with megavolt electron beams”, Appl. Phys. Lett. 89, 184109 (2006).

[5] P. Musumeci, J. T. Moody, C. M. Scoby, M. S. Gutierrez, H. A. Bender, N. S. Wilcox, “High quality single shot diffraction patterns using ultrashort megaelectron volt electron beams from a radio frequency photoinjector”, Rev. Sci. Instrum. 81, 013306 (2010).

[6] T. Shintake et al., “A compact free-electron laser for generating coherent radiation in the extreme ultraviolet region”, Nature Photonics 2, 555-559 (2008).

[7] J.-H. Han, “Production of a sub-10 fs electron beam with 10^7 electrons” Phys. Rev. ST Accel. Beams 14, 050101 (2011).

[8] G. P. Williams, “Filling the THz gap-high power sources and applications”, Rep. Prog. Phys. 69, 301-326 (2006).

[9] M. Tonouchi, “Cutting-edge terahertz technology”, Nat. Photonics 1, 97-105 (2007).

[10] P. H. Siegel, “Terahertz technology in biology and medicine”, IEEE Trans. Microwave Theory Tech. 52, 2438–2446 (2004).

[11] H. T. Chen, R. Kersting, G. C. Cho, “Terahertz imaging with nanometer resolution”, Appl. Phys. Lett. 83, 3009–3011 (2003).

[12] S. W. Smye, J. M. Chamberlain, A. J. Fitzgerald, E. Berry, “The interaction between Terahertz radiation and biological tissue”, Phys. Med. Biol. 46, R101-R112 (2001).

[13] M. Hangyo, T. Nagashima and S. Nashima, “Spectroscopy by pulsed terahertz radiation”, Meas. Sci. Technol. 13, 1727-1738 (2002).

[14] A. J. Fitzgerald, E. Berry, N. N. Zinovev, G. C. Walker, M. A. Smith and J. M. Chamberlain, “An introduction to medical imaging with coherent terahertz frequency radiation”, Phys. Med. Biol. 47, R67-R84 (2002).

[15] https://www.psi.ch/swissfel/swissfel-accelerator.

[16] http://www.xfel.eu/en/.

[17] A. Gover, “Superradiant and stimulated-superradiant emission in prebunched electron-beam radiators. I. Formulation”, Phys. Rev. ST Accel. Beams 8, 030701 (2005).

[18] A. S. Muller, “Accelerator-Based Sources of Infrared and Terahertz Radiation”, Rev. Accl. Sci. Tech. 03, 165-183 (2010).

[19] D.F. Gordon, A. Ting, T. Jones, B. Hazi, R.F. Hubbard and P. Sprangle, “Particle-in-cell simulation of optical injector for plasma accelerators”, in Proceedings of the Particle Accelerator Conference (PAC’03), 1846-1848 (2003).

[20] G. L. Carr et al., “High-power terahertz radiation from relativistic electrons”, Nature (London) 420, 153-156 (2002).

[21] M. Abo-Bakr, et al, Brilliant, “Coherent Far-Infrared (THz) Synchrotron Radiation”, Phys. Rev. Lett. 90, 094801 (2003).

[22] F. Lemery and P. Piot, “Ballistic Bunching of Photo-Injected Electron Bunches with Dielectric-Lined Waveguides”, Phys. Rev. ST Accel. Beams 17, 112804 (2014).

[23] V. Ayvazyan et al., “First operation of a free-electron laser generating GW power radiation at 32 nm wavelength”, Eur. Phys. J. D 37, 297-303 (2006).

[24] http://www-ssrl.slac.stanford.edu/lcls/.

[25] Z. Wu, A. S. Fisher et al., “Intense terahertz pulses from SLAC electron beams using coherent transition radiation”, Rev. Sci. Instrum. 84, 022701 (2013).

[26] J. Nodvick and D. Saxon, “Suppression of Coherent Radiation by Electrons in a Synchrotron”, Phys. Rev. 96 (1), 180 (1954).

[27] R. H. Dicke, “Coherence in Spontaneous Radiation Processes”, Phys. Rev. 93 (1), 99-110 (1953).

[28] C. J. Hirschmugl, M. Sagurton and G. P. Williams, “Multiparticle coherence calculations for synchrotron-radiation emission”, Phys. Rev. A 44 (2), 44-48 (1991).

[29] G. V. Stupakov, M. S. Zolotorev, “Ponderomotive Laser Acceleration and Focusing in Vacuum for Generation of Attosecond Electron Bunches”, Phys. Rev. Lett. 86 (23), 5274-5277 (2001).

[30] N. Naumova, I. Sokolov, J. Nees, A. Maksimchuk, V. Yanovsky and G. Mourou, “Attosecond Electron Bunches”, Phys. Rev. Lett. 93 (19), 195003 (2004).

[31] S. Antipov et al., “Subpicosecond Bunch Train Production for a Tunable mJ Level THz Source”, Phys. Rev. Lett. 111, 134802 (2013).

[32] S. V. Milton et al., “Exponential gain and saturation of a self-amplified spontaneous emission free-electron laser”, Science 292, 2037-2041 (2001).

[33] A. M. Kondratenko, E. L. Saldin, “Generation of coherent radiation by a relativistic electron beam in an undulator”, Particle Accelerators 10, 207-216 (1980).

[34] L.-H. Yu, M. Babzien, I. Ben-Zvi et al., “High-Gain Harmonic-Generation Free-Electron Laser”, Science 289 (5481), 932-934 (2000).

[35] http://www.elettra.trieste.it/lightsources/fermi/fermi-machine.

[36] S. Reiche, “Overview of seeding methods for FELs”, Proceedings of IPAC’13, Shanghai, China, WEZB102 (2013).

[37] P. Musumeci et al., “Velocity Bunching Experiment at the Neptune Laboratory”, AIP Conference Proceedings 647, 858-868 (2002).

[38] P. Piot, “Overview of alternative bunching and current-shaping techniques for low-energy electron beams”, Proceedings of FEL2015, Daejeon, Korea, MOD02 (2015).

[39] F. Lemery, P. Piot, “Passive Longitudinal-Phase-Space Tailoring of Non-Ultrarelativistic Beams with Dielectric-Lined Waveguides”, AIP Conference Proceedings 1777, 080008 (2016).

[40] G. Xia and A. Caldwell, “Producing short proton bunch for driving plasma wakefield acceleration”, Proceedings of IPAC’10, Kyoto, Japan, THPD051 (2010).

[41] B. E. Carlsten, S. M. Russel, “Subpicosecond compression of 0.1 - 1 nC electron bunches with a magnetic chicane at 8 MeV”, Phys. Rev. E 53 3, R2072-R2075 (1996).

[42] X. J. Wang, X. Qiu, and I. Ben-Zvi, “Experimental observation of high-brightness microbunching in a photocathode rf electron gun”, Phys. Rev. E 54 (4), R3121 (1996).

[43] X. J. Wang, X. Y. Chang, “Femto-seconds kilo-ampere electron beam generation”, Nucl. Instr. and Meth. A 507, 310-313 (2003).

[44] P. Piot, L. Carr, W. S. Graves and H. Loos, “Subpicosecond compression by velocity bunching in a photoinjector”, Phys. Rev. ST Accel. Beams 6, 033503 (2003).

[45] M. Ferrario et al., “Experimental Demonstration of Emittance Compensation with Velocity Bunching”, Phys. Rev. Lett. 104, 054801 (2010).

[46] A. M. Cook, R. Tikhoplav, S. Y. Tochitsky, G. Travish, O. B. Williams and J. B. Rosenzweig, “Observation of Narrow-Band Terahertz Coherent Cherenkov Radiation from a Cylindrical Dielectric-Lined Waveguide”, Phys. Rev. Lett. 103, 095003 (2009).

[47] О. А. Вальднер, А. В. Шальнов, “Электромагнитные поля в диафрагмированных волноводах линейных электронных ускорителей”, Москва, Госатомиздат, (1963).

[48] Э. Д. Газазян, Э. М. Лазиев, “О черенковском излучении в волноводе”, Изв. НАН Арм. ССР, физ.-мат. науки, 16, N2, 79, (1963).

[49] M. Ivanyan, V. Tsakanov, “Coupling Impedance of Rough Resistive Pipe”, IPAC 2011, MOPS045, Spain, 700-702 (2011).

[50] M. Ivanyan, A. Tsakanian, “Impedances and Wakes in Round Three-layer Ceramic Waveguide”, IPAC2011, MOPS046, Spain, 703-705 (2011).

[51] G. Stupakov, K.L.F. Bane, “Surface impedance formalism for a metallic beam pipe with small corrugations”, Phys. Rev. ST Accel. Beams 15, 124401 (2012).

[52] A. W. Chao, “Physics of Collective Beam Instabilities in High Energy Accelerators”, New York, John Willey & Sons, Inc., (1993).

[53] B. W. Zotter and S. A. Kheifetz, “Impedances and Wakes in High-Energy Particle Accelerators”, Singapore, World Scientific, (1997).

[54] H. Wiedemann, “Particle Accelerator Physics”, Springer, Nederland, Vol. 2, (1999).

[55] T. O. Raubenheimer, “Electron Beam Acceleration and Compression for Short Wavelength FELs”, Nucl. Instr. and Meth. A 358, 40-43 (1995).

[56] A. Hofmann, “Beam Instabilities”, CAS Proceedings, Rhodes, Greece, CERN – 95-06, 307-326 (1995).

[57] G. A. Amatuni, V. M. Tsakanov et al, “Dynamic aperture, impedances and instabilities in CANDLE light source”, ICFA Beam Dyn. Newslett 44, 176-183 (2007).

[58] J. L. Laclare, “Coasting Beam Longitudinal Coherent Instabilities”, CAS Proc., Finland, CERN – 94-01, 345-405 (1994).

[59] K. Y. Ng, “Physics of Intensity Dependent Beam Instabilities”, World Scientific, (2005).

[60] Y. Martirosyan, M. Ivanyan, V. Tsakanov, “Beam Current Limitations Study for CANDLE Light Source”, Proc. of EPAC-2002, France, 715-717 (2002).

[61] K. L. Bane, P. B. Wilson, and T. Weiland, “Wake fields and wake field acceleration”, AIP Conf. Proc. 127, 875-928 (1985).

[62] B. M. Bolotovskii, “THEORY OF CERENKOV RADIATION (III)”, Sov. Phys. Usp. 4, 781-811 (1962).

[63] Я. Б. Файнберг, “Ускорение частиц в плазме”, Атомная энергия, 6 (4), 431-446 (1959).

[64] P. Chen, J. M. Dawson, “The plasma wake field accelerator”, AIP Conf. Proc. 130, 201 (1985).

[65] R. Fitzpatrick. “Classical electromagnetism”, The University of Texas at Austin, (2006).

[66] M. Ivanyan, A. Grigoryan, A. Tsakanian, and V. Tsakanov, “Narrow-band impedance of a round metallic pipe with a low conductive thin layer”, Phys. Rev. ST Accel. Beams 17, 021302 (2014).

[67] M. Ivanyan, V. Tsakanov, A. Grigoryan, A. Tsakanian, “The narrow-band resonance in two-layer metallic round tube”, http://arxiv.org/abs/1301.7729, (2013).

[68] R. J. England et al., “Dielectric laser accelerators”, Rev. Mod. Phys. 86, 1337-1389 (2014).

[69] E. A. Nanni, W. R. Huang, K.-H. Hong, K. Ravi, A. Fallahi, G. Moriena, R. J. Dwayne Miller and F. X. Kartner, “Terahertz-driven linear electron acceleration”, Nat. Commun. 6, 8486 (2015).

[70] R. B. Yoder, J. B. Rosenzweig, “Side-coupled slab-symmetric structure for high-gradient acceleration using terahertz power”, Phys. Rev. ST Accel. Beams 8, 111301 (2005).

[71] H. Hahn, “Matrix solution for the wall impedance of infinitely long multilayer circular beam tubes”, Phys. Rev. ST Accel. Beams 13, 012002 (2010).

[72] M. Ivanyan, E. Laziev, V. Tsakanov and A. Vardanyan, S. Heifets and A. Tsakanian, “Multilayer tube impedance and external radiation”, Phys. Rev. ST Accel. Beams 11, 084001 (2008).

[73] N. Wang and Q. Qin, “Resistive-wall impedance of two-layer tube”, Phys. Rev. ST Accel. Beams 10, 111003 (2007).

[74] M. Ivanyan, V. Tsakanov, “Longitudinal impedance of two-layer tube”, Phys. Rev. ST Accel. Beams 7, 114402 (2004).

[75] M. I. Ivanyan, S. V. Zakaryan et al., “High frequency single mode traveling wave structure for particle acceleration”, Nucl. Instr. and Meth. A 829, 187-189 (2016).

[76] W. Gai et al., “Experimental Demonstration of Wake-Field Effects in Dielectric Structures”, Phys. Rev. Lett. 61 (24), 2756-2759 (1988).

[77] K. l. F. Bane and M. Sands, “The Short-Range Resistive Wall Wakefields”, AIP Conf. Proc. 367, 131-149 (1996).

[78] G. Stupakov, K. l. F. Bane, P. Emma, “Resistive wall wakefields of short bunches at cryogenic temperatures”, Phys. Rev. ST Accel. Beams 18, 034402 (2015).

[79] H. S. Uhm, G. Joyce, “Theory of wake-field effects of a relativistic electron beam propagating in a plasma”, Physics of Fluids B: Plasma Physics 3, 1587-1598 (1991).

[80] C. Jing, A. Kanareykin, J. G. Power et al., “Experimental Demonstration of Wakefield Acceleration in a Tunable Dielectric Loaded Accelerating Structure”, Phys. Rev. Let. 106, 164802 (2011).

[81] K. L. F. Bane et al., “Experimental Demonstration of Wakefield Acceleration in a Tunable Dielectric Loaded Accelerating Structure”, Proceedings of PAC’97, Vancouver, British Columbia, Canada, 751046 (1997).

[82] K. L. F. Bane, “Wakefield effects in a linear collider”, AIP Conf. Proc. 153, 971-1014 (1987).

[83] P. Chen et al., “Acceleration of Electrons by the Interaction of a Bunched Electron Beam with a Plasma”, Phys. Rev. Lett. 54, 693-696 (1985).

[84] W. Gai, M. Conde, J. G. Power, “Considerations for a dielectric-based two-beam-accelerator linear collider”, Proc. of IPAC10, Kyoto, Japan, 3428-3430 (2010).

[85] J. B. Rosenzweig et al., “High Frequency, High Gradient Dielectric Wakefield Acceleration Experiments at SLAC and BNL”, AIP Conf. Proc. 1299, 364-369 (2010).

[86] K. L. F. Bane and G. Stupakov, “Terahertz radiation from a pipe with small corrugations”, Nucl. Instr. and Meth. A 677, 67-73 (2012).

[87] S. Zakaryan, “Electron Bunch Compression and Microbunching in Single-Mode Structure”, Armenian Journal of Physics 9 (3), 220-224 (2016).

[88] V. M. Tsakanov, S. Zakaryan et al., “AREAL test facility for advanced accelerator and radiation source concepts”, Nucl. Instr. and Meth. A 829, 284-290 (2016).

[89] M. I. Ivanyan, A. Grigoryan, S. Zakaryan, A. V. Tsakanian, “Impedance and wake of two-layer metallic flat structure”, Armenian Journal of Physics 10 (1), 36-41 (2017).

[90] M. I. Ivanyan, V. S. Zakaryan et al., “On the resonant behavior of laminated accelerating structures”, Journal of Instrumentation 12, P03019 (2017).

[91] G. Korn and T. Korn, “Mathematical handbook for scientists and engineers”, Dover Publications, Mineola, New York (1968).

[92] H. Henke and O. Napoly, “Wake Fields Between Two Parallel Resistive Plates”, in Proc. of the 2nd European Particle Accel. Conf., France, 1046-1048 (1990).

[93] K. Bane and G. Stupakov, “Using surface impedance for calculating wakefields in flat geometry”, Phys. Rev. ST Accel. Beams 18, 034401 (2015).

[94] M. Abramowitz and I. Stegun, “Handbook of Mathematical Functions with formulas, graphs, and mathematical tables”, National Bureau of Standards, (1964).

[95] David M. Pozar, “Microwave Engineering”, 3rd edition, ISBN 10:471448788, John Wiley & Sons Inc., 170-174 (2005).

[96] R & S ZVB Vector Network Analyzer, http:/www.rohde-schwarz.com.

[97] Л. Вайнштейн, “Электромагнитные волны”, 2-е издание, Москва, Радио и связь, (1988).

[98] S. M. Sze, “Physics of Semiconductor Devices”, John Wiley and Sons, New York (1981).

[99] M. Ivanyan, A. Grigoryan, A. Tsakanian and V. Tsakanov, “Wakefield radiation from the open end of an internally coated metallic tube”, Phys. Rev. ST Accel. Beams 17, 074701 (2014).

[100] A. H. Zewail and J. M. Thomas, “4D Electron Microscopy: Imaging in Space and Time”, Imperial College Press, London (2010).

[101] R. K. Li, P. Musumeci, H. A. Bender, N. S. Wilcox and M. Wu, “Imaging single electrons to enable the generation of ultrashort beams for single-shot femtosecond relativistic electron diffraction”, Journal of Appl. Phys. 110, 074512 (2011).

[102] A. Modena et al., “Electron acceleration from the breaking of relativistic plasma waves”, Nature 377, 606-608 (1995).

[103] J. G. Power, W. Gai, X. Sun, A. Kanareykin, “Transformer Ratio Enhancement Using a Ramped Bunch Train in a Collinear Wakefield Accelerator”, PAC 2001 Proceedings, 114-116 (2002).

[104] А. Григорян, “Резонансные свойства излучения низкоэнергетических электронных пучков в двухслойном волноводе”, Изв. НАН Армении, Физика 48, 383-393 (2013).